Comparison of Measured and Monte Carlo-calculated Peak Scatter Factors for 10×10 cm^2 Field Size in 6 MV and 18 MV Photon Beams

Eunah Chung

Master of Science

Medical Physics Unit

McGill University

Montréal,Québec

October 2008

A thesis submitted to McGill University in partial fulfillment
of the requirements of the degree of Master of Science.

©Eunah Chung, October 2008

ABSTRACT

The purpose of this thesis is to measure the peak scatter factors (PSFs) for a 10×10 cm^2 field size in 6 MV and 18 MV photon beams using a Solid Water^{TM} phantom and build-up caps made of Lucite^{TM}, aluminum, brass, and copper. The PSF for the 10×10 cm^2 field size was first determined by extrapolating the measured normalized peak scatter factor (NPSF) to 0×0 cm^2 field size. The extrapolated NPSF was the reciprocal of the PSF(10, $h\nu$). The measured PSF(10, $h\nu$) was then compared to the PSF determined with Monte Carlo methods.

We used Monte Carlo methods to investigate the dependence of the measured signal on the build-up cap material. This was carried out by calculating the primary and scatter dose contributions to the measured signal in the air cavity of the ionization chamber. Based on Monte Carlo studies, a factor was calculated to obtain the PSF from the measurements.

ABRÉGÉ

L'objectif de cette thèse est d'obtenir le peak scatter factor (PSF) de faisceaux de photons de 6 et 18 MV. Les champs utilisés étaient de 10×10 cm^2 et les mesures furent effectuées à l'aide d'un fantme de Solid Water$^{\text{TM}}$ couplé à des capuchons d'accumulation fait de Lucite$^{\text{TM}}$, d'aluminium, de laiton et de cuivre. Le PSF du champ de 10×10 cm^2 a été déterminé en extrapolant le peak scatter factor normalisé (NPSF) d'un champ de 0×0 cm^2. Le NPSF extrapolé correspond à la réciproque du PSF(10, $h\nu$). Le PSF(10, $h\nu$) fut ensuite comparé à celui déterminé à l'aide de méthodes Monte Carlo.

Les méthodes Monte Carlo furent utilises pour étudier la dépendance entre le signal mesuré et le matériel du capuchon d'accumulation. Ceci fut accompli en décomposant le signal provenant de la cavité de la chambre d'ionisation en dose primaire et diffusée. Un facteur liant le PSF et les mesures fut calculé à l'aide d'études Monte Carlo.

ACKNOWLEDGEMENTS

To write this thesis, there are so many people who have helped me. First of all, I would like to thank my supervisor Dr. Ervin B. Podgorsak for his support and guidance during my master project. During this work, while suggesting guidance of the work, he encouraged me to work independently and actively. My appreciation also goes to my co-supervisor Dr. Wamied T. Abdel-Rahman for his guidance of practical aspect of the master project. He helped me in the measurements and the Monte Carlo calculation works. He allowed me to discuss my work anytime, thereby encouraging me to think more actively.

I would also like to thank the other Medical Physics staff who helped me so much. Especially, I am grateful to Rovin van Gils for making the build-up caps used in this project. I would like to acknowledge Margery Knewstubb for her help in the registration work. I express endless thanks to my fellow students Magdalena Bazalova for her help about Monte Carlo calculation works and Luc Serré for his help during my measurements.

Finally, I would like to thank my parents, Iljin Chung and Woesoo Bae, and my brother, Heebum Chung, for their support and encouragement during my study. Without them, I could not continue my study in Montreal. This thesis is dedicated to them.

TABLE OF CONTENTS

ABSTRACT ii

ABRÉGÉ iii

ACKNOWLEDGEMENTS iv

LIST OF TABLES viii

LIST OF FIGURES xi

1 Introduction 1

1.1 Radiotherapy 1
1.2 Radiation Sources in Radiotherapy 1
1.3 Classification of Radiation 2
1.4 Interactions of photons with a medium 3
1.4.1 Photoelectric effect 3
1.4.2 Compton scattering 4
1.4.3 Pair production 4
1.4.4 Rayleigh scattering 5
1.5 Mass attenuation coefficient 6
1.6 Definition of dose 8
1.6.1 The primary dose component 9
1.6.2 The scatter dose component 13
1.7 Dosimetry in radiotherapy 13
1.7.1 Absolute beam dosimetry 13
1.7.2 Relative dosimetry functions 14
1.8 Thesis objectives and outline 23

2 Background 26

2.1 Early definitions of the tissue-air ratio and the peak scatter factor 26
2.2 International Commission on Radiation Units and Measurements, Report 10d 27

2.3 British Journal of Radiology Supplement 11 29
2.4 International Commission on Radiation Units and Measurements, Report 23 30
2.5 British Journal of Radiology Supplement 17 32
2.6 British Journal of Radiology Supplement 25 36
2.7 Summary 38

3 Materials and Methods 42

3.1 Experimental apparatus 42
3.1.1 Ionization chambers and electrometers 42
3.1.2 Radiation beams 46
3.1.3 Solid Water^{TM} phantom 48
3.1.4 Build-up caps 49
3.2 Experimental techniques 51
3.2.1 In-phantom measurements 51
3.2.2 In-air measurements 53
3.3 Monte Carlo simulations 54
3.3.1 EGSnrc code system 54
3.3.2 BEAMnrc 55
3.3.3 NRC user codes 58

4 Results and Discussions 63

4.1 The apparent PSF for 6 MV and 18 MV photon beams 63
4.2 The NPSF for 6 MV and 18 MV photon beams 66
4.2.1 Extrapolated PSF(10, $h\nu$) for 6 MV and 18 MV photon beams 69
4.3 Monte Carlo-calculated SF for ^{60}Co, 6 MV, and 18 MV photon beams 71
4.4 Monte Carlo-calculated PSF for ^{60}Co, 6 MV, and 18 MV photon beams 75
4.5 Air cavity dose versus build-up thickness 76
4.6 Separation of primary and scatter doses in the air cavity of the ionization chamber in the in-air measurements and in the in-phantom measurements 85
4.6.1 Primary and scatter doses in the air cavity in the in-air measurements 85

4.6.2 Primary dose in the air cavity in the in-phantom measurements . . . 92
4.7 PSF(10, $h\nu$) corrected from the apparent PSF(10, $h\nu$) for 6 MV and 18 MV photon beams . . . 95
4.7.1 Correction for scatter dose contribution . . . 95
4.7.2 Correction for primary dose contribution . . . 97

5 Conclusions . . . 105

5.1 Thesis summary . . . 105
5.2 Future work . . . 108

LIST OF TABLES

Table page

1–1 Dependence of the mass attenuation coefficients for photoelectric effect, Compton scattering, Rayleigh scattering, and pair production on incident photon energy and atomic number of medium. 6

1–2 Nominal $z_{\max}$ listed in the BJR Supplement 25[10] for various photon beams. 17

2–1 Chronological summary of the definitions of the TAR and the SF from the ICRU Report 10d[2], the BJR Supplement 11[4], the ICRU Report 23[5], the BJR Supplement 17[6], and the BJR Supplement 25[10]. 39

3–1 The linear attenuation coefficients μ, beam hardening coefficients η, mass attenuation coefficients μ/ρ, and HVLs in copper and lead for the 6 MV and 18 MV photon beams produced in our Varian Clinac 21 EX linac. 48

4–1 NPSF obtained from measurements with Lucite$^{\text{TM}}$, aluminum, brass, and copper build-up caps and that referenced by the BJR Supplement 25[1] for the 6 MV photon beam. 68

4–2 NPSF obtained from measurements with Lucite$^{\text{TM}}$, aluminum, brass, and copper build-up caps and that referenced by the BJR Supplement 25[1] for the 18 MV photon beam. 68

4–3 PSFs(10, $h\nu$) for the 6 MV and 18 MV photon beams obtained with Lucite$^{\text{TM}}$, aluminum, brass, and copper build-up caps. The data are calculated by extrapolating NPSF to 0×0 cm^2 field size. 71

4–4 Primary dose in the air cavity at 1.5 cm depth in the Solid Water™ phantom and primary doses in the air cavity with 1.5 g/cm^2 Lucite™, aluminum, brass, and copper build-up caps for the 10×10 cm^2 field size in the 6 MV photon beam. Column 3 lists the ratio of the primary dose in the air cavity with the build-up cap to that in the Solid Water™ phantom. 93

4–5 Primary dose in the air cavity at 3.0 cm depth in the Solid Water™ phantom and primary dose in the air cavity with 3.0 g/cm^2 Lucite™, aluminum, brass, and copper build-up caps for the 10×10 cm^2 field size in the 18 MV photon beam. Column 3 lists the ratio of the primary dose in the air cavity with the build-up cap to that in the Solid Water™ phantom. 94

4–6 Ratios of the primary dose to the total dose in the air cavity with Lucite™, aluminum, brass, and copper build-up caps for the 6 MV and 18 MV photon beams. Build-up thicknesses are 1.5 g/cm^2 for the 6 MV photon beam and 3.0 g/cm^2 for the 18 MV photon beam. 95

4–7 Apparent PSFs(10, 6 MV) (column 2) and PSFs(10, 6 MV) (column 3) obtained with Lucite™, aluminum, brass, and copper build-up caps. 96

4–8 Apparent PSFs(10, 18 MV) (column 2) and PSFs(10, 18 MV) (column 3) obtained with Lucite™, aluminum, brass, and copper build-up caps. 97

4–9 PSF(10, 6 MV) in Solid Water™ (column 6) obtained using Lucite™, aluminum, brass, and copper build-up caps for in-air measurements and corrected with Eq. 4.15. Column 2 lists the measured apparent PSFs(10, 6 MV) with the Lucite™, aluminum, brass, and copper build-up caps. Columns 3, 4, and 5 list ratios of the primary dose to the total dose deposited in the air cavity with the build-up caps, ratios of the mean restricted collision stopping powers of Solid Water™ to build-up cap materials, and ratios of the mean mass energy absorption coefficients of build-up cap materials to Solid Water™ for the 6 MV photon beam, respectively. 100

4–10 PSF(10, 18 MV) in Solid Water^{TM} (column 6) obtained using Lucite^{TM}, aluminum, brass, and copper build-up caps for in-air measurements and corrected using Eq. 4.15. Column 2 lists the measured apparent PSFs(10, 18 MV) with the Lucite^{TM}, aluminum, brass, and copper build-up caps. Columns 3, 4, 5 list ratios of the primary dose to the total dose deposited in the air cavity with the build-up cap, ratios of the mean restricted collision stopping powers of Solid Water^{TM} to build-up cap materials, and ratios of the mean mass energy absorption coefficients of build-up cap materials to Solid Water^{TM} for the 18 MV photon beam, respectively. 101

LIST OF FIGURES

Figure page

1–1 The mass attenuation coefficients in (a) water and (b) lead for photoelectric effect τ/ρ, Compton scattering σ_{C}/ρ, Rayleigh scattering σ_{R}/ρ, nuclear pair production $\kappa_{\mathrm{pp}}/\rho$, and triplet production $\kappa_{\mathrm{tp}}/\rho$, as well as the total mass attenuation coefficient μ/ρ.[3] 7

1–2 The absorbed dose at point Q in a phantom is divided into primary dose component and scatter dose component. The primary dose component is deposited by photon (1) emitted by the radiation source or photon (3) produced after primary photon (2) has undergone a scattering event outside of the phantom. Photon (5) is produced after primary photon (4) is scattered within the phantom. The dose deposited at point Q from photon (5) contributes to the scatter dose component. 9

1–3 Schematics of (a) narrow beam geometry and (b) broad beam geometry. 11

1–4 Divergence of a point source photon beam.[4] 12

1–5 Schematic definition of the PDD. The PDD at point Q is defined as the quotient of the total absorbed dose at point Q to the total absorbed dose at point P. 14

1–6 PDD curves for various photon beams.[6] 15

1–7 Depth of maximum dose, $z_{\max}$, as a function of field size for 6 MV, 10 MV, and 18 MV photon beams[9]. 16

1–8 Schematic definition of the TAR from the BJR Supplement 17[11]. The TAR is defined as the ratio of the total absorbed dose at point Q to the primary dose at point $\mathrm{Q}_{\max}$. 18

1–9 Schematic definition of the PSF. The PSF is defined as the ratio of the total dose to the primary dose at point $\mathrm{Q}_{\max}$. 19

1–10 Variation of PSF (BSF for low energy photon beams) against energy of photon beams represented by Half-value layer in the range of 0.1 to 4.0 mm Cu for various square field sizes.[10] 20

1–11 PSF for ^{60}Co from BJR Supplement 25[10]. 21

1–12 Schematic definition of the normalized peak scatter factor NPSF, the relative dose factor RDF, and the collimator factor CF. The NPSF is the ratio of the PSF for field size A_{Q} to that for a reference field size $A_{\mathrm{Q}_{\mathrm{ref}}}$; the RDF is the ratio of the total absorbed dose at $z_{\max}$ for field size A_{Q} to that for the reference field size $A_{\mathrm{Q}_{\mathrm{ref}}}$; and the CF is the ratio of the primary dose at $z_{\max}$ for field size A_{Q} to that for the reference field size $A_{\mathrm{Q}_{\mathrm{ref}}}$. 22

2–1 Schematic definition of the TAR from Johns *et al.*[1] The TAR at point Q was defined as the ratio of the exposure at point Q to the exposure at point Q′. 26

2–2 Schematic definition of the TAR from ICRU Report 10d[2]. The TAR at point Q was defined as the ratio of the absorbed dose at point Q in the phantom to the absorbed dose at point Q′ in the small mass of tissue in air. 28

2–3 Schematic definition of the SF according to the ICRU Report 23[5]. The SF at point Q was defined as the ratio of the total exposure to the primary exposure at point Q or the ratio of the total absorbed dose to the primary dose at point Q. 31

2–4 Schematic definition of the TAR according to the BJR Supplement 17[6]. The TAR at point Q was defined as the ratio of the total absorbed dose at point Q to the primary dose at point $\mathrm{Q}_{\max}$. 33

2–5 Schematic definition of the empirical PSF from the BJR Supplement 17[6]. The empirical PSF for field size A_{Q} was defined as the ratio of the the total absorbed dose at point $\mathrm{Q}_{\max}$ in the phantom to the absorbed dose at point $\mathrm{Q}'_{\max}$ in the small mass of build-up material. 35

3–1 The Exradin Miniature Shonka Thimble Chamber model A1SL. . . . 43

3–2 X-ray image of the Exradin A1SL ionization chamber. 44

3–3 3-dimensional rendered image of the Exradin A1SL ionization chamber. 44

3–4 The PTW 30004 Farmer ionization chamber. 45

3–5 Attenuation curves for (a) 6 MV photon beam and (b) 18 MV photon beam in copper and lead. 47

3–6 $30 \times 30 \times 10$ cm^3 Solid Water^{TM} phantom. 49

3–7 Build-up caps made by Lucite^{TM}, aluminum, brass, and copper. . . . 50

3–8 In-phantom measurement setup. The distance from the radiation source to the ionization chamber plane is 100 cm. 52

3–9 Ionization signal versus lateral couch position for a 1×1 cm^2 field size. 52

3–10 In-air measurement setup. The distance from the radiation source to the ionization chamber plane is 100 cm. 54

3–11 Geometries of the Varian Clinac 21 EX linac head for (a) 6 MV and (b) 18 MV photon beams. The phase-space files were scored at $z = 90$ cm. 57

3–12 Photon spectra of Varian Clinac 21 EX (a) 6 MV photon beam and (b) 18 MV photon beam. 59

4–1 Apparent PSF for the 6 MV photon beam, in part (a), and for the 18 MV photon beam, in part (b), against field size measured using a Solid Water^{TM} phantom and build-up caps made of Lucite^{TM}, aluminum, brass, and copper. 65

4–2 NPSF for the 6 MV photon beam, in part (a), and for the 18 MV photon beam, in part (b), versus field size obtained with Lucite^{TM}, aluminum, brass, and copper build-up caps. 67

4–3 Extrapolation of the NPSF, measured with Lucite^{TM}, aluminum, brass, and copper build-up caps, to 0×0 cm^2 field size for the 6 MV photon beam, in part (a), and for the 18 MV photon beam, in part (b). 70

4–4 Total dose, scatter dose, and primary dose per incident fluence for the 10×10 cm^2 field size versus depth along the beam central axis in a Solid Water^{TM} phantom for the ^{60}Co beam. 73

4–5 Total dose, scatter dose, and primary dose per incident electron on target for the 10×10 cm^2 field size versus depth along the beam central axis in a Solid Water^{TM} phantom for the 6 MV photon beam. 73

4–6 Total dose, scatter dose, and primary dose per incident electron on target for the 10×10 cm^2 field size versus depth along the beam central axis in a Solid Water^{TM} phantom for the 18 MV photon beam. 74

4–7 The SF versus depth along the beam central axis for the 10×10 cm^2 field size in a Solid Water^{TM} phantom for ^{60}Co, 6 MV, and 18 MV photon beams. 74

4–8 RZ geometry to represent the Exradin A1SL ionization chamber. . . . 77

4–9 RZ geometry to calculate the air cavity dose in the Exradin A1SL ionization chamber with a build-up cap. 79

4–10 Normalized air cavity dose for the 6 MV photon beam, obtained from the measurements and the Monte Carlo simulations, against build-up thickness for Lucite^{TM} build-up caps, in part (a), and aluminum build-up caps, in part (b). 80

4–11 Normalized air cavity dose for the 6 MV photon beam, obtained from the measurements and the Monte Carlo simulations, against build-up thickness for brass build-up caps, in part (a), and copper build-up cap, in part (b). 81

4–12 Normalized air cavity dose for the 18 MV photon beam, obtained from the measurements and the Monte Carlo simulations, against build-up thickness for Lucite^{TM} build-up caps, in part (a), and aluminum build-up caps, in part (b). 83

4–13 Normalized air cavity dose for the 18 MV photon beam, obtained from the measurements and the Monte Carlo simulations, against build-up thickness for brass build-up caps, in part (a), and copper build-up caps, in part (b). 84

4–14 Normalized primary dose, in part (a), and scatter dose, in part (b), deposited in the air cavity for the 6 MV photon beam versus build-up thickness calculated for Lucite^{TM}, aluminum, brass, and copper build-up caps. 88

4–15 Normalized primary dose, in part (a), and scatter dose, in part (b), deposited in the air cavity for the 18 MV photon beam versus build-up thickness calculated for Lucite^{TM}, aluminum, brass, and copper build-up caps. 90

4–16 RZ Geometry to calculate the primary dose in the air cavity at the nominal z_{max} in the Solid Water^{TM} phantom. 92

CHAPTER 1
Introduction

1.1 Radiotherapy

Radiotherapy is one of the main three cancer treatment modalities; the other two being chemotherapy and surgery. The objective of radiotherapy is to deliver a prescribed dose to a defined target volume, while sparing the normal tissue and critical organs near the target volume. Radiotherapy is a complex process and involves several steps beginning with the diagnosis and localization of the target volume, including treatment planning and accurate dose distribution determination, and ending with accurate dose delivery. The International Commission on Radiation Units and Measurements (ICRU) Report 24[1] has recommended that the accuracy of dose delivered to the target volume compared to the prescribed dose should be within ± 5 % to eradicate the primary tumor and to keep the dose received by healthy organs below their tolerance values.

1.2 Radiation Sources in Radiotherapy

Based on the position of the radiation source with respect to the patient, radiotherapy is divided into two main categories: brachytherapy and external beam radiotherapy, also called teletherapy. In brachytherapy, radiotherapy is carried out with sealed radionuclide sources placed inside the patient within or near the target volume. Radionuclide sources used in brachytherapy are gamma(γ) emitters such as

^{60}Co, ^{137}Cs, ^{192}Ir, ^{125}I, and ^{103}Pd; in rare instances, beta(β) emitters such as ^{90}Sr; and neutron emitters such as ^{252}Cf are also used.

When radiotherapy is carried out with radiation sources set externally to the patient, the procedure is called external beam radiotherapy. External beam radiotherapy with photon and electron beams are commonly used in radiotherapy clinics. However, a small number of radiotherapy clinics carry out external beam radiotherapy with proton, neutron, or heavy charged particle beams. Sources for external radiotherapy photon beams are either sealed radionuclides such as ^{60}Co and ^{137}Cs, or bremsstrahlung x rays. Bremsstrahlung x rays are produced by bombarding a target with energetic electrons. In radiotherapy units, electrons are accelerated using either electrostatic accelerators or cyclic accelerators depending on the accelerating electric field. In electrostatic accelerators, the electric field is conservative and there is an upper limit to the energy of accelerating electrons. Therefore, electrostatic accelerators are capable of producing low energy x rays such as superficial and orthovoltage x rays. On the other hand, cyclic accelerators, such as linear accelerators (linacs), microtrons, and betatrons, have variable and non-conservative electric fields. Cyclic accelerators can accelerate electrons and produce megavoltage photon beams.

1.3 Classification of Radiation

Based on the ability of ionizing matter, radiation is classified as non-ionizing radiation and ionizing radiation. Ionizing radiation is further divided into directly ionizing radiation and indirectly ionizing radiation. Directly ionizing radiation refers to charged particles, such as electrons, positrons, protons, and heavy ions. The charged particle deposits energy into the medium through direct Coulomb force interaction

between the charged particle and the orbital electrons in the medium. Indirectly ionizing radiation refers to neutral particles such as photons and neutrons. Indirectly ionizing radiation deposits energy in the medium through a two step process. All or part of the energy of the neutral particle is first transferred to a charged particle and the charged particle subsequently deposits its energy through Coulomb force interactions with the orbital electrons in the medium.

1.4 Interactions of photons with a medium

When penetrating a medium, photons undergo various interactions with atoms in the medium, mainly through one of four types of interaction: photoelectric effect, Compton scattering, pair production (nuclear pair production and triplet production), and Rayleigh scattering[2]. Photons may interact with orbital electrons of absorber (Compton scattering and triplet production), with the atomic nucleus of the absorber (nuclear pair production), or with the whole atom of the absorber (photoelectric effect and Rayleigh scattering). During the interaction, photons may be completely absorbed (photoelectric effect, nuclear pair production, and triplet production) or merely scattered (Compton scattering and Rayleigh scattering), and charged particles (electrons and positrons) may be released (photoelectric effect, Compton scattering, nuclear pair production, and triplet production).

1.4.1 Photoelectric effect

The photoelectric effect[2] is an interaction of a photon with the whole atom. The incident photon energy $h\nu$ is absorbed by the atom and the absorbed energy is given to a tightly bound orbital electron. This electron, called a photoelectron, is

ejected from the atom with kinetic energy $E_{\mathrm{K}} = h\nu - E_{\mathrm{B}}$, where E_{B} is the binding energy of the ejected electron.

The mass attenuation coefficient for the photoelectric effect τ/ρ is proportional to Z^3, where Z is the atomic number of the absorber, and inversely proportional to $(h\nu)^3$, hwere $h\nu$ is the incident energy of the photon. The photoelectric effect is the dominant interaction for low energy photons. With increasing the photon energy, the mass attenuation coefficient for the photoelectric effect decreases sharply.

1.4.2 Compton scattering

The Compton scattering[2] is an interaction of a photon with a loosely bound electron. The loosely bound electron refers to an orbital electron with a binding energy E_{B} much smaller than the incident photon energy $h\nu$. In the Compton scattering process, the incident photon is scattered with a lower energy $h\nu'$ and the loosely bound electron is ejected from the atom with kinetic energy $E_{\mathrm{K}} \approx h\nu - h\nu'$.

The mass attenuation coefficient for the Compton scattering σ_{C}/ρ is independent of the atomic number Z of the medium and decreases with increasing incident photon energy $h\nu$. The Compton scattering is the dominant interaction of photons with medium and megavoltage photon beams.

1.4.3 Pair production

Pair production[2] is an interaction of a photon with the Coulomb field of a nucleus (nuclear pair production) or with the Coulomb field of an orbital electron (triplet production). In pair production, the photon disappears and an electron-positron pair is created. Unlike the Compton scattering and Rayleigh scattering, pair production can only occur above a photon threshold energy. For nuclear pair

production, the incident photon energy must be greater than $2m_ec^2 = 1.022$ MeV, where $m_ec^2 = 0.511$ MeV is the rest mass energy of the electron. For triplet production, the threshold energy is $4m_ec^2 = 2.044$ MeV. In nuclear pair production and triplet production, the energy transfered to charged particles is equal to $h\nu - 2m_ec^2$. The transfered energy is shared between the electron-positron pair in nuclear pair production and between three particles (the electron-positron pair and the orbital electron) in triplet production.

The mass attenuation coefficient for the nuclear pair production $\kappa_{\rm pp}/\rho$ is much larger than that for the triplet production $\kappa_{\rm tp}/\rho$, and the sum of $\kappa_{\rm pp}/\rho$ and $\kappa_{\rm tp}/\rho$ is referred to as the pair production mass attenuation κ/ρ. The mass attenuation for the pair production κ/ρ is proportional to the atomic number Z of the medium and increases with the incident photon energy $h\nu$. Pair production is the dominant interaction of photons in the very high energy region, i.e., $\epsilon \gg 1$, where ϵ is the incident photon energy normalized to the rest mass energy of electron, $h\nu/m_ec^2$.

1.4.4 Rayleigh scattering

In Rayleigh scattering[2] the incident photon interacts with the whole atom. After the interaction, the photon is scattered at an angle θ relative to the direction of the incident photon. The whole atom absorbs the transferred momentum, but its recoil energy is very small and the energy of the scattered photon is essentially the same as the energy of the incident photon.

The mass attenuation coefficient for Rayleigh scattering $\sigma_{\rm R}/\rho$ is proportional to the atomic number Z of the medium and inversely proportional to the square of the

incident photon energy, $(h\nu)^2$. Rayleigh scattering is an important interaction in very low energy photon beams and high atomic number medium.

1.5 Mass attenuation coefficient

The total mass attenuation coefficient μ/ρ refers to the sum of the mass attenuation coefficient for the four main photon interactions. The total mass attenuation coefficient μ/ρ is given by the following relationship:

$$\frac{\mu}{\rho} = \frac{\tau}{\rho} + \frac{\sigma_{\mathrm{C}}}{\rho} + \frac{\sigma_{\mathrm{R}}}{\rho} + \frac{\kappa}{\rho}, \tag{1.1}$$

where τ/ρ, σ_{C}/ρ, σ_{R}/ρ, and κ/ρ are the mass attenuation coefficients for photoelectric effect, Compton scattering, Rayleigh scattering, and pair production, respectively. Figure 1–1 shows the total mass attenuation coefficient μ/ρ in water and lead, as well as the mass attenuation coefficient for the four main photon interactions. The photon energy dependence and the atomic number dependence of the mass attenuation coefficients for the four main photon interactions with the medium are summarized in Table 1–1.

	Photoelectric effect	Compton scattering	Rayleigh Scattering	Pair production
Energy dependence	$1/(h\nu)^3$	Decrease with energy	$1/(h\nu)^2$	Increase with energy
Atomic number dependence	Z^3	Z^0	Z	Z

Table 1–1: Dependence of the mass attenuation coefficients for photoelectric effect, Compton scattering, Rayleigh scattering, and pair production on incident photon energy and atomic number of medium.

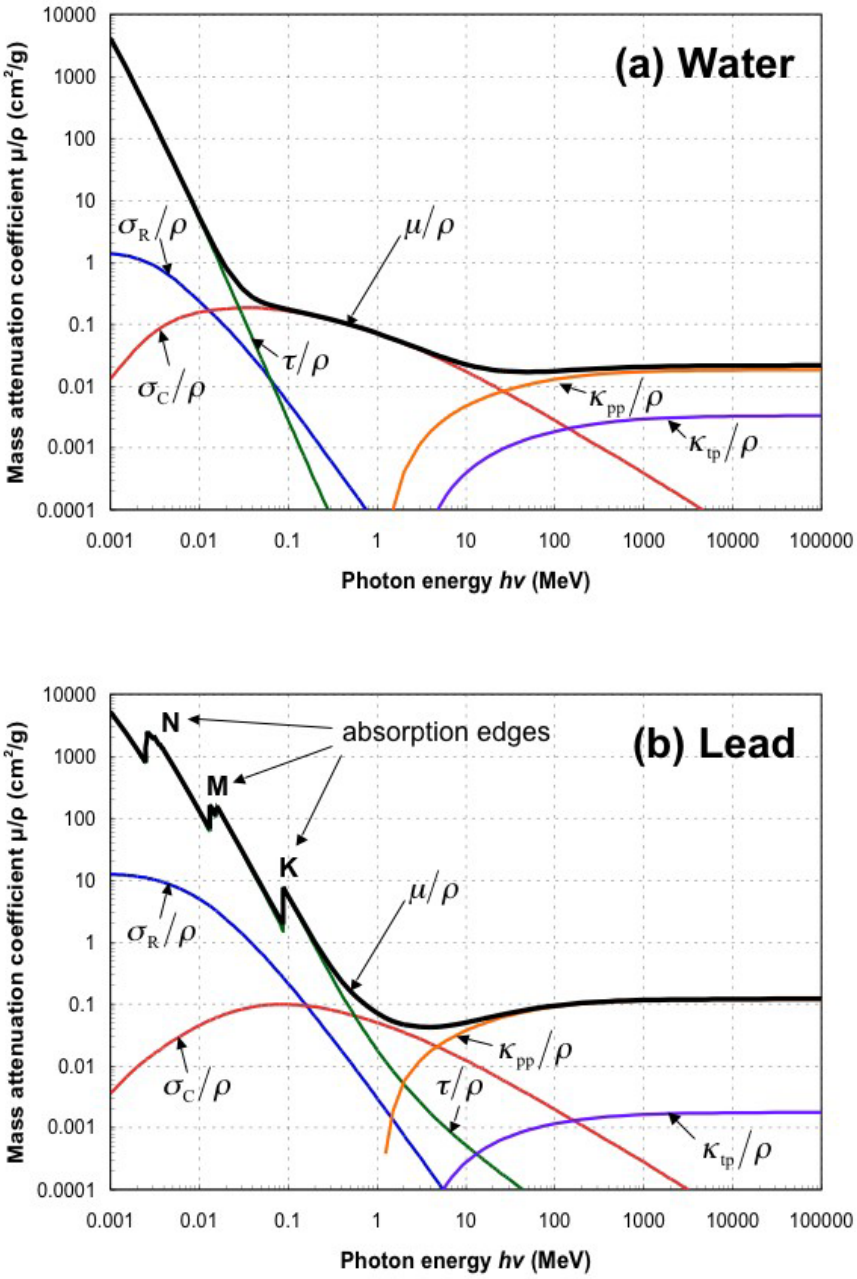

Figure 1–1: The mass attenuation coefficients in (a) water and (b) lead for photoelectric effect τ/ρ, Compton scattering σ_{C}/ρ, Rayleigh scattering σ_{R}/ρ, nuclear pair production $\kappa_{\mathrm{pp}}/\rho$, and triplet production $\kappa_{\mathrm{tp}}/\rho$, as well as the total mass attenuation coefficient μ/ρ.[3]

1.6 Definition of dose

Dose[4–6], or absorbed dose, in medium is defined as the energy imparted by ionizing radiation E_{ab} per unit mass m:

$$D = \frac{dE_{\text{ab}}}{dm}. \tag{1.2}$$

The SI unit of dose is the gray (Gy), i.e., J/kg.

When a phantom is irradiated with an external photon beam source, the absorbed dose at a point of interest in the phantom is deposited by two types of photons: (i) photons emitted directly by the source (primary photons) and (ii) photons produced after a scattering event of a primary photon (scattered photons). The scattering event of primary photons may take place in the treatment head, in the air between the source and the phantom, or in the phantom itself. The absorbed dose at the point of interest in the phantom may be divided into two components: primary dose component and scatter dose component. The primary and scatter dose components should logically be associated with primary photons and scattered photons, respectively. However, in dosimetric calculations, the scatter dose component is only associated with scattered photons produced within the phantom. Scattered photons produced from the treatment head and from the air above the phantom are categorized as primary photons, thus, contribute to the primary dose component rather than the scatter dose component. Therefore, the term "primary photons" is used for "true" primary photons as well as photons produced from the radiation source and then scattered outside of the phantom. The term "scattered photons"

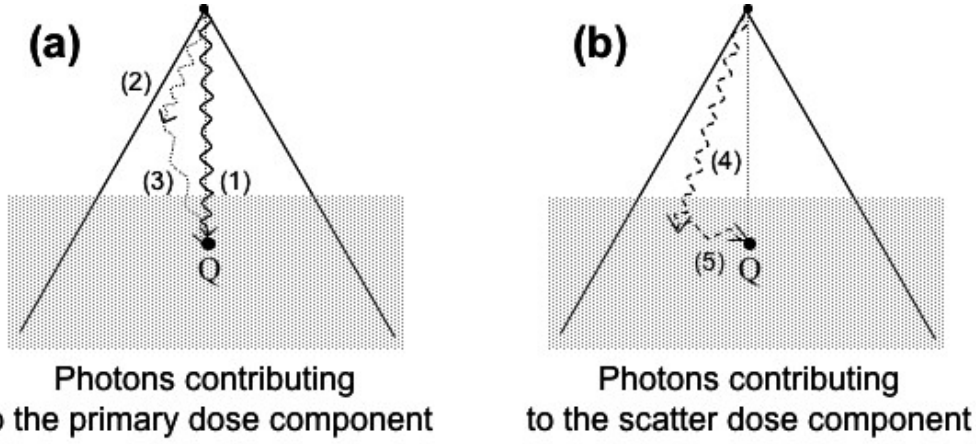

Figure 1–2: The absorbed dose at point Q in a phantom is divided into primary dose component and scatter dose component. The primary dose component is deposited by photon (1) emitted by the radiation source or photon (3) produced after primary photon (2) has undergone a scattering event outside of the phantom. Photon (5) is produced after primary photon (4) is scattered within the phantom. The dose deposited at point Q from photon (5) contributes to the scatter dose component.

is used only for photons produced from the radiation source but have undergone a scattering event within the phantom.

1.6.1 The primary dose component

In a phantom, the primary dose component decreases with depth and this decrease is governed by two effects, namely, the attenuation of primary photons with depth in the phantom and the decrease in the primary photon fluence as a function of distance from the source.

Attenuation law for photon beams

For a monoenergetic photon beam with energy $h\nu$, the intensity of photon beams $I(x)$ after passing a thickness x of an attenuator is governed by the following relationship:

$$I(x) = I(0)e^{-\mu x}, \tag{1.3}$$

where $I(0)$ is the intensity of the photon beam without the attenuator, and μ is the linear attenuation coefficient of the attenuating medium for photon energy $h\nu$. The linear attenuation coefficient μ is thus a function of the photon beam energy and the traversed medium and is equal to the product of the mass attenuation coefficient μ/ρ and the physical density of the medium μ.

The half-value layer (HVL) of an attenuator is the thickness of the attenuator required to decrease the intensity of the photon beam to half of its initial intensity. The HVL is related to the linear attenuation coefficient μ by:

$$\text{HVL} = \frac{\ln 2}{\mu}. \tag{1.4}$$

For a polyenergetic photon beam, photons with different energies are attenuated differently and the attenuation of the beam intensity is usually described either by using an effective linear attenuation coefficient μ_{eff} or by using a variable linear attenuation coefficient depending on the depth. For the latter situation, the attenuation law becomes:

$$I(x) = I(0)e^{-\mu x(1-\eta x)}, \tag{1.5}$$

where the parameter η is referred to as the beam hardening coefficient.

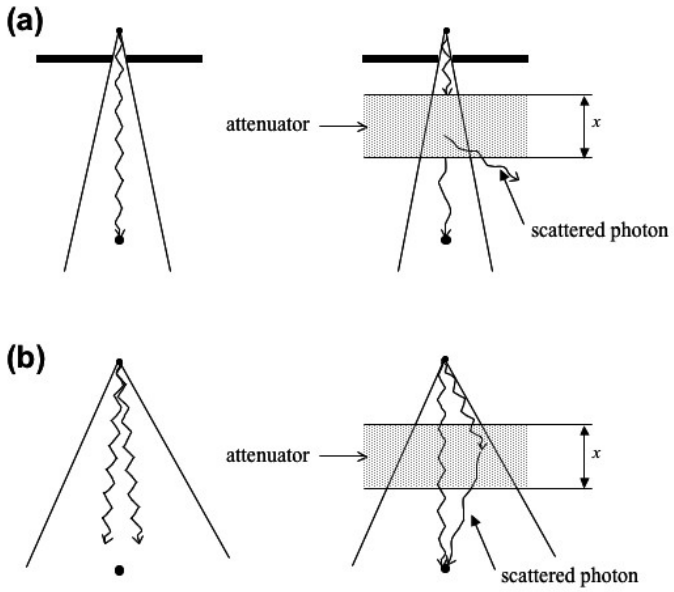

Figure 1–3: Schematics of (a) narrow beam geometry and (b) broad beam geometry.

Measurements of the linear attenuation coefficient μ and the beam hardening coefficient are carried out under a narrow beam geometry, as shown in Fig. 1–3. In the narrow beam geometry, the number of photons scattered from the attenuator and reaching the detector is minimized, and the measured signal by the detector is primarily due to photons transmitted through the attenuator.

Inverse square law

The inverse square law states that the photon fluence ϕ, which is defined as the number of photons crossing unit area, is inversely proportional to the square of the distance from the radiation source. The inverse square law is illustrated using Fig. 1–4, where S is a photon source producing a square field with area A at distance f_a. Area A is geometrically related to area B through:

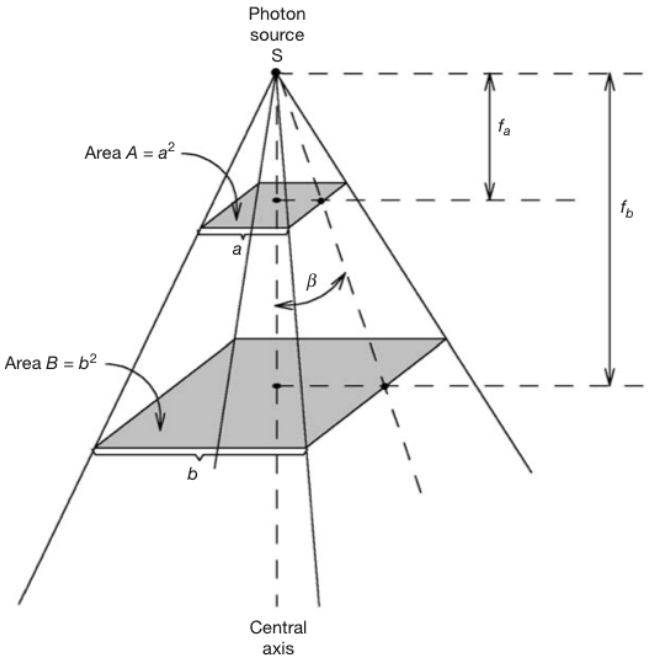

Figure 1–4: Divergence of a point source photon beam.[4]

$$\frac{A}{B} = \frac{{f_a}^2}{{f_b}^2}, \tag{1.6}$$

where f_b is the distance from the photon source S to area B. With the assumption that there is no interaction of photons between area A and area B, the number of photons N crossing area A is equal to the number of photons crossing area B:

$$N = \phi_A A = \phi_B B. \tag{1.7}$$

Therefore, the ratio of the photon fluence ϕ_A in area A to the photon fluence ϕ_B in area B is given by the following relationship:

$$\frac{\phi_A}{\phi_B} = \frac{B}{A} = \frac{{f_b}^2}{{f_a}^2}. \tag{1.8}$$

1.6.2 The scatter dose component

The scatter dose component at a point in a phantom depends on the field size. For a larger field size, more phantom material is irradiated by the photon beam, increasing the number of scattered photons. Hence, with increase in field size, the scatter dose component at the point of interest increases.

1.7 Dosimetry in radiotherapy

The determination of the 3-D dose distribution in the phantom or the patient in radiotherapy is referred to as clinical dosimetry. The 3-D dose distribution is determined by first determining the dose at a reference geometrical point (absolute beam dosimetry or beam calibration), and then using a number of relative dosimetric functions that relate the dose at a point of interest to the dose at a reference point.

1.7.1 Absolute beam dosimetry

Absolute beam dosimetry is the process of determining the absorbed dose at a reference point in a reference geometry setup in the air or in the phantom. Several methods have been developed for absolute beam dosimetry. Through measuring the temperature rise due to energy deposition in a medium, calorimetry is considered as the most fundamental method of determining the absorbed dose. The absorbed dose may also be determined with Fricke dosimetry by measuring the chemical reaction of ferrous sulphate solutions in Fricke gel with energy deposition or ionization chamber dosimetry, where the absorbed dose is determined from the charge collected in the ionization chamber's air volume and a recognized dosimetry protocol, such as the AAPM TG-51[7] and IAEA TRS-398[8] protocols.

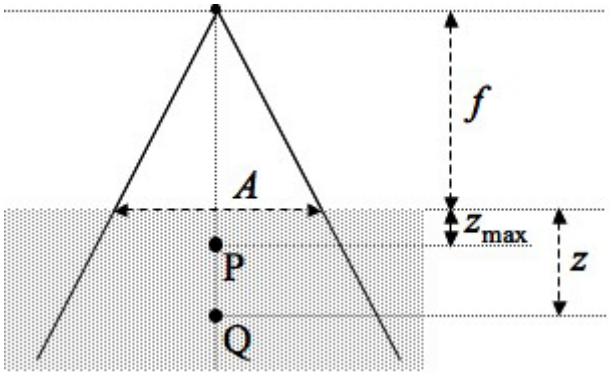

Figure 1–5: Schematic definition of the PDD. The PDD at point Q is defined as the quotient of the total absorbed dose at point Q to the total absorbed dose at point P.

1.7.2 Relative dosimetry functions

Percent depth dose

The percentage depth dose PDD[4–6] is defined as the ratio of the total absorbed dose in phantom at a given point Q along the beam central axis to the total absorbed dose at point P which is at the depth of maximum dose $z_{\max}$. As illustrated in Fig. 1–5, the PDD at the point Q is given by the following relationship:

$$\mathrm{PDD}(z, A, f, h\nu) = \frac{D_{\mathrm{Q}}(z, A, f, h\nu)}{D_{\mathrm{P}}(z_{\max}, A, f, h\nu)} \times 100, \tag{1.9}$$

where z is the depth of point Q, A is the field size determined at the phantom's surface, f is the source-surface distance, and $h\nu$ is the energy of the incident photon beam.

Figure 1–6 shows PDD curves versus depth z in water for photon beam energies ranging from 3.0 mm Cu HVL to 25 MV. The PDD has a non-zero value at the phantom surface, increases with increasing z, and then reaches a maximum at the depth of maximum dose $z_{\max}$. For superficial and orthovoltage photon beams, such

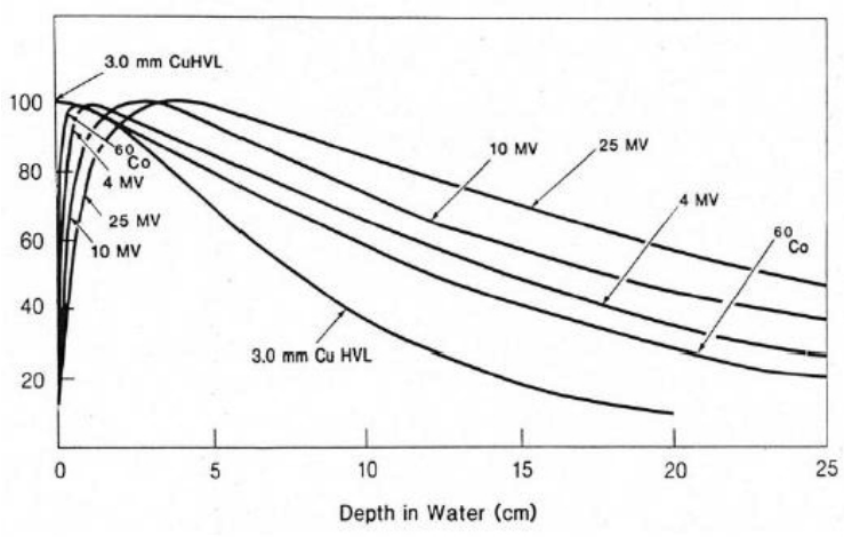

Figure 1–6: PDD curves for various photon beams.[6]

as 3 mm Cu HVL photon beam in Fig. 1–6, $z_{\max}$ occurs at the surface of the phantom, thus, the PDD does not exhibit a dose build-up near the surface. For ^{60}Co and megavoltage photon beams, $z_{\max}$ is beyond the surface of the phantom, and the region where the PDD increases between the surface ($z = 0$) and $z_{\max}$ is called the build-up region. Beyond $z_{\max}$, the PDD decreases in an exponentially like manner. The decrease in the PDD is attributed to the attenuation of photons in the phantom as well as to the decrease of photon fluence as governed by the inverse square law.

Depth of maximum dose $z_{\max}$

The depth of maximum dose $z_{\max}$ refers to the depth at which the maximum dose along the beam central axis in the phantom occurs. It depends primarily on the energy of the photon beam but a small dependence is also observed with respect to the field size. With respect to the photon beam energy, $z_{\max}$ is zero for superficial

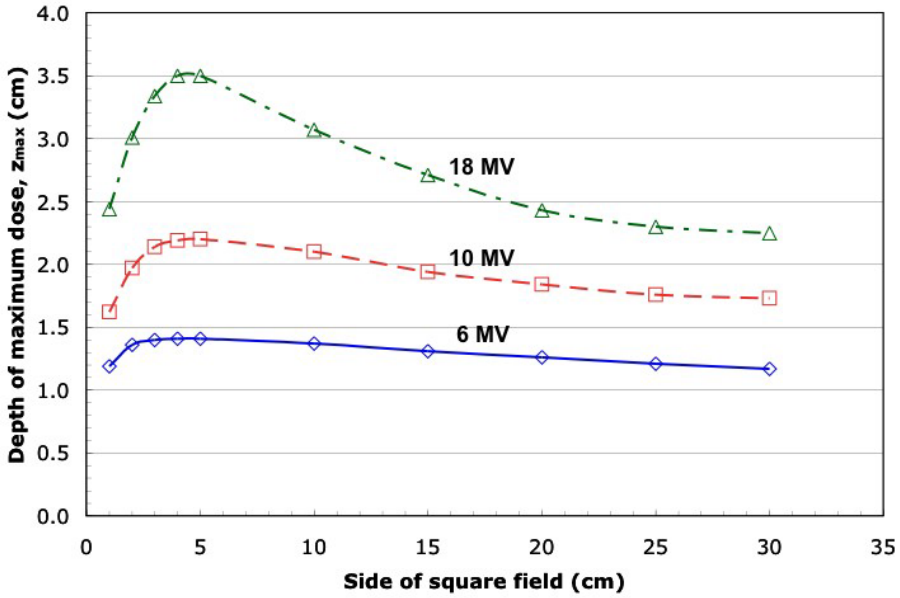

Figure 1–7: Depth of maximum dose, $z_{\max}$, as a function of field size for 6 MV, 10 MV, and 18 MV photon beams[9].

and orthovoltage beams and then gradually increases with increasing photon beam energy.

Figure 1–7 shows the variation of $z_{\max}$ with the field size for 6 MV, 10 MV, and 18 MV photon beams measured by Sixel *et al.*[9] With respect to the field size, the maximum $z_{\max}$ for a given photon beam energy occurs at 5×5 cm^2 field size. For fields smaller than 5×5 cm^2, the decrease of $z_{\max}$ is due to the in-phantom scatter effect and the decrease of $z_{\max}$ for fields larger than 5×5 cm^2 is attributed to collimator and flattening filter scatter effects.[9] As shown in Fig. 1–7, the change of $z_{\max}$ against the field size becomes larger with increasing photon energy. However, since the field size has a minor effect on $z_{\max}$, the dependence of $z_{\max}$ on the field

Photon energy	$z_{\max}$(cm)
superficial	0
orthovoltage	0
^{137}Cs	0.12
^{60}Co	0.5
4 MV	1
6 MV	1.5
10 MV	2.5
18 MV	3.0–3.5

Table 1–2: Nominal $z_{\max}$ listed in the BJR Supplement 25[10] for various photon beams.

size is usually ignored. Table 1–2 lists the nominal $z_{\max}$ for various photon beam energies as published in British Journal of Radiology Supplement 25[10].

Tissue-air ratio and tissue-maximum ratio

The definition of the tissue-air ratio TAR has evloved through several stages, which are further discussed in Chapter 2. The latest accepted definition of the TAR is given in the BJR Supplement 17[11]. As schematically shown in Fig. 1–8, the TAR at point Q is defined as the quotient of the total absorbed dose along the beam central axis at point Q, divided by the primary dose at $\mathrm{Q}_{\max}$. The TAR at point Q for depth z and field size A_{Q} is given by the following relationship:

$$\mathrm{TAR}(z, A_{\mathrm{Q}}, h\nu) = \frac{D_{\mathrm{Q}}(z, A_{\mathrm{Q}}, h\nu)}{D^{\mathrm{pri}}_{\mathrm{Q}_{\max}}(A_{\mathrm{Q}}, h\nu)}, \tag{1.10}$$

where $D_{\mathrm{Q}}(z, A_{\mathrm{Q}}, h\nu)$ is the total absorbed dose at point Q for depth z and field size A_{Q} and $D^{\mathrm{pri}}_{\mathrm{Q}_{\max}}(A_{\mathrm{Q}}, h\nu)$ is the primary dose at the point $\mathrm{Q}_{\max}$ for depth $z_{\max}$ and field size A_{Q}. Points Q and $\mathrm{Q}_{\max}$ are at the same distance from the source and A_{Q} is the field size at Q and at $\mathrm{Q}_{\max}$.

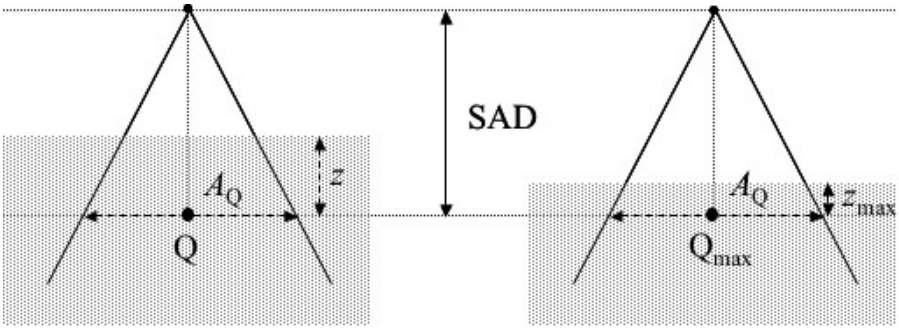

Figure 1–8: Schematic definition of the TAR from the BJR Supplement 17[11]. The TAR is defined as the ratio of the total absorbed dose at point Q to the primary dose at point Q_{max}.

The ratio of the total absorbed dose at point Q to the total absorbed dose at point Q_{max} is defined as the tissue-maximum ratio TMR[4–6, 11]:

$$\mathrm{TMR}(z, A_Q, h\nu) = \frac{D_Q(z, A_Q, h\nu)}{D_{Q_{max}}(A_Q, h\nu)}, \tag{1.11}$$

where $D_{Q_{max}}(A_Q, h\nu)$ is the total absorbed dose at Q_{max}.

Peak scatter factor

The peak scatter factor PSF[10, 11] is a special case of the TAR when the depth of point Q in Fig. 1–8 is equal to z_{max}. The PSF at point Q_{max} for field size A_Q, as illustrated schematically in Fig. 1–9, is given by the following relationship:

$$\mathrm{PSF}(A_Q, h\nu) = \frac{D_{Q_{max}}(z_{max}, A_Q, h\nu)}{D^{pri}_{Q_{max}}(A_Q, h\nu)}, \tag{1.12}$$

where $D_{Q_{max}}(z_{max}, A_Q, h\nu)$ is the total absorbed dose at the point Q_{max} for depth z_{max} and field size A_Q and $D^{pri}_{Q_{max}}(A_Q, h\nu)$ is the primary dose at the point Q_{max}. Since z_{max} is zero for low energy photon beams, the scatter dose at the point Q_{max}

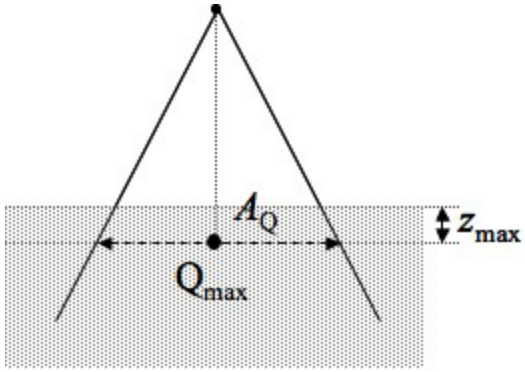

Figure 1–9: Schematic definition of the PSF. The PSF is defined as the ratio of the total dose to the primary dose at point Q_{max}.

is essentially from photons back scattered from the phantom. Hence, the PSF is referred to as the back scatter factor BSF for low energy photon beams.

Figure 1–10 shows the variation of the PSF against photon energies for different radiation field sizes. With respect to the photon beam energy, the PSF increases at first with increasing photon beam energy; reaches a maximum at about a photon beam energy equivalent to HVL=0.4 mm Cu; then decreases with further increase in the photon beam energy. The initial increase in the PSF is due to the increase in the relative number of scattered photons (Compton effect). As the energy further increases, the Compton scattered photons are more forwardly scattered with respect to the direction of incident photons, and the PSF decreases with further increase of the energy of photon beams after the 0.4 mm Cu HVL photon beam.

With respect to field size, the PSF increases with increase in the field size. With larger field size, more phantom material is irradiated by the field and more scattered photons are produced, thereby the total absorbed dose at Q_{max} increases.

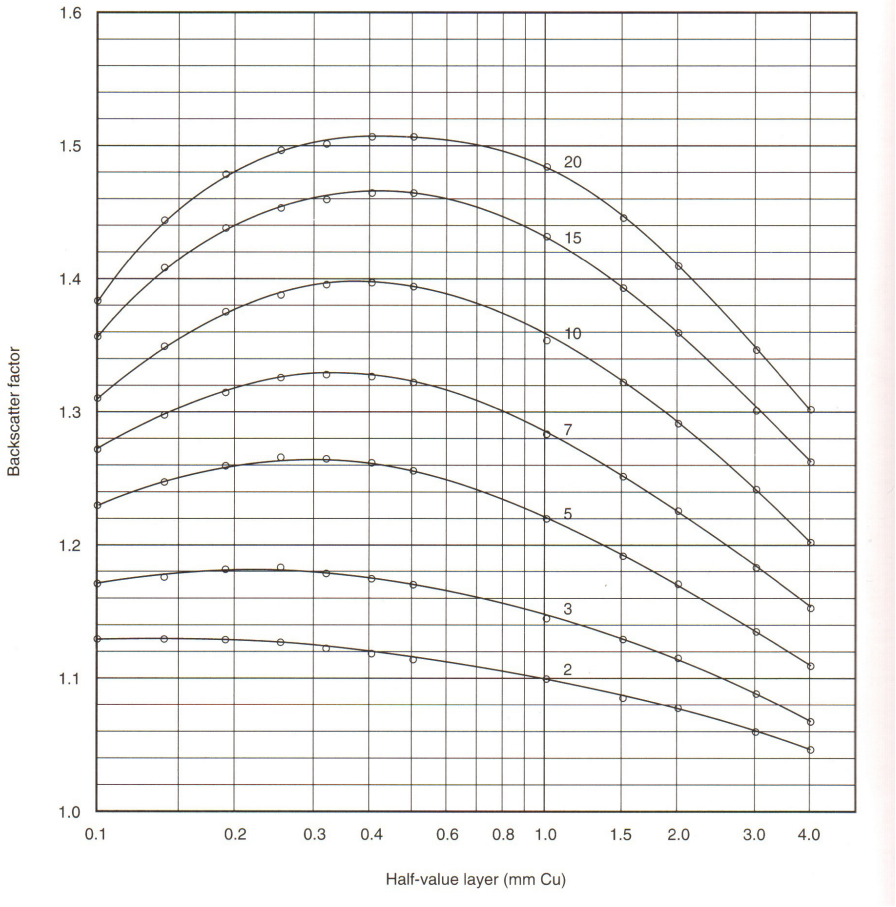

Figure 1–10: Variation of PSF (BSF for low energy photon beams) against energy of photon beams represented by Half-value layer in the range of 0.1 to 4.0 mm Cu for various square field sizes.[10]

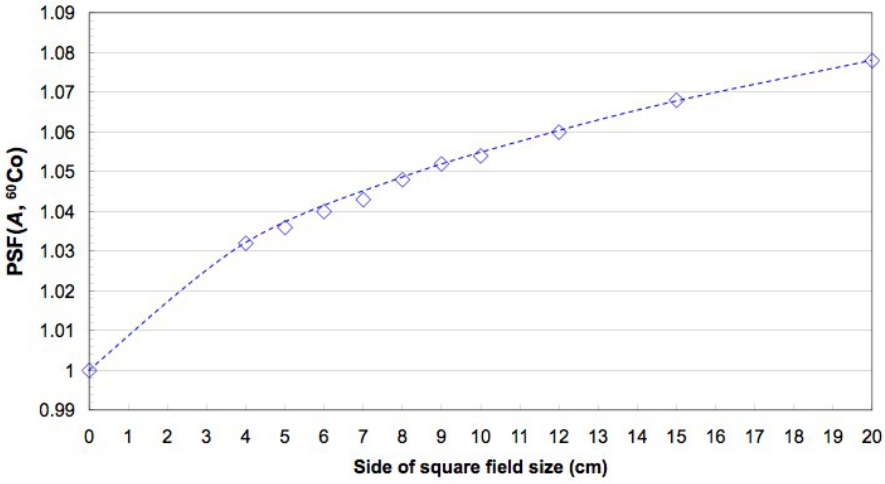

Figure 1–11: PSF for ^{60}Co from BJR Supplement 25[10].

Figure 1–11 plots the PSF for ^{60}Co beam against field size ranging from 0×0 cm^2 to 20×20 cm^2. The PSFs for ^{60}Co are taken from the BJR Supplement 25[10].

For megavoltage photon beams, where it is hard to measure the primary dose at the point $\mathrm{Q}_{\max}$ directly, the BJR Supplements 17[11] and 25[10] suggested using the normalized peak scatter factor NPSF in radiotherapy dosimetry. As shown in Fig. 1–12, the NPSF at the point $\mathrm{Q}_{\max}$ for field size A_{Q} is defined as:

$$\mathrm{NPSF}(A_{\mathrm{Q}}, h\nu) = \frac{\mathrm{PSF}(A_{\mathrm{Q}}, h\nu)}{\mathrm{PSF}(A_{\mathrm{Q}_{\mathrm{ref}}}, h\nu)}, \tag{1.13}$$

where $\mathrm{PSF}(A_{\mathrm{Q}}, h\nu)$ is the PSF at the point $\mathrm{Q}_{\max}$ for field size A_{Q} and $\mathrm{PSF}(A_{\mathrm{Q}_{\mathrm{ref}}}, h\nu)$ is the PSF for a reference field size $A_{\mathrm{Q}_{\mathrm{ref}}}$.

Relative dose factor and collimator factor

The relative dose factor RDF[4–6] is defined as the ratio of the total absorbed dose at $z_{\max}$ for a given field size to the total absorbed dose at $z_{\max}$ for a reference

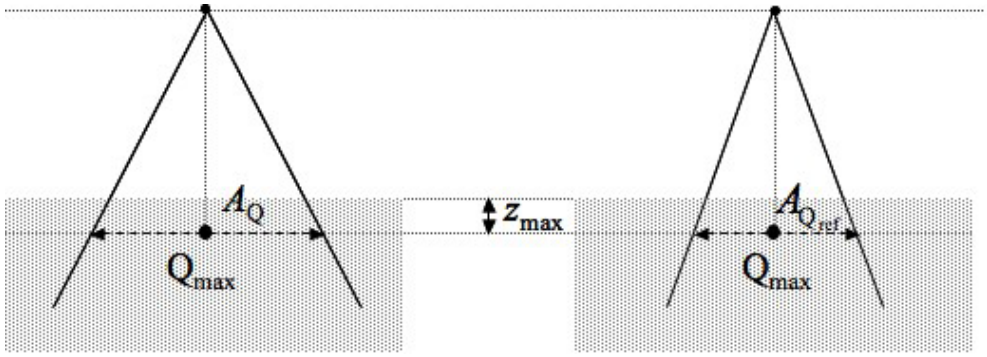

Figure 1–12: Schematic definition of the normalized peak scatter factor NPSF, the relative dose factor RDF, and the collimator factor CF. The NPSF is the ratio of the PSF for field size A_Q to that for a reference field size $A_{Q_{ref}}$; the RDF is the ratio of the total absorbed dose at z_{max} for field size A_Q to that for the reference field size $A_{Q_{ref}}$; and the CF is the ratio of the primary dose at z_{max} for field size A_Q to that for the reference field size $A_{Q_{ref}}$.

field size. Based on Fig. 1–12, the RDF at the point Q_{max} for the field size A_Q is given by the following relationship:

$$\mathrm{RDF}(A_Q, h\nu) = \frac{D_{Q_{max}}(z_{max}, A_Q, h\nu)}{D_{Q_{max}}(z_{max}, A_{Q_{ref}}, h\nu)}, \tag{1.14}$$

where $D_{Q_{max}}(z_{max}, A_Q, h\nu)$ is the total absorbed dose at point Q_{max} for field size A_Q and $D_{Q_{max}}(z_{max}, A_{Q_{ref}}, h\nu)$ is the total absorbed dose at point Q_{max} for the reference field size $A_{Q_{ref}}$.

The collimator factor CF describes the change in the primary dose at Q_{max} due to the change of the collimator settings. Based on Fig. 1–12, the CF for field size A_Q in the phantom is defined by the following relationship:

$$\mathrm{CF}(A_Q, h\nu) = \frac{D^{pri}_{Q_{max}}(A_Q, h\nu)}{D^{pri}_{Q_{max}}(A_{Q_{ref}}, h\nu)}, \tag{1.15}$$

where $D^{\text{pri}}_{\text{Q}_{\text{max}}}(A_{\text{Q}}, h\nu)$ is the primary dose at the point Q_{max} for field size A_{Q} and $D^{\text{pri}}_{\text{Q}_{\text{max}}}(A_{\text{Q}_{\text{ref}}}, h\nu)$ is the primary dose at the same point for the reference field size $A_{\text{Q}_{\text{ref}}}$.

From Eq. 1.13 and Eq. 1.15, the RDF can be rewritten as:

$$\text{RDF}(A_{\text{Q}}, h\nu) = \frac{D^{\text{pri}}_{\text{Q}_{\text{max}}}(A_{\text{Q}}, h\nu) \times \text{PSF}(A_{\text{Q}}, h\nu)}{D^{\text{pri}}_{\text{Q}_{\text{max}}}(A_{\text{Q}_{\text{ref}}}, h\nu) \times \text{PSF}(A_{\text{Q}_{\text{ref}}}, h\nu)} = \text{CF}(A_{\text{Q}}, h\nu) \times \text{NPSF}(A_{\text{Q}}, h\nu). \tag{1.16}$$

Equation 1.16 indicates that the RDF includes the change of the scatter dose from the collimator settings (CF) and from the phantom (NPSF).

1.8 Thesis objectives and outline

The purpose of this project is to measure the PSF for the 10×10 cm^2 field size in 6 MV and 18 MV photon beams. The PSF for the 10×10 cm^2 field size is measured in Solid Water$^{\text{TM}}$ by following recommendations presented in the BJR Supplements 17[11] and 25[10]. The measured PSF(10, $h\nu$) is compared to the PSF$(10, h\nu)$ calculated with Monte Carlo methods. In addition, the effect of the build-up cap material density on the measurements is examined. Four build-up cap materials, namely, Lucite$^{\text{TM}}$, aluminum, brass, and copper, are studied.

In addition to chapter 1, this thesis contains four additional chapters. Chapter 2 reviews the modifications to the definitions of the TAR and the PSF. Chapter 3 describes the materials, experimental setups, and Monte Carlo methods used in this project. Then, chapter 4 reports the results of the measurements and the Monte Carlo calculations. Chapter 5 provides a summary and conclusions for this work and recommendations for future work.

REFERENCES

[1] International Commission on Radiation Units and Measurements (ICRU). *Determination of absorbed dose in a patient irradiated by beams of X or gamma rays in radiotherapy procedures,* Report 24. International Commission on Radiation Units and Measurements, Washington, DC, 1976.

[2] E. B. Podgoršak. *Radiation Physics for Medical Physicists*. Springer, Heidelberg, Germany, 2006.

[3] M. J. Berger, J. H. Hubbell, S. M. Seltzer, J. Chang, J. S. Coursey, R. Sukumar, and D. S. Zucker. *XCOM: Photon cross section database*, NBSIR 87-3597. National Institute of Standard and Technology, 2005. Available from *http://physics.nist.gov/PhysRefData/Xcom/Text/XCOM.html*.

[4] E. B. Podgorsak, editor. *Radiation Oncology Physics: A Handbook for Teachers and Students*. International Atomic Energy Agency, Vienna, Austria, 2005.

[5] H. E. Johns and J. R. Cunningham. *The Physics of Radiology,* 4th edition. Charles C. Thomas, Springfield, IL, 1983.

[6] F. A. Khan. *The Physics of Radiation Therapy,* 3rd edition. Lippincott Williams & Wilkins, Philadelphia, PA, 2003.

[7] P. R. Almond, P. J. Biggs, B. M. Hanson W. F. Coursey, Huq. M. S., R. Nath, and D. W. O. Rogers. AAPM's TG-51 protocol for clinical reference dosimetry of high-energy photon and electron beams. *Medical Physics*, 26:1847–1870, 1999.

[8] International Atomic Energy Agency (IAEA). *Absorbed dose determination in external beam radiotherapy: An international code of practice for dosimetry based on standards of absorbed dose to water,* Technical Report Series No. 398.

International Atomic Energy Agency, Vienna, Austria, 2000.

[9] K. E. Sixel and E. B. Podgorsak. Buildup region and depth of dose maximum of megavoltage x-ray beams. *Medical Physics*, 21:411–416, 1994.

[10] British Journal of Radiology. *Central axis depth dose data for use in radiotherapy: 1996,* Supplement 25. The British Institute of Radiology, London, UK, 1996.

[11] British Journal of Radiology. *Central axis depth dose data for use in radiotherapy,* Supplement 17. The British Institute of Radiology, London, UK, 1983.

CHAPTER 2
Background

2.1 Early definitions of the tissue-air ratio and the peak scatter factor

The concept of the TAR was first suggested by Johns *et al.*[1] in 1953. Because of its independence of the source-axis distance (SAD), the TAR was first used in the dosimetry of rotational beam radiotherapy and was later applied in conventional stationary beam radiotherapy. In the early days, the TAR[1] was defined as the ratio of the exposure along the beam central axis at depth z in a phantom to the exposure in air at the same distance from the radiation source. As shown schematically in Fig. 2–1, the TAR at point Q for depth z and field size A_{Q} defined at point Q was given by the following relationship:

$$\mathrm{TAR}(z, A_{\mathrm{Q}}, h\nu) = \frac{X_{\mathrm{Q}}}{X_{\mathrm{Q}'}}, \tag{2.1}$$

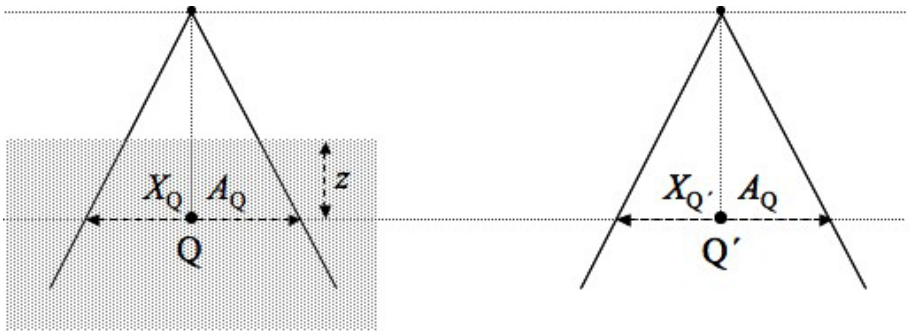

Figure 2–1: Schematic definition of the TAR from Johns *et al.*[1] The TAR at point Q was defined as the ratio of the exposure at point Q to the exposure at point Q′.

where X_{Q} is the exposure at point Q in the phantom and $X_{\mathrm{Q}'}$ is the exposure at point Q$'$ in air at the same distance from the radiation source.

The calibration of external radiotherapy photon beam was usually based on determining the exposure or exposure rate at a distance from the radiation source. The back scatter factor BSF was used to relate the exposure in air to the exposure on a patient's or phantom surface at the same field size A_{Q} and the same distance from the source. The BSF was defined as the ratio of the exposure at a phantom surface to the exposure in space (air) at the same distance from the source. Hence, the TAR at the surface ($z = 0$) is equal to the BSF.

2.2 International Commission on Radiation Units and Measurements, Report 10d

The ICRU Report 10d[2], published in 1962, was a reference document for clinical dosimetry. The report included procedures for the calibration of external radiotherapy beams, definitions of fundamental relative dosimetric functions, and methods for the determination of the dose distribution in patients.

As the absorbed dose quantity became more commonly used to quantify radiation in radiotherapy, the definition of the TAR was modified. According to the ICRU Report 10d[2], the TAR was defined as the ratio of *the absorbed dose* at a given point in the phantom to *the absorbed dose* in a small mass of tissue in air at the same distance from the source. As schematically shown in Fig. 2–2, the TAR at point Q for depth z and field size A_{Q} was given as follows:

$$\mathrm{TAR}(z, A_{\mathrm{Q}}, h\nu) = \frac{D_{\mathrm{Q}}}{D_{\mathrm{Q}'}}, \tag{2.2}$$

where D_{Q} is the absorbed dose measured at point Q for depth z and field size A_{Q} in

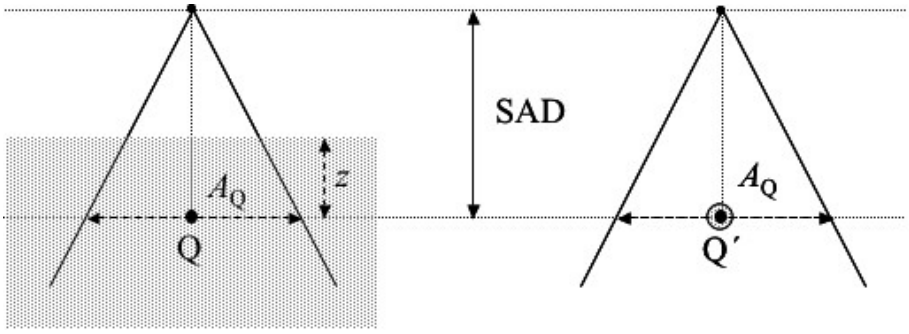

Figure 2–2: Schematic definition of the TAR from ICRU Report 10d[2]. The TAR at point Q was defined as the ratio of the absorbed dose at point Q in the phantom to the absorbed dose at point Q′ in the small mass of tissue in air.

the phantom and $D_{Q'}$ is the absorbed dose in the small mass of tissue in air at point Q′ for field size A_Q. The dimensions of the small mass of tissue must be sufficiently large to establish electronic equilibrium at point Q′.

The ICRU Report 10d[2] also introduced a relative dosimetric function called the scatter factor SF. The SF was defined as the ratio of the exposure at *a reference point* in the phantom to the exposure at the same distance in air "under similar conditions of irradiation in the absence of the phantom". For photon energies less than 400 kVp, the reference point at which the SF was defined was at the phantom surface ($z = 0$) and the SF in this situation was referred to as the back scatter factor BSF. For photon energies above 400 kVp, the reference point was taken at the depth of maximum dose $z_{\max}$.

The definition of the SF as given by the ICRU Report 10d[2] was not clear among medical physicists when applied to photon energies above 400 kVp. There were two interpretations of the statement "the exposure in air under similar condition of irradiation in the absence of the phantom". The first interpretation was

that the above statement implied that the in-air exposure must be measured for an attenuated beam. Hence, the measurement of the exposure in air must be carried out with the presence of an attenuator (build-up cap) with a thickness equivalent to $z_{\max}$. The second interpretation of the statement, supported by Cunningham *et al.*[3], suggested that the in-air exposure measurement should be carried out without the presence of an attenuator. Cunningham *et al.*[3] also pointed out that in the absence of an attenuator in the in-air measurement, the resulting SF for high energy photon beams for 0×0 cm^2 field size would be less than one. Cunningham *et al.*[3] suggested correcting the in-air exposure measurement with a factor that accounts for the attenuation of the photon beam through the thickness $z_{\max}$ in order to (i) avoid having the SF less than unity for 0×0 cm^2 field size and (ii) maintain the equality of the TAR at $z_{\max}$ and the SF.

2.3 British Journal of Radiology Supplement 11

The BJR Supplement 11[4], published in 1972, contained reference dosimetric data for photon beams ranging from 6 kVp to 35 MV. The document also contained updated definitions of the various dosimetric functions, such as the PDD, the TAR, and the SF, which are used in radiotherapy.

In the BJR Supplement 11[4], the definition of the TAR was not changed from that defined in the ICRU Report 10d[2]. The TAR definition remained as the quotient of the absorbed dose at depth z in the phantom to the dose in a small mass of tissue in air at the same distance from the radiation source. The BJR Supplement 11[4], however, modified the definition of the SF. The new definition of the SF was proposed to avoid the ambiguity of the ICRU Report 10d SF definition. Following

the suggested definition, given by the ICRU Report 23[5] which was published a year later, the definition of the SF was given as the ratio of the exposure (or of *the absorbed dose*) at a reference point in a phantom to the part of that exposure (or *absorbed dose*) *which is due to primary photons*. For photon beams generated with a potential lower than 400 kV, the reference point was at the phantom surface and the SF was called the BSF. For photon beams with energy higher than 400 kVp, the reference point was defined at $z_{\max}$. The BJR Supplement 11[4] emphasized that the numerical value of the BSF was equal to that of the TAR at $z_{\max}$.

The BJR Supplement 11[4] pointed out that the "BSF" term should be restricted for photon beams generated with potentials lower than 400 kV. The document argued that, since the reference point $z_{\max}$ is located below the phantom surface for higher energy photon beams, the SF includes dose contribution from the forward scattered photons originating in the layers above $z_{\max}$ in the phantom in addition to back scattered photons produced at depths greater than $z_{\max}$. Yet, the BSF term, instead of the SF, was still used in labelling tabulated data for high energy photon beams, such as ^{137}Cs, ^{60}Co, and 2 MV.

2.4 International Commission on Radiation Units and Measurements, Report 23

The ICRU Report 23[5], published in 1973 as a revision to the ICRU Report 10d[2], addressed methods to determine the absorbed dose distribution in photon beams using absolute and relative dosimetry techniques.

The TAR definition in this report was not changed from that in the ICRU Report 10d[2]. The SF, on the other hand, was defined as the ratio of the exposure (or of the absorbed dose) at *a point* in a phantom to the part of that exposure (or

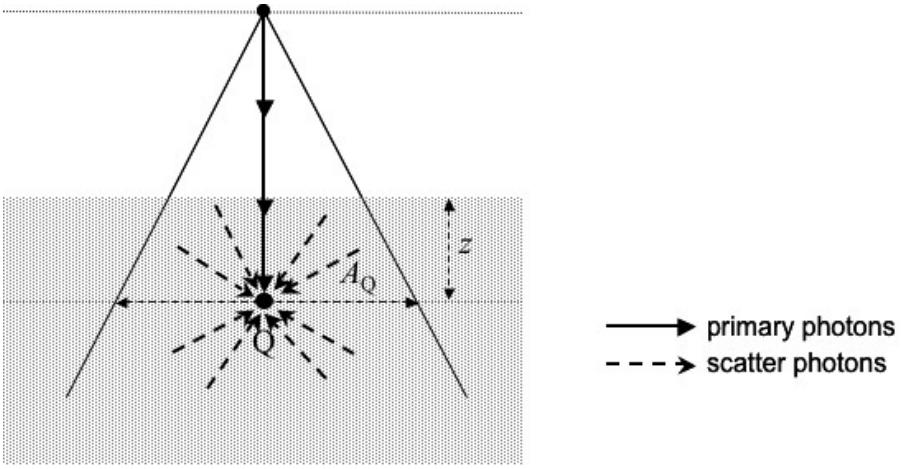

Figure 2–3: Schematic definition of the SF according to the ICRU Report 23[5]. The SF at point Q was defined as the ratio of the total exposure to the primary exposure at point Q or the ratio of the total absorbed dose to the primary dose at point Q.

absorbed dose) which is due to primary photons. Based on Fig. 2–3, the SF at point Q for depth z and field size A_Q is given by the following relationship:

$$\mathrm{SF}(z, A_Q, h\nu) = \frac{X_Q}{X_Q^{\mathrm{pri}}} = \frac{D_Q}{D_Q^{\mathrm{pri}}}, \tag{2.3}$$

where X_Q and X_Q^{pri} are the total and primary exposures at point Q, respectively, and D_Q and D_Q^{pri} are the total and primary doses at point Q, respectively. There were two modifications in the ICRU 23 definition of the SF. The first modification is that the definition of the SF is based on the primary dose concept. This modification in the SF definition was also present in the BJR Supplement 11[4], which was published a year earlier. The second modification to the definition of the SF presented by the ICRU Report 23[5] was that the SF definition can be applied to any point in the phantom instead of being restricted to the point at depth of maximum dose $z_{\max}$.

Similarly to the BJR Supplement 11[4], the SF at $z = 0$ for photon beams less than 400 kVp was called the BSF. For higher energy photon beams, the SF at $z_{\max}$ was called the *peak scatter factor* PSF. The BSF for lower energy photon beams and the PSF for higher energy photon beams are numerically equal to the TAR at $z = 0$ and the TAR at $z = z_{\max}$, respectively.

2.5 British Journal of Radiology Supplement 17

The BJR Supplement 17[6] was published in 1983 as a revision of the BJR Supplement 11[4]. In the document, reference dosimetric data, which was compiled from various radiotherapy units made by different manufacturers for photon beams, were expanded to include beams with energies up to 43 MV.

The BJR Supplement 17[6] criticized the ICRU Report 23 definition of the TAR and pointed out four defects in the definition: (i) The size and shape of the small mass of tissue in air were not specified, (ii) The absorbed dose within the small mass of tissue in air includes contribution from the scattered radiation within the small mass. This scatter dose contribution is not negligible specially for high energy photon beams. Hence, it was not clear if the "dose in a small mass of tissue in air" concept, which was used in the definition of the TAR by the ICRU Report 23[5], includes the scatter dose contribution or not, (iii) As pointed out by Cunningham[7], the TAR definition from the ICRU Report 23[5] is meaningless when applied to field sizes smaller than the diameter of the small mass of tissue. For such small field sizes, the scatter dose from the small mass of tissue is comparable to that from the phantom, (iv) The ICRU Report 23 definitions of the TAR and the PSF were conceptually different although it was assumed that the TAR at $z = z_{\max}$ is numerically equal

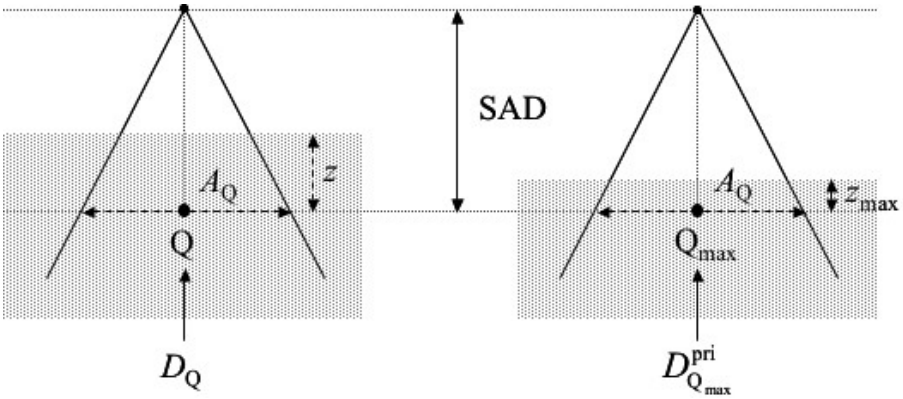

Figure 2–4: Schematic definition of the TAR according to the BJR Supplement 17[6]. The TAR at point Q was defined as the ratio of the total absorbed dose at point Q to the primary dose at point Q_{max}.

to the PSF. The TAR definition was based on the "small mass of tissue in air" concept, while the PSF definition was based on the "primary dose in the phantom" concept. Henry[8] and Pfalzner[9] pointed out that when applying the ICRU Report 23 definitions of the TAR and the PSF, the numerical values of the TAR at z_{max} and the PSF in high energy photon beams might be different from one another.

To overcome the defects in the ICRU Report 23 definition of the TAR and to blend harmoniously the definitions of the TAR and the PSF, the BJR Supplement 17[6] modified the definition of the TAR and defined it as the ratio of the total absorbed dose at depth z to the absorbed dose from primary photons at depth z_{max} at the same distance from the radiation source. As shown schematically in Fig. 2–4, the TAR at point Q was given as:

$$\mathrm{TAR}(z, A_Q, h\nu) = \frac{D_Q}{D^{\mathrm{pri}}_{Q_{max}}}, \tag{2.4}$$

where D_{Q} is the total absorbed dose at point Q for depth z and field size A_{Q} in the phantom and $D^{\mathrm{pri}}_{\mathrm{Q}_{\mathrm{max}}}$ is the absorbed dose from primary photons at point $\mathrm{Q}_{\mathrm{max}}$ for depth z_{max} and field size A_{Q} also in the phantom. The two points Q and $\mathrm{Q}_{\mathrm{max}}$ are at the same distance from the source.

The BJR Supplement 17[6] did not change the definition of the SF that was given by the ICRU Report 23[5], but linked the SF and the TAR at point Q with the following relationship:

$$\mathrm{SF}(z, A_{\mathrm{Q}}, h\nu) = \mathrm{TAR}(z, A_{\mathrm{Q}}, h\nu) \times e^{\mu(z - z_{\mathrm{max}})}, \tag{2.5}$$

where μ is the linear attenuation coefficient of the photon beam in the phantom. Based on Eq. 2.5, the PSF, defined as the SF at $z = z_{\mathrm{max}}$, is equal to the TAR at z_{max}.

The BJR Supplement 17[6] noted that determining the primary dose component $D^{\mathrm{pri}}_{\mathrm{Q}_{\mathrm{max}}}$ was not an easy task in high energy photon beams. Carrying out measurements of the primary dose component at z_{max} using in-air measurements with an ionization chamber surrounded by a build-up cap results in overestimation of the primary dose. In addition to the primary photons, the measured ionization signal in the ionization chamber includes contribution from photons scattered within the build-up cap. Henry[8] estimated that a 0.5 cm build-up cap contributes to 1 % of the total measured signal in the ionization chamber for a ^{60}Co beam. For higher energy photon beams, larger build-up caps are required, and the contribution from the build-up cap scattered photons to the measured signal can be as high as 10 %.

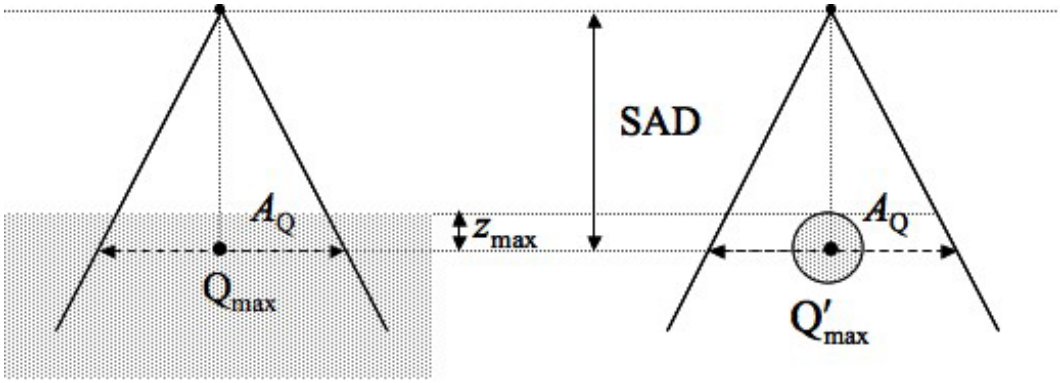

Figure 2–5: Schematic definition of the empirical PSF from the BJR Supplement 17[6]. The empirical PSF for field size A_Q was defined as the ratio of the the total absorbed dose at point Q_{max} in the phantom to the absorbed dose at point Q'_{max} in the small mass of build-up material.

For practical purposes, the BJR Supplement 17[6] suggested measuring an *empirical PSF*, defined as the total absorbed dose at z_{max} in the phantom to the absorbed dose in a small mass of build-up material in air, and using the *normalized peak scatter factor* NPSF in dosimetric calculations. The empirical PSF is related to the PSF through the following relationship:

$$\text{Empirical PSF}(A_Q, h\nu) = \frac{\text{PSF}(A_Q, h\nu)}{1+B}, \tag{2.6}$$

where B is the dose contribution at Q'_{max} from photons scattered within the small mass of build-up cap material relative to the dose from primary photons. The parameter B depends on the size and the shape of the build-up cap, but has a negligible dependance on the field size. The BJR Supplement 17[6] argued that the ratios of PSFs are numerically equal to the ratios of the corresponding empirical PSFs.

Therefore, the NPSF for field size A_Q were given with the following relationships:

$$\text{NPSF}(A_Q, h\nu) = \frac{\text{PSF}(A_Q, h\nu)}{\text{PSF}(A_{Q_{ref}}, h\nu)} = \frac{\text{Empirical PSF}(A_Q, h\nu)}{\text{Empirical PSF}(A_{Q_{ref}}, h\nu)}, \tag{2.7}$$

where $A_{Q_{ref}}$ is the reference field size (usually 10×10 cm^2).

The BJR Supplement 17[6] suggested that obtaining the "true" PSF can be carried out by the extrapolation of the NPSF to 0×0 cm^2 field size. The procedure involves the following steps: (i) measuring empirical PSF as a function of field size A_Q; (ii) calculating and plotting NPSF as a function of field size A_Q; (iii) extrapolating the NPSF curve to 0×0 cm^2 field size to obtain the NPSF(0, $h\nu$). Since the PSF(0, $h\nu$) is equal to unity, the NPSF(0, $h\nu$) is numerically equal to the reciprocal of the PSF($A_{Q_{ref}}, h\nu$). The PSF for any field size A_Q can be obtained with the following relationship:

$$\text{PSF}(A_Q, h\nu) = \text{NPSF}(A_Q, h\nu) \times \text{PSF}(A_{Q_{ref}}, h\nu). \tag{2.8}$$

2.6 British Journal of Radiology Supplement 25

The BJR Supplement 25[10], published in 1996, is a revised version of the BJR Supplement 17[6].

The definitions of the TAR, the SF, the BSF, and the PSF in the BJR Supplement 25[10] were not changed from their definitions in the BJR Supplement 17[6]. For ^{60}Co beam, however, the reference data of the TAR and the PSF were increased by 1.8 % from the data in the BJR Supplement 17[6]. Kijewski *et al.*[11] found that the scatter-primary ratios SPRs for a ^{60}Co beam calculated with Monte Carlo methods were different from the SPRs derived from ^{60}Co TAR data published in the BJR

Supplement 17[6]. McKenzie[12], Nizin and Kase[13], and Burns *et al.*[14] calculated directly the PSF for ^{60}Co beam using Monte Carlo methods and found that the calculated PSF was about 2 % higher than that tabulated in the BJR Supplement 17[6].

In the BJR Supplement 25[10], the term empirical PSF was replaced by the *apparent PSF*. The BJR Supplement 25[10], similarly to the BJR Supplement 17[6], suggested that the "true" PSF can be estimated by the extrapolation of the NPSF to 0×0 cm^2 field size. The document also provided an alternative extrapolation technique, suggested by Bjärngard and Petti[15], to obtain the PSF from measured TMR. Bjärngard and Petti[15] derived the following relationship:

$$\frac{\mathrm{SF}(z, A_\mathrm{Q}, h\nu)}{\mathrm{PSF}(A_{\mathrm{Q}_\mathrm{ref}}, h\nu)} = \mathrm{NPSF}(A_\mathrm{Q}, h\nu) \times \mathrm{TMR}(z, A_\mathrm{Q}, h\nu) \times e^{\mu(z - z_\mathrm{max})}, \qquad (2.9)$$

where μ is the linear attenuation coefficient in water. Since the SF for 0×0 cm^2 field size is equal to one, the extrapolation of the right hand side of Eq. 2.9 to 0×0 cm^2 field size gives the reciprocal of the PSF at the reference field size. Bjärngard and Petti[15] and Bjärngard *et al.*[16] showed that extrapolation of the right hand size of Eq. 2.9 can be carried out with a simple linear relationship for a constant ratio of A_Q/z. The BJR Supplement 25[10] calculated the PSF for 10×10 cm^2 field size in 6 MV photon beam using the extrapolation method suggested by Bjärngard and Petti[15] when A_Q/z was equal to one. The calculated value of the PSF for the 10×10 cm^2 field size in the 6 MV photon beam was 1.080.

2.7 Summary

The definitions of the PSF and the TAR have been refined since they were introduced in the early days as higher energy photon beams were introduced in radiotherapy. In some instances, the changes were required to provide physicists with practical means for measuring the two dosimetric quantities while maintaining the equality of the PSF and the TAR at the depth of maximum dose $z_{\max}$. In Table 2–1, the definitions of the TAR and the SF in a number of reference reports are presented chronologically.

	TAR	SF
ICRU Report 10d [2](1963)	the ratio of the absorbed dose at a given point in the phantom to the absorbed dose in a small mass of tissue in air at the same distance from the source	the ratio of the exposure at a reference point in the phantom to the exposure at the same distance in air under similar conditions of irradiation in the absence of the phantom
BJR Supplement 11 [4](1972)	same as the ICRU Report 10d	the ratio of the exposure (or of *the absorbed dose*) at a reference point in a phantom to the part of that exposure (or *absorbed dose*) *which is due to primary photons*
ICRU Report 23 [5](1973)	same as the ICRU Report 10d	the ratio of the exposure (or of the absorbed dose) at *any point* in a phantom to the part of that exposure (or absorbed dose) which is due to primary photons
BJR Supplement 17 [6](1983)	the ratio of the total absorbed dose at depth z to the absorbed dose *from primary photons at depth* $z_{\max}$ at the same distance from the radiation source	same as the ICRU Report 23
BJR Supplement 25 [10](1996)	same as the BJR Supplement 17	same as the ICRU Report 23

Table 2–1: Chronological summary of the definitions of the TAR and the SF from the ICRU Report 10d[2], the BJR Supplement 11[4], the ICRU Report 23[5], the BJR Supplement 17[6], and the BJR Supplement 25[10].

REFERENCES

[1] H.E. Johns, G.F. Whitmore, J.A. Whitson, and F. H. Umberg. A system of dosimetry for rotation therapy with typical rotation distributions. *Journal of the Canadian Association of Radiologists*, 4:1–14, 1953.

[2] International Commission on Radiation Units and Measurements (ICRU). *Clinical dosimetry,* Report 10d. National Bureau of Standards, Washington, DC, 1962.

[3] J. R. Cunningham, H. E. Johns, and S. K. Gupta. An examination of the definition and magnitude of backscatter factor for cobalt 60 gamma rays. *British Journal of Radiology*, 14:265–268, 1965.

[4] British Journal of Radiology. *Central axis depth dose data for use in radiotherapy,* Supplement 11. British Institute of Radiology, London, UK, 1972.

[5] International Commission on Radiation Units and Measurements (ICRU). *Measurement of absorbed dose in a phantom irradiated by a single beam of X or gamma rays,* Report 23. International Commission on Radiation Units and Measurements, Washington, DC, 1973.

[6] British Journal of Radiology. *Central axis depth dose data for use in radiotherapy,* Supplement 17. The British Institute of Radiology, London, UK, 1983.

[7] J. R Cunningham. Scatter-air ratios. *Physics in Medicine and Biology*, 17:42–51, 1972.

[8] W. H. Henry. Tissue-air ratio, peak scatter factor and consistency. *Physics in Medicine and Biology*, 19:43–50, 1974.

[9] P. F. Pfalzner. A revised equation relating tissue-air ratio to percent depth dose. *Physics in Medicine and Biology*, 26:510–513, 1981.

[10] British Journal of Radiology. *Central axis depth dose data for use in radiotherapy: 1996,* Supplement 25. The British Institute of Radiology, London, UK, 1996.

[11] P. K. Kijewski, B. E. Bjärngard, and P. L. Petti. Monte Carlo calculations of scatter dose for small field sizes in a ^{60}Co beam. *Medical Physics*, 13:74–77, 1986.

[12] A. L. McKenzie. Should ^{60}Co tissue-air ratios be re-evaluated? *Physics in Medicine and Biology*, 37:1601–1610, 1992.

[13] P. S. Nizin and K. R. Kase. Determination of primary dose in ^{60}Co gamma beam using a small attenuator. *Medical Physics*, 17:92–94, 1990.

[14] J. E. Burns, D. H. Pritchard, and R. T. Knight. Peak scatter factors for ^{60}Co gamma-radiation. *Physics in Medicine and Biology*, 37:2309–2318, 1992.

[15] B. E. Bjärngard and P. L. Petti. Description of the scatter component in photon beam data. *Physics in Medicine and Biology*, 33:21–32, 1988.

[16] B. E. Bjärngard, H. Rashid, and C. H. Obcemea. Separation of primary and scatter componenents of measured photon beam data. *Physics in Medicine and Biology*, 34:1939–1945, 1989.

CHAPTER 3
Materials and Methods

3.1 Experimental apparatus

3.1.1 Ionization chambers and electrometers

The measurements reported in this thesis were carried out using two ionization chambers: an Exradin Miniature Shonka Thimble Chamber model A1SL (Standard Imaging, Madison, WI) and a PTW Farmer-type ionization chamber model 30004 (PTW, Freiburg, Germany).

The Exradin A1SL ionization chamber, shown in Fig. 3–1, is a cylindrical ionization chamber with a uniform outer diameter of 0.625 cm and a wall thickness of 0.1 cm. The diameter of the central collecting electrode is 0.1 cm and the electrode length is 0.44 cm. The radius and length of the air cavity in the ionization chamber are 0.2 cm and 0.57 cm, respectively, and the nominal collecting volume of the air cavity is 0.056 cm^3. Many of the important components of the ionization chamber, such as the wall, central collecting electrode, and guard ring, are made of C-552 air equivalent plastic[1], which has a physical density of 1.76 g/cm^3 and is composed of hydrogen (2.5 %), carbon (50.2 %), oxygen (0.4 %), fluorine (46.5 %), and silicon (0.4 %).

To verify the dimensions of the Exradin A1SL ionization chamber, its radiographic image was obtained using a Simulix EVOLUTION^{TM} simulator unit (Nucletron, Veenendaal, Netherlands). As shown in Fig. 3–2, only the outer dimensions of

Figure 3–1: The Exradin Miniature Shonka Thimble Chamber model A1SL.

the ionization chamber were visible in the x-ray image; the dimensions of the wall thickness, the central collecting electrode, and the guard ring were difficult to determine with the x-ray image. The Exradin A1SL ionization chamber was also scanned in an AcQSim CT simulator (Philips, Ontario, CA). CT slices with 1 mm thickness were obtained and a 3-dimensional rendered image of the ionization chamber was reconstructed using OsiriX imaging software (version 3.2.1, OsiriX Foundation, Geneva, Switzerland). Figure 3–3 shows the 3-dimensional reconstructed CT image of the ionization chamber with its wall thickness, collecting electrode, and guard ring clearly visible. The dimensions measured from the radiographic image and the CT rendered image were within 1 % of the dimensions specified by the manufacturer.

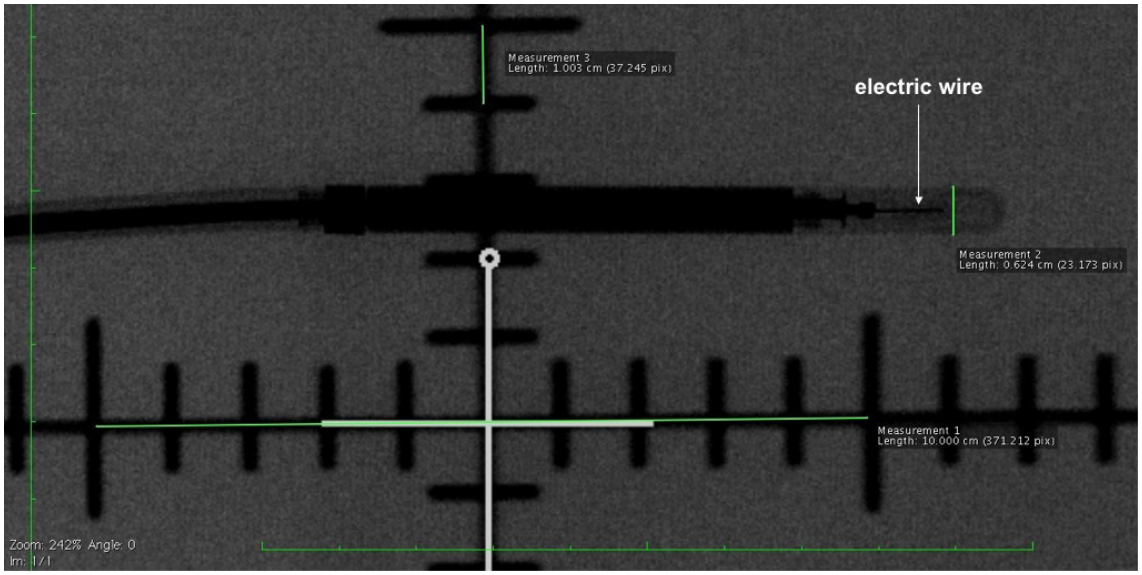

Figure 3–2: X-ray image of the Exradin A1SL ionization chamber.

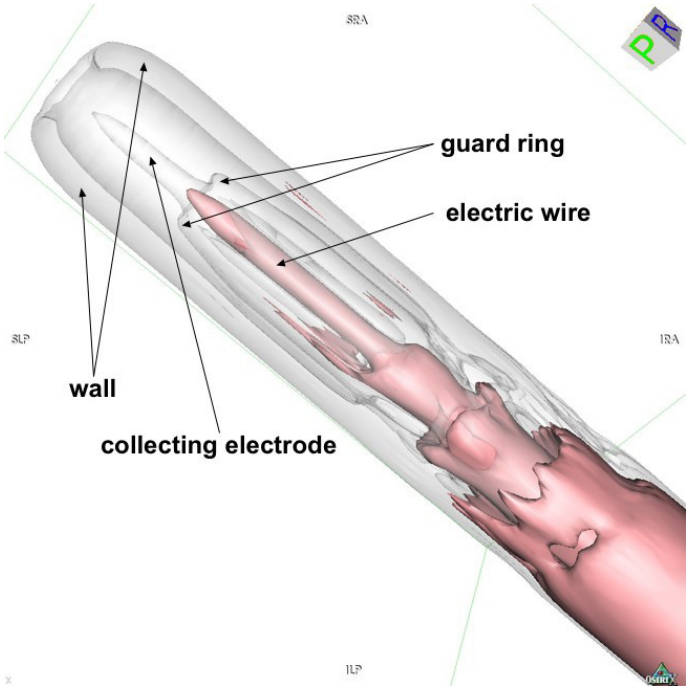

Figure 3–3: 3-dimensional rendered image of the Exradin A1SL ionization chamber.

Figure 3–4: The PTW 30004 Farmer ionization chamber.

The second ionization chamber used in our work was the PTW Farmer-type ionization chamber model 30004 (PTW, Freiburg, Germany). The PTW 30004 ionization chamber is a cylindrical ionization chamber, as shown in Fig. 3–4, with an outer diameter of 0.7 cm and a wall thickness of 0.046 cm. The radius and length of the air cavity are 0.31 cm and 2.30 cm, respectively, and the nominal collecting volume of the air cavity is 0.6 cm^3. The wall of the PTW 30004 ionization chamber is made of graphite (density: 1.7 g/cm^3), and its collecting electrode is made of aluminum (density: 2.7 g/cm^3).

The ionization chambers were connected to a Keithley electrometer model 35617 (Keithley, Cleveland, OH) using a triaxial cable. The electrometer was used to bias the ionization chamber as well as to read the ionization signal produced in the air cavity. In all measurements, the ionization chamber was biased with a +300 V and no ionization recombination or polarity corrections were applied.

3.1.2 Radiation beams

The radiation beams used in our work were 6 MV and 18 MV photon beams produced from a Clinac 21 EX unit (Varian, Palo Alto, CA) at the Montreal General Hospital. To investigate the characteristics of both photon beams, attenuation curves were measured in copper (density: 8.96 g/cm^2) and lead (density: 11.34 g/cm^2) using narrow beam geometry. The attenuation curve measurements were carried out using the PTW 30004 ionization chamber surrounded with an appropriate aluminum build-up cap. The thicknesses of the build-up caps were 1.5 g/cm^2 for measurements in the 6 MV photon beam and 3.0 g/cm^2 for measurements in the 18 MV photon beam. The ionization chamber with the build-up cap was positioned at a distance of 156 cm from the radiation source. In all attenuation measurements, the field size was set to 3×3 cm^2 at 100 cm, thus, projecting a field size of 4.7×4.7 cm^2 at the ionization chamber plane. Copper and lead attenuators made of 1 mm thick sheets were placed on a Lucite^{TM} tray at a distance of 70 cm from the radiation source. The Lucite^{TM} tray was mounted in the tray insert on the linac head. Transmission measurements were obtained in copper for thicknesses up to 5 cm and in lead for thicknesses up to 3 cm.

The transmissions as a function of the attenuator thickness in copper and lead for the 6 MV and 18 MV photon beams are plotted in Fig. 3–5. For the 6 MV photon beam, the HVLs measured in copper and lead are 1.84 cm and 1.11 cm, respectively, and the HVLs for the 18 MV photon beam measured in copper and lead are 2.38 cm and 1.25 cm, respectively. The linear attenuation coefficient and the beam hardening coefficient for the 6 MV and 18 MV photon beams in copper and

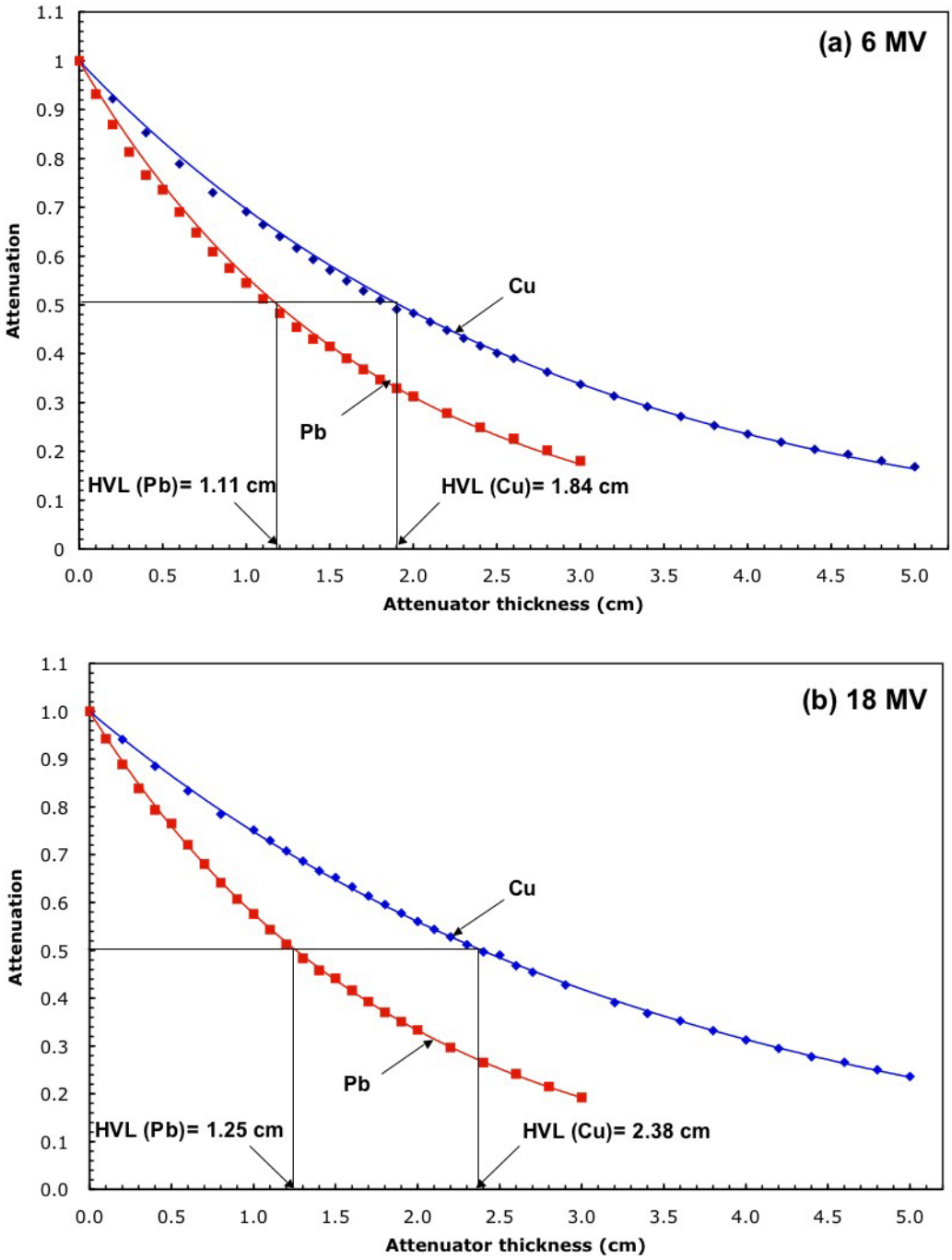

Figure 3–5: Attenuation curves for (a) 6 MV photon beam and (b) 18 MV photon beam in copper and lead.

Energy	Material	μ (cm^{-1})	η (cm^{-1})	μ/ρ (cm^2/g)	HVL (cm)
6 MV	Copper	0.377	1.107×10^{-2}	0.0420	1.84
	Lead	0.627	3.253×10^{-2}	0.0552	1.11
18 MV	Copper	0.291	9.158×10^{-4}	0.0325	2.38
	Lead	0.556	4.562×10^{-3}	0.0490	1.25

Table 3–1: The linear attenuation coefficients μ, beam hardening coefficients η, mass attenuation coefficients μ/ρ, and HVLs in copper and lead for the 6 MV and 18 MV photon beams produced in our Varian Clinac 21 EX linac.

lead were obtained by fitting the transmission data in Fig. 3–5 to Eq. 1.5. Table 3–1 summarizes the linear attenuation coefficient μ, the beam hardening coefficient η, the mass attenuation coefficient μ/ρ, and the HVL for the 6 MV and 18 MV photon beams in copper and lead.

3.1.3 Solid Water™ phantom

Solid Water™ is a plastic material with a density of approximately 1.036 g/cm^3. It is composed of hydrogen (8 %), carbon (67 %), nitrogen (2.5 %), oxygen (20 %), and calcium (2.5 %). In-phantom measurements were carried out using a 30(length)$\times$ 30(depth) $\times$ 10(height) cm^3 Solid Water™ phantom shown in Fig. 3–6. The Solid Water™ phantom had 1.9 cm diameter holes at 1.5 cm and 3.0 cm depths. The length of both holes allowed for positioning of the ionization chamber at the vertical midline of the phantom. To fit the Exradin A1SL ionization chamber into the holes, a custom-made Solid Water™ sleeve with a 1.9 cm outer diameter was built in the machine shop of the Medical Physics department. The inner diameter of the sleeve was 0.625 cm, just large enough to fit the Exradin A1SL ionization chamber. These two holes located at 1.5 cm and 3.0 cm depths were used to position the Exradin

Figure 3–6: $30 \times 30 \times 10$ cm^3 Solid Water^{TM} phantom.

A1SL ionization chamber with the Solid Water^{TM} sleeve at z_{max} in the phantom for measurements in the 6 MV and 18 MV photon beams.

3.1.4 Build-up caps

Dosimetric quantities of interest in air are in general measured using a water-equivalent material build-up cap surrounding the ionization chamber. The build-up caps are required to establish electronic equilibrium in the ionization chamber. For high energy photon beams, the thickness of the build-up cap required to establish electronic equilibrium is of the order of a few centimeters when constructed from a water-equivalent material. The large dimensions of a water-equivalent build-up cap might in general perturb the in-air measurement because of the increase in the number of scattered photons produced within the build-up cap. The scattered photon contribution to the measured signal can be relatively large when compared to the

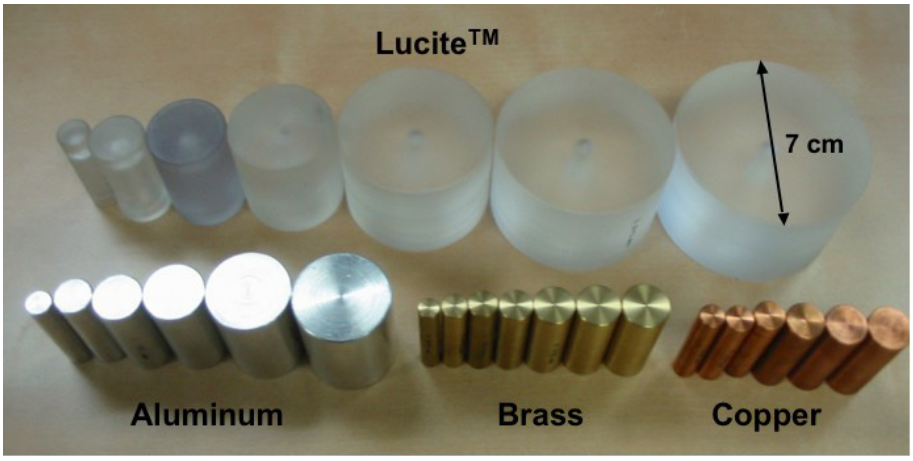

Figure 3–7: Build-up caps made by Lucite™, aluminum, brass, and copper.

signal produced from primary photons especially when the in-air measurements are carried out in small field sizes. Therefore, in-air measurements in high energy photon beams are sometimes carried out with build-up caps constructed from high density materials, such as copper, to allow in-air measurements in small field sizes. For example, for a 3.0 g/cm^2 equivalent thickness, the radius of a Lucite™ build-up cap is 2.69 cm, while the radius of a copper build-up cap is only 0.63 cm.

For our in-air measurements, custom-made build-up caps made of Lucite™ (Polymethyl Methacrylate, PMMA), aluminum, brass, and copper were used. The build-up caps were made in our machine shop and are shown in Fig. 3–7. Lucite™ is a plastic material composed of hydrogen (8 %), carbon (60 %), and oxygen (32 %) with a physical density of 1.19 g/cm^3.[1] Brass is an alloy composed of copper (66.6 %) and zinc (33.4 %) and has a physical density of 8.4 g/cm^3. The physical densities of aluminum and copper are 2.7 g/cm^3 and 8.96 g/cm^3, respectively. The build-up caps for each material ranged in thickness from 0.5 g/cm^2 to 4.0 g/cm^2.

All build-up caps had a 0.63 cm diameter hole that allows fitting the Exradin A1SL chamber into the build-up cap. After constructing the build-up caps, the thickness of individual build-up cap was determined using a vernier caliper.

3.2 Experimental techniques

3.2.1 In-phantom measurements

In-phantom measurements were carried out using the $30 \times 30 \times 10$ cm^3 Solid Water^{TM} phantom. The Exradin A1SL ionization chamber with the Solid Water^{TM} sleeve was inserted into the hole at 1.5 cm depth for measurements in the 6 MV photon beam and into the hole at 3.0 cm depth for the 18 MV photon beam. During our experiments, the hole not filled with the ionization chamber was filled with a Solid Water^{TM} plug to avoid any possible interference of the empty hole with our measurements.

The in-phantom measurements were carried out with a source-axis distance SAD of 100 cm. Therefore, the collimator settings for the upper and lower jaws defined the field size at the ionization chamber plane. The Solid Water^{TM} phantom was placed on the treatment couch of the linac and the gantry angle was set to 0°. Fig. 3–8 shows the setup for the in-phantom measurements.

To position correctly the ionization chamber along the beam central axis, the signal of the ionization chamber was measured in a 1×1 cm^2 field size as a function of the phantom's longitudinal and lateral positions across the plane perpendicular to the radiation beam. The phantom position with respect to the radiation beam was varied by controlling the supporting couch of the linac. The procedure of positioning the ionization chamber along the beam central axis started by first aligning the

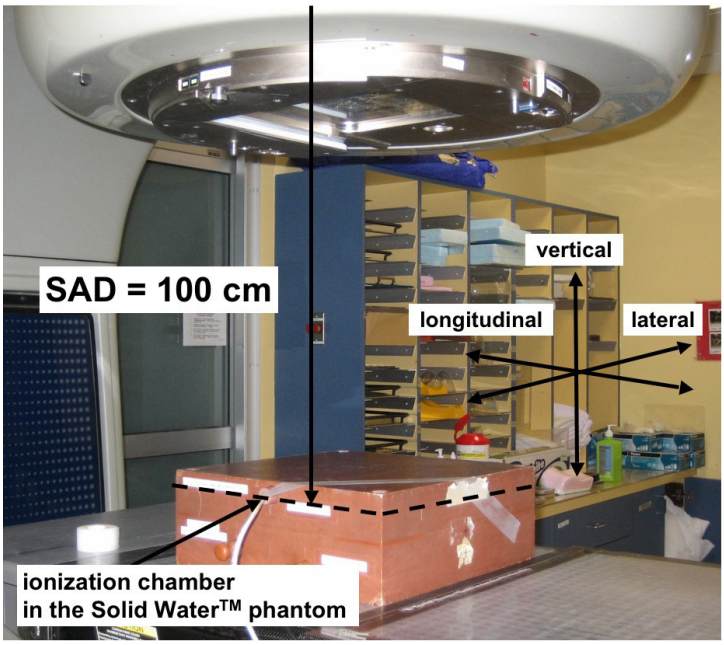

Figure 3–8: In-phantom measurement setup. The distance from the radiation source to the ionization chamber plane is 100 cm.

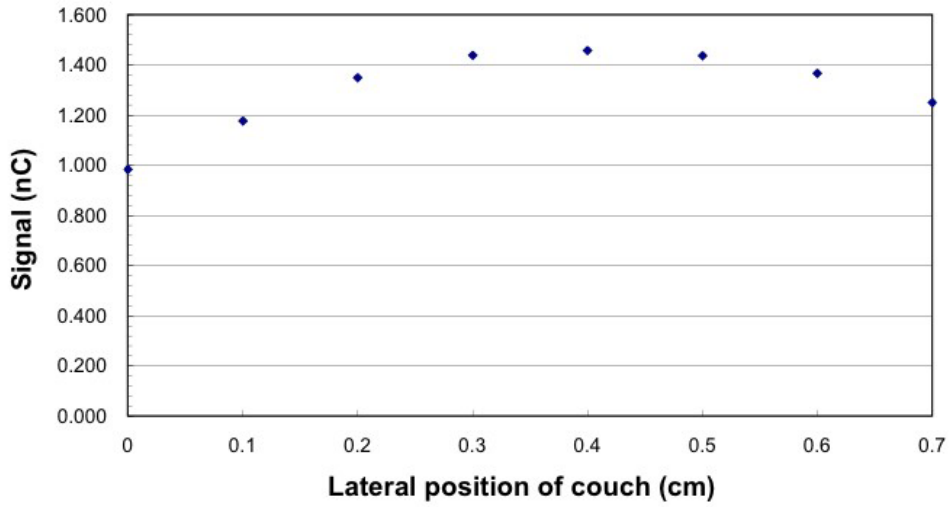

Figure 3–9: Ionization signal versus lateral couch position for a 1×1 cm^2 field size.

ionization chamber using the light field for a 10×10 cm^2 field size and the linac cross-hairs. Then, the collimators were set to 1×1 cm^2 field size and the ionization signal as a function of the lateral couch position was measured. A typical plot of the ionization signal versus the lateral couch position is shown in Fig. 3–9. The lateral couch position was then locked at the position where the ionization signal was maximum and the ionization signal was then measured as a function of the longitudinal couch position. The longitudinal couch position was then locked at the position where the measured signal was maximum.

3.2.2 In-air measurements

In-air measurements were carried out using the custom-made build-up caps. Figure 3–10 shows the setup for the in-air measurements. In our in-air measurements, a lateral beam was used by rotating the gantry to 90°. The Exradin A1SL ionization chamber was fixed to a supporting device and the ionization chamber with the build-up cap was aligned vertically at an SAD of 100 cm. This orientation of setting the ionization chamber was chosen to prevent damaging the ionization chamber because of the weight of the heavy build-up caps. Similarly to the in-phantom measurements, the signal of the ionization chamber was measured as a function of the vertical and longitudinal positions across a 1×1 cm^2 field size in order to align the ionization chamber along the beam central axis before starting the in-air measurements.

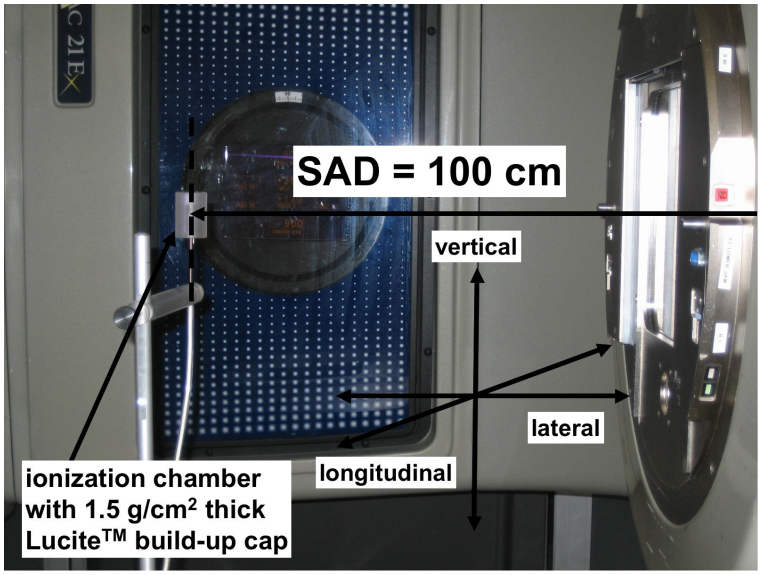

Figure 3–10: In-air measurement setup. The distance from the radiation source to the ionization chamber plane is 100 cm.

3.3 Monte Carlo simulations

3.3.1 EGSnrc code system

The Monte Carlo code system used in our work was the EGS (Electron-Gamma-Shower)nrc code system[2] released by the National Research Council of Canada. The EGSnrc code system simulates the transport of photons and electrons in a user defined geometry using the interaction probabilities of photons and electrons in matter.

The EGSnrc code system is divided into a USER code and an EGS code. The USER code contains subroutines to define: (i) the geometry in which the particles are transported and (ii) the scored quantities of interest, i.e., dose or kerma. The

EGS code consists of subroutines that govern the particle transport in the simulation. Details on the EGSnrc code system can be obtained at the following website: *http://www.irs.inms.nrc.ca/EGSnrc/pirs701/index.html*

The execution of a Monte Carlo simulation with the EGSnrc code system, in addition to the USER code, requires an input file and a cross section data file. The input file contains the size and material components of the geometry of interest, the source location, energy and type, Monte Carlo transport options (cut-off energies and physics options), number of histories to simulate, random number seeds, and the desired output quantities and format. The cross section data file is compiled by the user and contains photon cross section data and electron stopping power data for materials used in the predefined geometry. These data are generated by a separate program called PEGS4 including in the EGSnrc code system.

3.3.2 BEAMnrc

The BEAMnrc system[3], part of the EGSnrc code system package, is used to simulate the transport of photons and electrons in a treatment head or an x-ray tube. The BEAMnrc system generates a USER code that models the complex geometry of a linac head using simpler geometry modules, called component modules (CMs), stacked above one another. In the input file, the user defines: (i) the dimensions and materials of the CMs; (ii) source type and energy; (iii) transport options; and (iv) output options, etc. One of the most important outputs of a BEAMnrc user code simulation is a phase-space file.

The phase-space file contains the characteristics of all particles crossing a scoring plane defined by the user. For each particle, the phase-space file records the particle's

charge, energy, position on the phase-space plane, velocity vector, and statistical weight. To statistically represent the particle fluence emerging from a linac head, a phase-space file containing a few million particles is typically scored below the CM representing the linac's exit window. The phase-space file may be used as an input source in other USER codes in the EGSnrc Monte Carlo code system.

In this work, the geometries of the Varian Clinac 21 EX linac (6 MV and 18 MV modalities) head were modeled using the BEAMnrc user code. The geometries of the Varian Clinac 21 EX linac head as modeled with BEAMnrc for the 6 MV and 18 MV modalities are illustrated in Fig. 3–11. For the simulation of the 6 MV photon beam, the energy of the electrons impinging on the x-ray target was 6 MeV and the radius of the electron pencil beam was 0.12 cm. For the 18 MV photon beam, the energy and radius of the electron pencil beam hitting the x-ray target were 18 MeV and 0.06 cm, respectively. The energy and radius of the electron beam in the BEAMnrc user code simulation are optimized by comparing the measured and calculated PDDs in water and the measured and calculated off-axis ratios at a given depth in water. The collimator settings produced a 10×10 cm^2 field size at 100 cm from the source position. Phase-space files for the 10×10 cm^2 field size were scored at 90 cm from the source position. The phase-space file for the 6 MV photon beam contained about 9.4×10^6 photons and 2.1×10^4 charged particles (electrons and positrons). The phase-space file for the 18 MV photon beam contained about 3.8×10^7 photons and 5.9×10^4 charged particles (electrons and positrons).

Photon spectral distributions representing the 6 MV and 18 MV were extracted from the scored phase-space files using the BEAMDP program[4], included in the

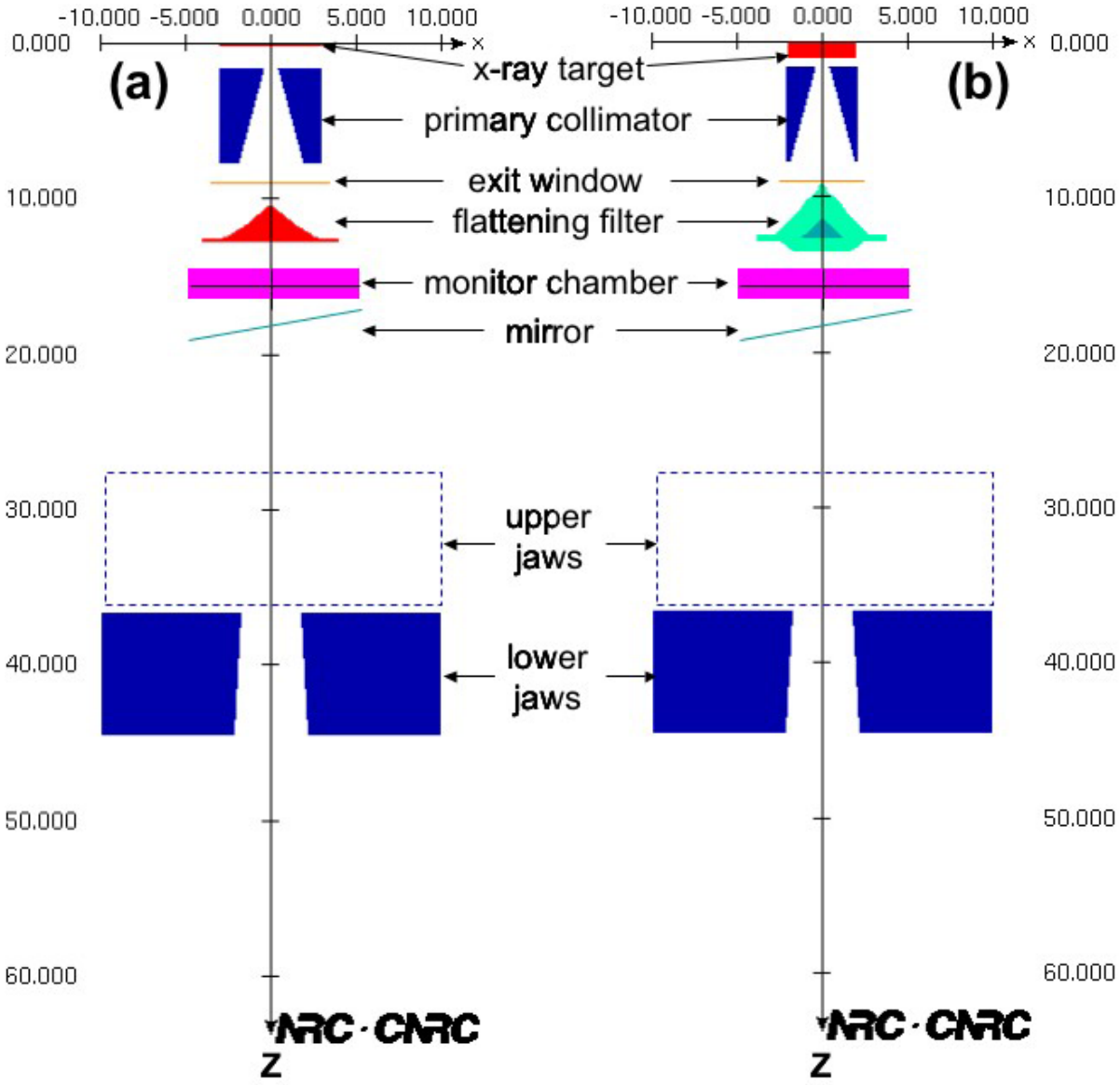

Figure 3–11: Geometries of the Varian Clinac 21 EX linac head for (a) 6 MV and (b) 18 MV photon beams. The phase-space files were scored at $z = 90$ cm.

EGSnrc code system package. The spectra for the 6 MV and 18 MV photon beams are shown in Fig. 3–12. The minimum and maximum kinetic energy of the photons for the 6 MV photon beam were 0 MeV and and 6 MeV, respectively. For the 18 MV photon beam, the minimum and maximum kinetic energies of the photons were 0 MeV and 18 MeV, respectively.

3.3.3 NRC user codes

In the EGSnrc code system package, standard user codes, called the NRC user codes[5], are released by the National Research Council of Canada. In this work, Monte Carlo simulations using the EGSnrc code system were carried out with three NRC user codes: the DOSRZnrc/EGSnrcMP user code, the SPRRZnrc/EGSnrcMP user code, and the g/EGSnrcMP user code.

DOSRZnrc/EGSnrcMP user code

The DOSRZnrc/EGSnrcMP user code[5] (DOSRZnrc) is used to calculate the absorbed dose in user-defined cylindrical geometry. The cylindrical geometry consists of annular scoring regions each defined with the inner and other radii and height. One of the output options available with the DOSRZnrc simulation is called "scatter fraction". When the "scatter fraction" option is selected, the simulation scores the scatter dose component in the region, in addition to scoring the total dose. The scatter dose component is the dose deposited in the region by photons that were scattered within the defined geometry. Hence, the primary dose component in the region can be obtained by subtracting the scatter dose component from the total dose. In our DOSRZnrc simulations, the photon spectral distribution files and the phase space files were used as particle source.

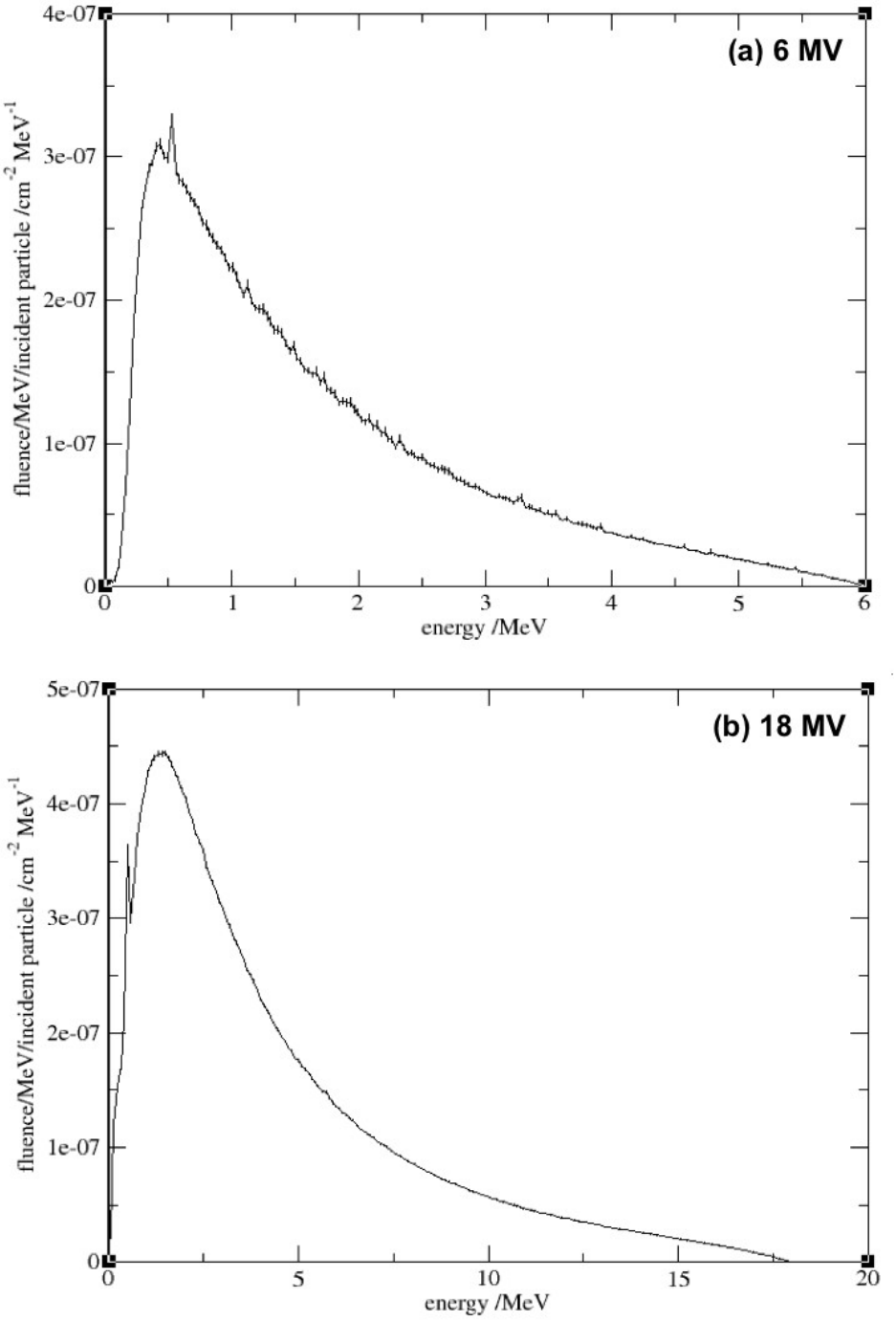

Figure 3–12: Photon spectra of Varian Clinac 21 EX (a) 6 MV photon beam and (b) 18 MV photon beam.

SPRRZnrc/EGSnrcMP user code

The SPRRZnrc/EGSnrcMP user code[5] (SPRRZnrc) is used to calculate the restricted mass collision stopping power ratios of two mediums. The outputs of the SPRRZnrc simulation are the ratios of the restricted mass collision stopping powers of a given medium in a region to a second user-defined medium. In our SPRRZnrc simulations, the phase space files were used to calculate restricted mass stopping powers relative to air.

g/EGSnrcMP user code

The g/EGSnrcMP user code[6] is used to calculate the radiation fraction $\overline{g}$ in a material for photons. In the input file of the g/EGSnrcMP simulations, the user defines: (i) the material of interest; (ii) parameters of the photon beam; and (iii) Monte Carlo transport parameters.

The outputs of the g/EGSnrcMP simulations are: (i) the mass energy transfer coefficient $\frac{\mu_{tr}}{\rho}$; (ii) mass energy absorption coefficient $\frac{\mu_{ab}}{\rho}$; and (iii) radiation fraction $\overline{g}$ for the material of interest. The $\frac{\mu_{tr}}{\rho}$, $\frac{\mu_{ab}}{\rho}$, and $\overline{g}$ are related by the following relationship:

$$\frac{\mu_{ab}}{\rho} = \frac{\mu_{tr}}{\rho}(1 - \overline{g}). \tag{3.1}$$

In the g/EGSnrcMP simulations, the particle source can be defined to emit monoenergetic photons or polyenergetic photons with energies sampled from a spectral distribution file. For a polyenergetic photon source, the g/EGSnrcMP user code reports the mean mass energy transfer coefficient $\frac{\overline{\mu}_{tr}}{\rho}$ and the mean mass energy

absorption coefficient $\frac{\overline{\mu}_{\text{ab}}}{\rho}$. In our g/EGSnrcMP simulations, the photon spectral distribution files were used to calculate $\frac{\overline{\mu}_{\text{ab}}}{\rho}$ for several materials of interest.

REFERENCES

[1] J. H. Hubbell and S. M. Seltzer. *Tables of x-ray mass attenuation coefficients and mass energy-absorption coefficients*, NISTIR 5632. National Institute of Standard and Technology, 2004. Available from *http://physics.nist.gov/PhysRefData/XrayMassCoef/tab2.html*.

[2] I. Kawrakow and D. W. O. Rogers. *The EGSnrc code system: Monte Carlo simulation of electron and photon transport,* NRCC Report PIRS-701. National Research Council Canada, Ottawa, ON, 2006.

[3] D. W. O. Rogers, B. Walters, and I. Kawrakow. *BEAMnrc users manual,* NRCC Report PIRS-0509(C)revK. National Research Council Canada, Ottawa, ON, 2006.

[4] C. -M. Ma and D. W. O. Rogers. *BEAMDP users manual,* NRCC Report PIRS-0509(C)revA. National Research Council Canada, Ottawa, ON, 2006.

[5] D. W. O. Rogers, I. Kawrakow, J. P. Seuntjens, B. R. B. Walters, and E. Mainegra-Hing. *NRC user codes for EGSnrc,* NRCC Report PIRS-702(revB). National Research Council Canada, Ottawa, ON, 2005.

[6] I. Kawrakow. *g/EGSnrcMP user code* (ver. 1.3). National Research Council Canada, Ottawa, ON, 2002.

CHAPTER 4
Results and Discussions

4.1 The apparent PSF for 6 MV and 18 MV photon beams

The BJR Supplement 25[1] defined the apparent peak scatter factor (apparent PSF) as the ratio of the total absorbed dose at $z_{\max}$ in the phantom to the absorbed dose in a small mass of build-up material in air. The apparent PSF versus field size was measured for the 6 MV and 18 MV photon beams using the setups for in-phantom measurements and in-air measurements described in section 3.2. For the in-phantom measurements, the Exradin A1SL ionization chamber was positioned in the Solid Water^{TM} phantom at 1.5 cm depth for measurements in the 6 MV photon beam and at 3.0 cm depth for measurements in the 18 MV photon beam. For the in-air measurements, build-up caps made of Lucite^{TM}, aluminum, brass, and copper were used. The thicknesses of the build-up caps were 1.324 g/cm^2 for the measurements in the 6 MV photon beam and 2.824 g/cm^2 for the measurements in the 18 MV photon beam. The combined thickness of the build-up cap and the ionization chamber's wall provided total build-up thicknesses of 1.5 g/cm^2 and 3.0 g/cm^2 for the measurements in the 6 MV and 18 MV photon beams, respectively. The field size at the ionization chamber plane for the in-phantom measurements and for the in-air measurements was varied from 1×1 cm^2 to 15×15 cm^2. The apparent PSF for a given field size was determined as the quotient of the measured air cavity ionization signal from the in-phantom measurement to that from the in-air measurement.

Figure 4–1 shows the measured apparent PSF versus field size for the 6 MV and 18 MV photon beams obtained using the Solid Water^{TM} phantom and the Lucite^{TM}, aluminum, brass, and copper build-up caps. For the 6 MV photon beam, the decrease of the apparent PSF with decreasing field size is relatively slow in the range from 15×15 cm^2 to 2×2 cm^2. For smaller field sizes, the apparent PSF decreases sharply with decreasing field size. The rapid decrease of the apparent PSF for fields smaller than 2×2 cm^2 might be attributed to the non-flatness of the beam profiles for small field sizes. The outer diameter of the Exradin A1SL ionization chamber is 0.625 cm, and the length of its air cavity is 0.57 cm. When the ionization chamber is placed in small field sizes, the air cavity volume is not exposed to a uniform beam intensity.

Similarly to the situation with the 6 MV photon beam, the apparent PSF for the 18 MV photon beam decreases slowly with decreasing the field size in the range from 15×15 cm^2 to 3×3 cm^2, and then decreases sharply with further field size decrease. For the 18 MV photon beam, we speculate that the relatively large shift in the depth of maximum dose $z_{\max}$ for small field size also contributes to the sharp decrease of the apparent PSF for fields smaller than 3×3 cm^2.

For the same build-up thickness, the volume of the build-up caps made of higher density materials, i.e., aluminum, brass, and copper, was much smaller than the build-up cap made of the relatively lower density material, Lucite^{TM}. For example, the thickness of the build-up caps made of aluminum, brass, and copper is 2.3, 7.1, and 7.5 times, respectively, smaller than that of the Lucite^{TM} build-up cap. It was expected that the scatter dose contribution produced within the build-up cap would decrease when using higher density materials because of the smaller volume

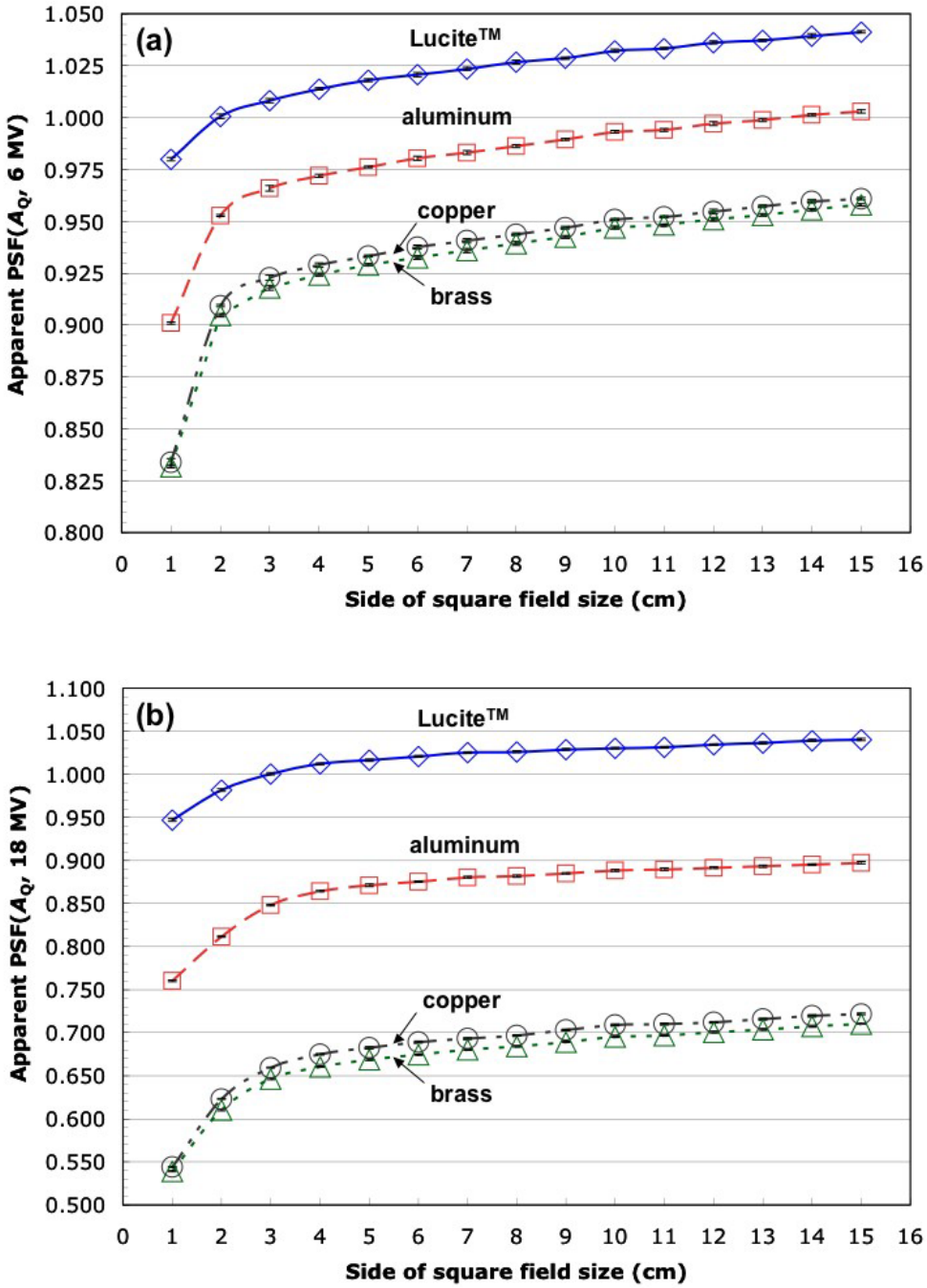

Figure 4–1: Apparent PSF for the 6 MV photon beam, in part (a), and for the 18 MV photon beam, in part (b), against field size measured using a Solid Water™ phantom and build-up caps made of Lucite™, aluminum, brass, and copper.

of the build-up cap, resulting in a larger measured apparent PSF. Contrary to our expectation, our measurements show that the apparent PSF at a given field size decreases as the density of the build-up cap material increases for the 6 MV and 18 MV photon beams.

4.2 The NPSF for 6 MV and 18 MV photon beams

Using the measured apparent PSF data, the normalized peak scatter factors (NPSFs) for the 6 MV and 18 MV photon beams were calculated using Eq. 2.7. The NPSF for field size A_{Q} is given by the following relationship:

$$\mathrm{NPSF}(A_{\mathrm{Q}}, h\nu) = \frac{\text{Apparent PSF}(A_{\mathrm{Q}}, h\nu)}{\text{Apparent PSF}(10, h\nu)}, \tag{4.1}$$

where the reference field size is 10×10 cm^2.

6 MV

The NPSF against field size obtained with the Lucite$^{\mathrm{TM}}$, aluminum, brass, and copper build-up caps for the 6 MV photon beam is shown in part (a) of Fig. 4–2 and summarized in Table 4–1. Table 4–1 also lists the NPSF for the 6 MV photon beam from the BJR Supplement 25[1]. The NPSFs for all four build-up cap materials are in agreement with the NPSF data from the BJR Supplement 25[1]. The standard deviation of the NPSF between the four build-up cap materials is within 0.3 % of the average value. We conclude that the dependence of the NPSF on the build-up cap material is relatively small and may be ignored for the 6 MV photon beam.

18 MV

Part (b) of Fig. 4–2 shows the NPSF versus field size obtained with Lucite$^{\mathrm{TM}}$, aluminum, brass, and copper build-up caps for the 18 MV photon beam. Table 4–2

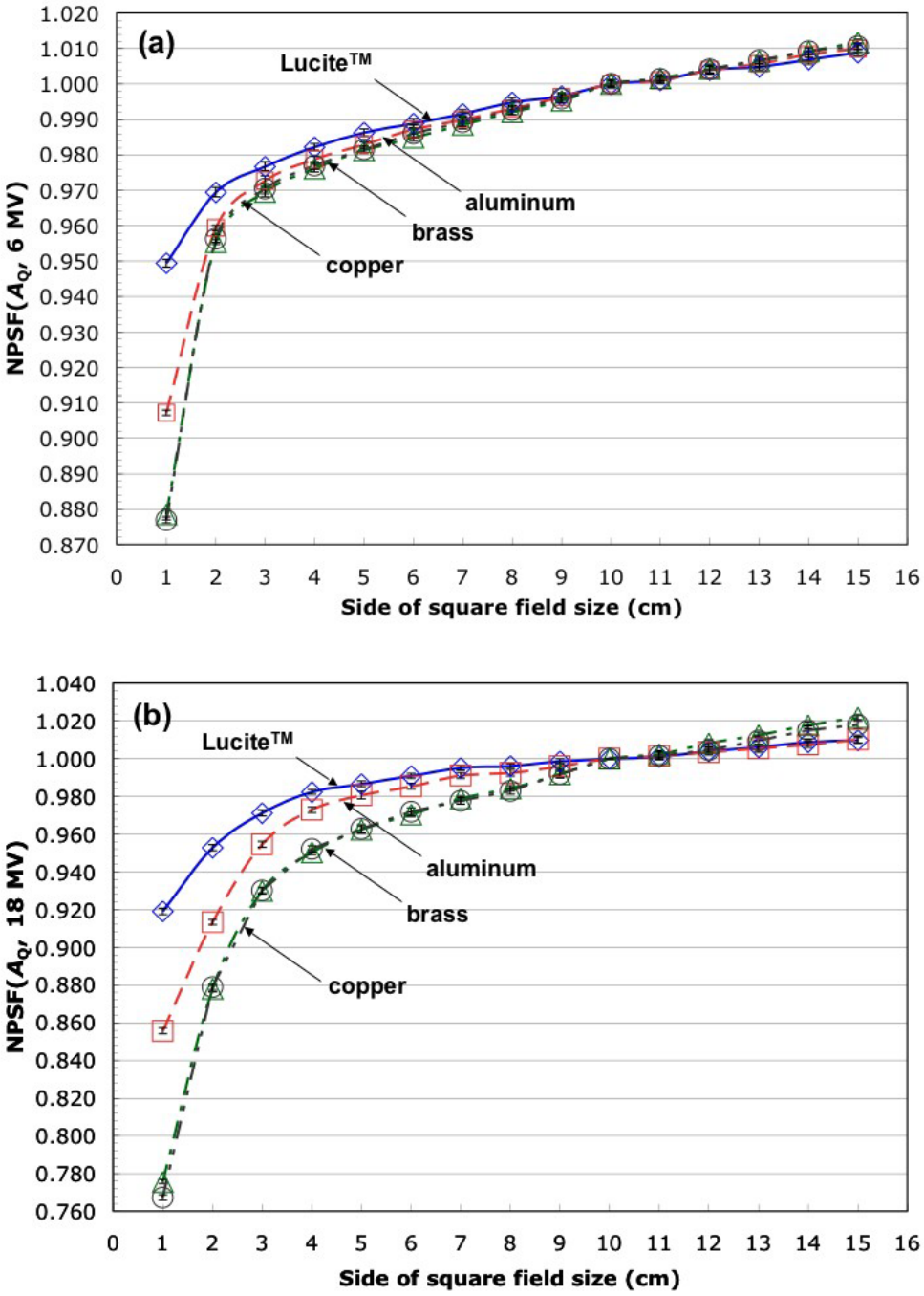

Figure 4–2: NPSF for the 6 MV photon beam, in part (a), and for the 18 MV photon beam, in part (b), versus field size obtained with Lucite™, aluminum, brass, and copper build-up caps.

build-up cap material	Field size (cm)								
	4	5	6	7	8	9	10	12	15
Lucite^{TM}	0.984	0.988	0.991	0.994	0.997	0.998	1.000	1.005	1.009
Aluminum	0.979	0.983	0.987	0.990	0.993	0.996	1.000	1.004	1.010
Brass	0.976	0.981	0.985	0.988	0.992	0.995	1.000	1.004	1.012
Copper	0.977	0.981	0.986	0.989	0.993	0.996	1.000	1.004	1.011
BJR 25	**0.979**	**0.983**	**0.987**	**0.990**	**0.994**	**0.997**	**1.000**	**1.006**	**1.013**

Table 4–1: NPSF obtained from measurements with Lucite^{TM}, aluminum, brass, and copper build-up caps and that referenced by the BJR Supplement 25[1] for the 6 MV photon beam.

build-up cap material	Field size (cm)								
	4	5	6	7	8	9	10	12	15
Lucite^{TM}	0.982	0.987	0.991	0.995	0.996	0.999	1.000	1.004	1.010
Aluminum	0.973	0.981	0.985	0.991	0.992	0.996	1.000	1.003	1.010
Brass	0.950	0.962	0.970	0.979	0.984	0.992	1.000	1.008	1.022
Copper	0.952	0.963	0.972	0.978	0.983	0.992	1.000	1.005	1.018
BJR 25	**0.979**	**0.983**	**0.987**	**0.990**	**0.994**	**0.997**	**1.000**	**1.006**	**1.013**

Table 4–2: NPSF obtained from measurements with Lucite^{TM}, aluminum, brass, and copper build-up caps and that referenced by the BJR Supplement 25[1] for the 18 MV photon beam.

summarizes the NPSF data shown in the part (b) of Fig. 4–2 and lists the NPSF for the 18 MV photon beam published in the BJR Supplement 25 [1]. The NPSFs for the 18 MV photon beam obtained with the Lucite^{TM} and aluminum build-up caps are in agreement with the NPSF published in the BJR Supplement 25[1]. However, there is a discrepancy between the NPSF measured with the brass and copper build-up caps and that published in the BJR Supplement 25[1]. For example, the NPSF measured with the brass and copper build-up caps for the 4×4 cm^2 field size is 3 % smaller than the NPSF for the same field size from the BJR Supplement 25[1]. Hence, we conclude that the NPSF for the 18 MV photon beam depends on the build-up cap material.

4.2.1 Extrapolated PSF(10, $h\nu$) for 6 MV and 18 MV photon beams

Following the recommendations of the BJR Supplements 17[2] and 25[1], the PSFs for the 10×10 cm^2 in the 6 MV and 18 MV photon beams were obtained by the extrapolation of the NPSF to 0×0 cm^2 field size. The NPSF curves for the 6 MV and 18 MV photon beams were extrapolated linearly to 0×0 cm^2 field size using the NPSF data for 3×3 cm^2 to 5×5 cm^2 field sizes. The PSF(10, $h\nu$) was then taken as the reciprocal of the NPSF for 0×0 cm^2 field size. The linear extrapolations of the NPSF to 0×0 cm^2 field size for the 6 MV and 18 MV photon beams are shown in Fig. 4–3. Table 4–3 lists the extrapolated PSF$(10, h\nu)$ for the 6 MV and 18 MV photon beams obtained from the measured NPSF data with the Lucite^{TM}, aluminum, brass, and copper build-up caps.

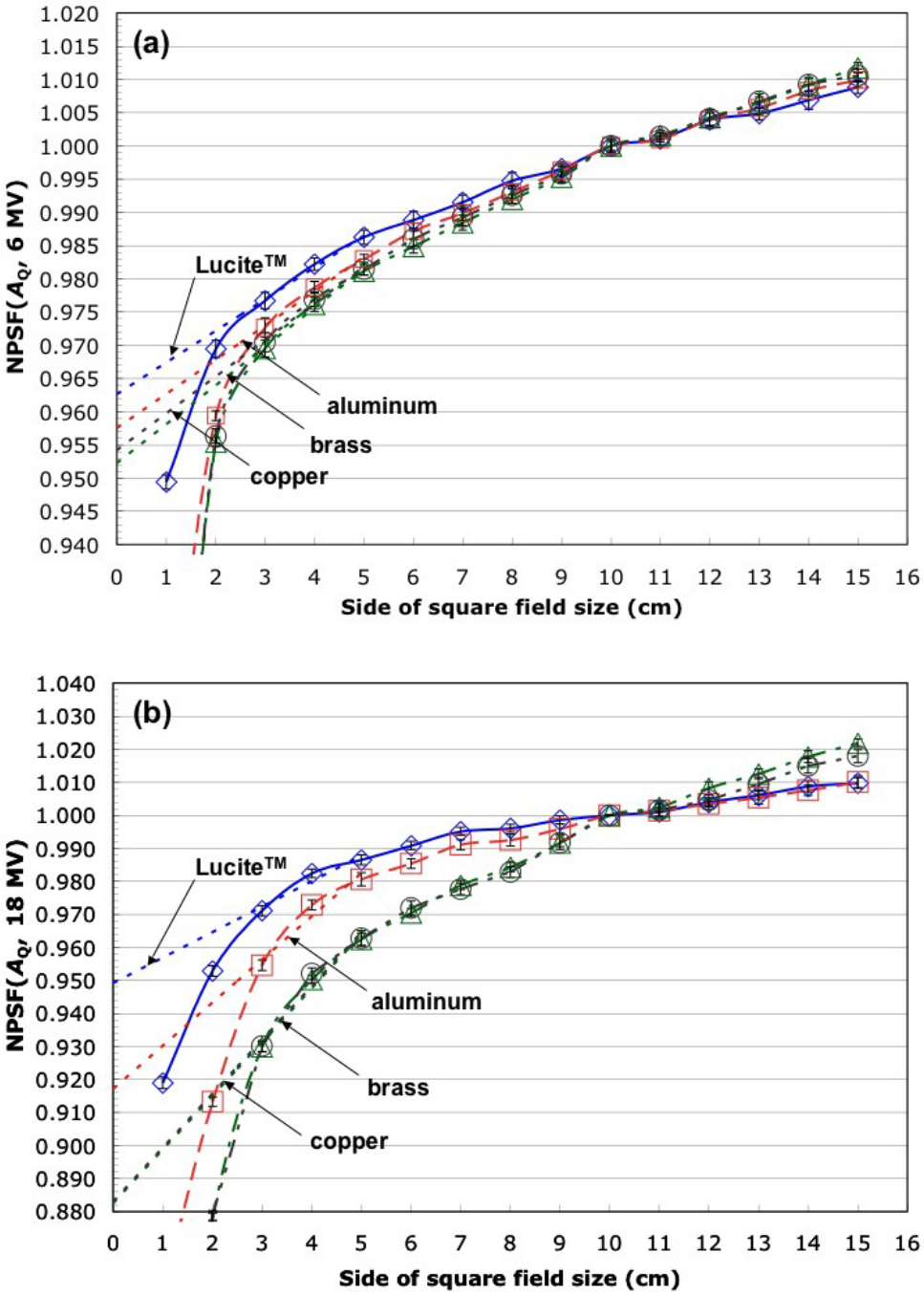

Figure 4–3: Extrapolation of the NPSF, measured with Lucite^{TM}, aluminum, brass, and copper build-up caps, to 0×0 cm^2 field size for the 6 MV photon beam, in part (a), and for the 18 MV photon beam, in part (b).

build-up cap material	Lucite™	aluminum	brass	copper	average
PSF(10, 6 MV)	1.039	1.044	1.050	1.050	1.046 ± 0.005
PSF(10, 18 MV)	1.053	1.090	1.133	1.133	1.102 ± 0.039

Table 4–3: PSFs(10, $h\nu$) for the 6 MV and 18 MV photon beams obtained with Lucite™, aluminum, brass, and copper build-up caps. The data are calculated by extrapolating NPSF to 0×0 cm^2 field size.

6 MV

For the 6 MV photon beam, the extrapolated PSF(10, 6 MV) was smallest (PSF$(10, 6$ MV$) = 1.039$) for the Lucite™ build-up cap and largest (PSF$(10, 6$ MV$) = 1.050$) for the brass and copper build-up caps. The average of the extrapolated PSFs$(10, 6$ MV$)$ obtained with the four build-up cap materials was 1.046 with a standard deviation of 0.005.

18 MV

For the 18 MV photon beam, the extrapolated PSF(10, 18 MV) was also smallest (PSF$(10, 18$ MV$) = 1.053$) when the Lucite™ build-up cap was used, and largest (PSF$(10, 18$ MV$) = 1.133$) when the brass and copper build-up caps were used. The average of the extrapolated PSFs$(10, 18$ MV$)$ with the four build-up cap materials was 1.102 with a standard deviation of 0.039. For the 18 MV photon beam, we observed a non-negligible dependence on the build-up cap material when determining the PSF(10, 18 MV) from the measured NPSF data.

4.3 Monte Carlo-calculated SF for ^{60}Co, 6 MV, and 18 MV photon beams

The scatter factor (SF) for the 10×10 cm^2 field size in a Solid Water™ phantom was calculated for ^{60}Co, 6 MV, and 18 MV photon beams with Monte Carlo methods using the DOSRZnrc/EGSnrcMP user code. The DOSRZnrc user code reports the

total dose D_{tot} and the scatter dose D_{sca} at each scoring region. The SF at a scoring region was calculated using the following relationship:

$$\text{SF}(z, 10, h\nu) = \frac{D_{\text{tot}}}{D_{\text{pri}}} = \frac{D_{\text{tot}}}{D_{\text{tot}} - D_{\text{sca}}}, \tag{4.2}$$

where D_{pri} is the primary dose at the scoring region.

The SF in Solid Water$^{\text{TM}}$ was calculated for depths ranging from 0.5 cm to 30 cm for ^{60}Co beam, for depths ranging from 1.5 cm to 30 cm for the 6 MV photon beam, and for depths ranging from 3.0 cm to 23 cm for the 18 MV photon beam. The input sources for the SF calculations were 10×10 cm^2 phase-space files for the 6 MV and 18 MV photon beams. The phase-space files were obtained using the BEAMnrc user code and were scored at a distance of 90 cm from the x-ray target, as discussed in section 3.3.2. Distances from the radiation source to the phantom surface were 98.5 cm and 97.0 cm for the 6 MV and 18 MV photon beams, respectively. For ^{60}Co simulations, a spectrum file representing the photon particle fluence produced by a Cobalt teletherapy unit was included in the EGSnrc code system package. The spectrum file was used to sample photons emitted by a point source at a distance of 99.5 cm from the phantom surface. In the ^{60}Co simulations, the point source emitted a diverging beam that produced a 10×10 cm^2 field size at z_{max} in the Solid Water$^{\text{TM}}$ phantom.

The calculated total dose, primary dose, and scatter dose versus depth along the beam central axis in the Solid Water$^{\text{TM}}$ phantom for the 10×10 cm^2 field size are shown in Figs. 4–4, 4–5, and 4–6 for ^{60}Co, 6 MV, and 18 MV photon beams, respectively. The SF was calculated from the data in Figs. 4–4, 4–5, and 4–6. The SF

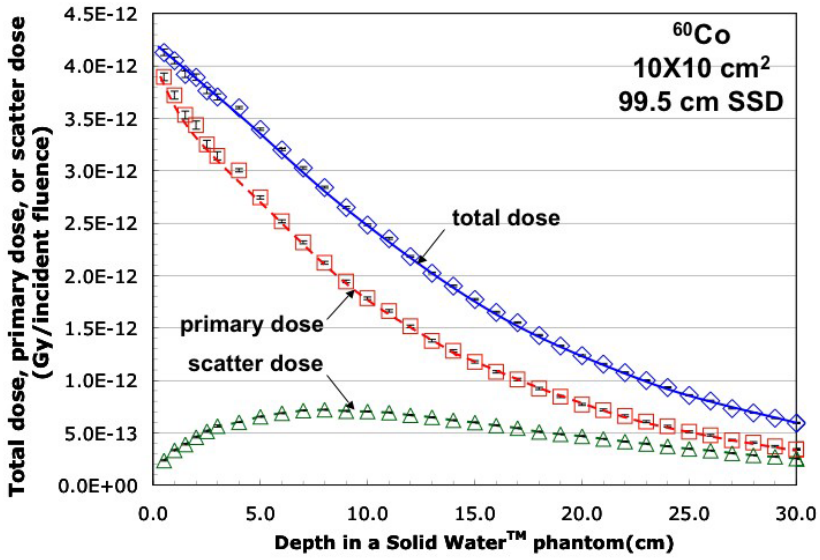

Figure 4–4: Total dose, scatter dose, and primary dose per incident fluence for the 10×10 cm^2 field size versus depth along the beam central axis in a Solid Water^{TM} phantom for the ^{60}Co beam.

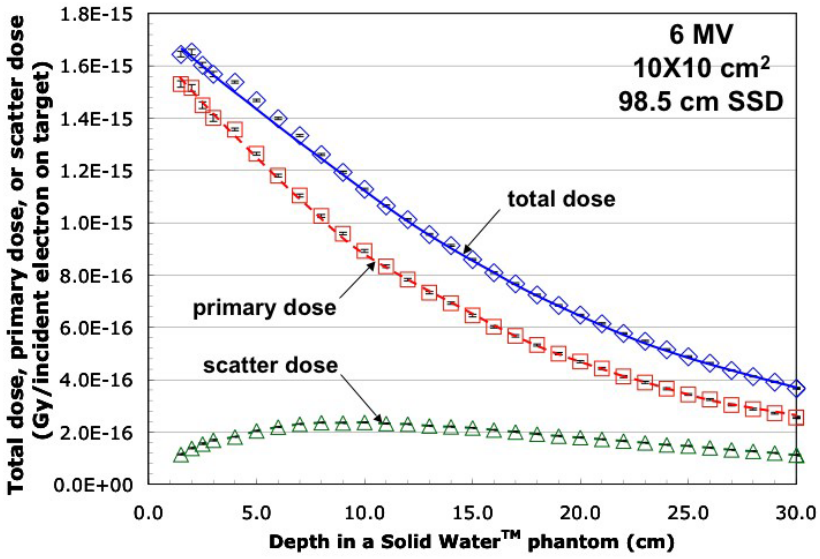

Figure 4–5: Total dose, scatter dose, and primary dose per incident electron on target for the 10×10 cm^2 field size versus depth along the beam central axis in a Solid Water^{TM} phantom for the 6 MV photon beam.

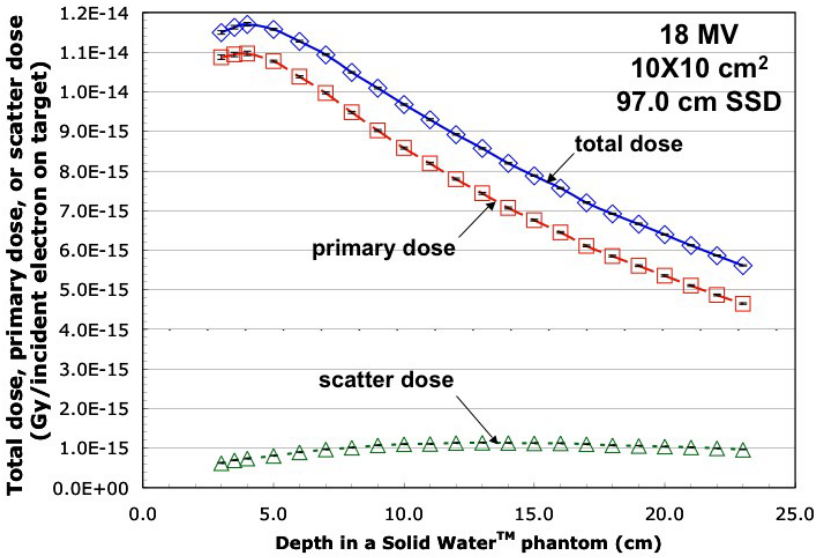

Figure 4–6: Total dose, scatter dose, and primary dose per incident electron on target for the 10×10 cm^2 field size versus depth along the beam central axis in a Solid Water^{TM} phantom for the 18 MV photon beam.

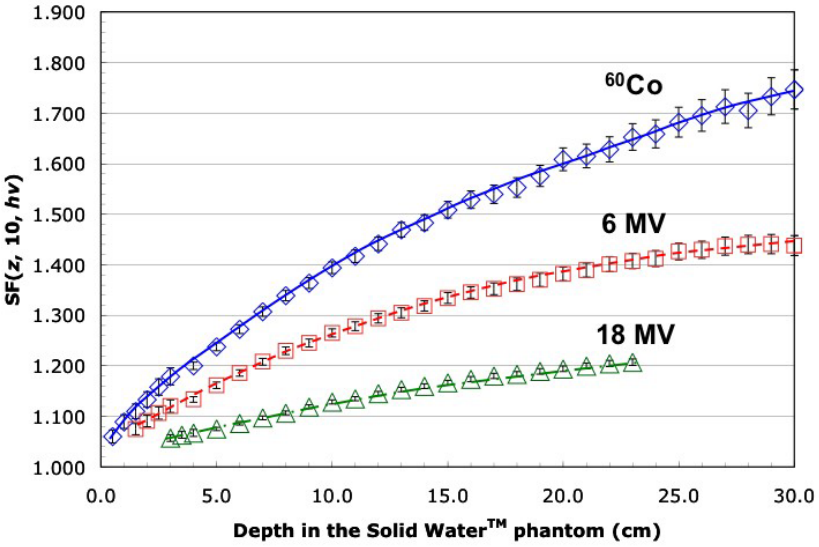

Figure 4–7: The SF versus depth along the beam central axis for the 10×10 cm^2 field size in a Solid Water^{TM} phantom for ^{60}Co, 6 MV, and 18 MV photon beams.

at depth z along the beam central axis for the 10×10 cm^2 field size was defined using Eq. 4.2. Figure 4–7 shows the SF along the beam central axis for the 10×10 cm^2 field size against depth in Solid Water^{TM} for ^{60}Co, 6 MV, and 18 MV photon beams. The SF for ^{60}Co, 6 MV, and 18 MV photon beams increases with increasing depth in the Solid Water^{TM} phantom. At a given depth beyond z_{max}, the SF for the 10×10 cm^2 field size is largest for the ^{60}Co beam and smallest for the 18 MV photon beam. For example, at 20 cm depth, the SF for the ^{60}Co beam is 1.606, whereas the SFs for the 6 MV and 18 MV photon beams are 1.385 and 1.193, respectively.

4.4 Monte Carlo-calculated PSF for ^{60}Co, 6 MV, and 18 MV photon beams

The PSF is the SF at the depth of maximum dose z_{max}[1, 2]. For the 10×10 cm^2 field size, the nominal depths of maximum dose in the Solid Water^{TM} phantom for ^{60}Co, 6 MV, and 18 MV photon beams are 0.5 cm, 1.5 cm, and 3.0 cm, respectively.

^{60}Co beam

The calculated value of the PSF(10, ^{60}Co) from Fig. 4–7 was 1.060 ± 0.013. The calculated PSF(10, ^{60}Co) is 0.6 % greater than the PSF(10, ^{60}Co) listed in the BJR Supplement 25[1] (PSF(10, ^{60}Co)=1.054). Li[3] obtained a PSF(10, ^{60}Co) of 1.060 $\pm$ 0.002 with Monte Carlo methods using a ^{60}Co spectrum that represents a Cobalt teletherapy unit. The ^{60}Co spectrum included the fluence contribution from photons scattered within the source capsule, source housing, and collimators in addition to the two γ photons (1.17 MeV and 1.33 MeV) emitted through the decay of a ^{60}Co radionuclide. Li[3] pointed out that the PSF(10, ^{60}Co) posted in the BJR Supplement 25[1] was obtained with a ^{60}Co radionuclide spectrum rather than a Cobalt unit spectrum, and showed that the presence of the scattered photons in

the spectrum of a Cobalt teletherapy unit slightly increased the PSF(10, ^{60}Co). Our calculated PSF(10, ^{60}Co) is in agreement with the PSF(10, ^{60}Co) calculated by Li[3].

6 MV and 18 MV photon beams

For the 6 MV photon beam, the calculated PSF(10, 6 MV) was 1.075 ± 0.011, which was 2–3 % larger than the PSF(10, 6 MV) obtained using the measured NPSF data. For the 18 MV photon beam, the calculated PSF(10, 18 MV) was 1.057 ± 0.007. The calculated PSF(10, 18 MV) agreed with the PSF(10, 18 MV) obtained from the measured NPSF data with the Lucite^{TM} build-up cap. However, the calculated PSF(10, 18 MV) was 3–7 % lower than the PSF obtained from the measured NPSF data with the aluminum, brass, and copper build-up caps. Hence, for the 6 MV and 18 MV photon beams, the extrapolated PSFs(10, $h\nu$) obtained from the measured NPSF data in general disagreed with the Monte Carlo-calculated PSF(10, $h\nu$). The only exception was the agreement between the extrapolated PSF(10, $h\nu$) obtained with the Lucite^{TM} build-up cap and the Monte Carlo-calculated PSF(10, $h\nu$) for the 18 MV photon beam.

4.5 Air cavity dose versus build-up thickness

We investigated the discrepancy the PSF(10, $h\nu$) between the measurements and Monte Carlo calculations by using Monte Carlo methods to study the air cavity dose in the Exradin A1SL ionization chamber when used for in-phantom measurements and in-air measurements. We used a simple RZ geometry in Monte Carlo simulations to represent the Exradin A1SL ionization chamber. The RZ geometry, shown schematically in Fig. 4–8, includes the wall, central collecting electrode, and guard ring of the Exradin A1SL ionization chamber. The air cavity of the simple

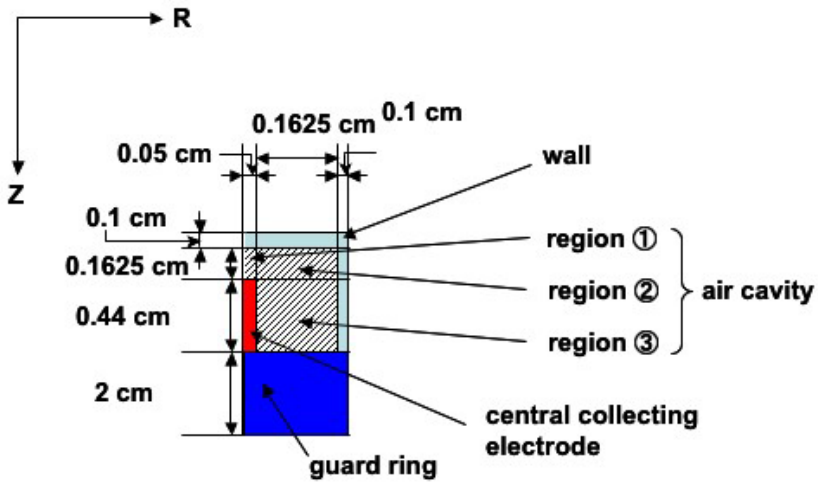

Figure 4–8: RZ geometry to represent the Exradin A1SL ionization chamber.

RZ ionization chamber geometry consists of three scoring regions, as indicated in Fig. 4–8. Since the DOSRZnrc user code reports the mass and the absorbed dose of each scoring region, the air cavity dose D_{air} was determined with the following relationship:

$$D_{\text{air}} = \frac{\sum_{\text{i}=1}^{3} m_{\text{i}} D_{\text{i,air}}}{\sum_{\text{i}=1}^{3} m_{\text{i}}}, \tag{4.3}$$

where m_i and $D_{i,\text{air}}$ are the mass and the air cavity dose in scoring region i, respectively. The standard deviation of the air cavity dose $\sigma_{\text{D}_{\text{air}}}$ was determined by the following equation:

$$\sigma_{\text{D}_{\text{air}}} = \frac{\sqrt{\sum_{\text{i}=1}^{3} (m_{\text{i}} \sigma_{\text{D}_{\text{i,air}}})^2}}{\sum_{\text{i}=1}^{3} m_{\text{i}}}, \tag{4.4}$$

where $\sigma_{D_{i,air}}$ is the standard deviation of the air cavity dose in scoring region i. Since the simple RZ ionization chamber geometry is not an exact representation of the Exradin A1SL ionization chamber, we carried out a test to establish whether the simple RZ geometry adequately represents the Exradin A1SL ionization chamber or not.

We first measured the ionization chamber signal for an SAD setup (SAD=100 cm) as a function of build-up thickness for the 6 MV and 18 MV photon beams. The data were measured for build-up thickness ranging from 0.176 g/cm^2 to 4.0 g/cm^2 using the Lucite^{TM}, aluminum, brass, and copper build-up caps. The total build-up thickness consists of the wall thickness (0.176 g/cm^2) and the build-up cap thickness. The field size at the ionization chamber plane was set to 10×10 cm^2.

The air cavity dose in the ionization chamber as a function of build-up thickness in an SAD setup (SAD=100 cm) for a 10×10 cm^2 field size was also calculated for the 6 MV and 18 MV photon beams with Monte Carlo methods using the DOSRZnrc/EGSnrcMP user code. An RZ geometry used for the Monte Carlo simulations is shown in Fig. 4–9. In this RZ geometry, a build-up cap geometry is added to the simple RZ ionization chamber geometry. The build-up cap geometry has a constant height, but a variable radial thickness.

The air cavity dose was first calculated using a phase-space file, and then calculated for a point source model emitting a photon spectrum. The phase-space file was obtained using the BEAMnrc user code for a 10×10 cm^2 field size and scored at 90 cm from the x-ray target, as discussed in section 3.3.2. The point source model was a photon point source positioned at 100 cm from the ionization chamber plane

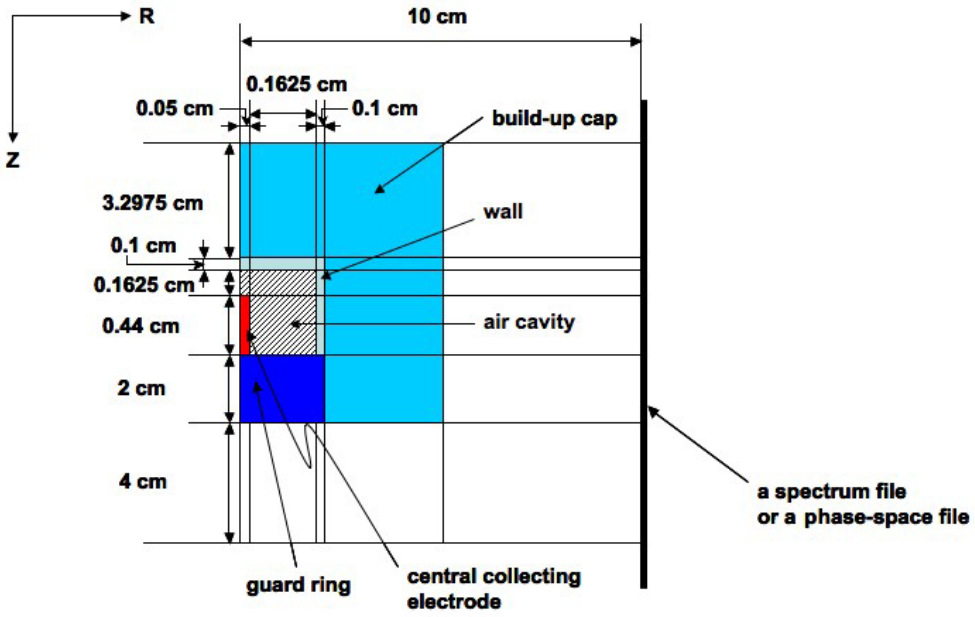

Figure 4–9: RZ geometry to calculate the air cavity dose in the Exradin A1SL ionization chamber with a build-up cap.

that produced a 10×10 cm^2 field size at the ionization chamber plane. The photons emitted from the point source were sampled from a spectrum file extracted from photons presented in the 10×10 cm^2 phase-space file.

6 MV

The normalized measured and Monte Carlo-calculated air cavity doses versus build-up thickness for the 6 MV photon beam are shown in Fig. 4–10 for Lucite^{TM} and aluminum build-up caps and in Fig. 4–11 for brass and copper build-up caps. The air cavity dose was normalized to 1 at 1.5 g/cm^2 build-up thickness. The variation of the air cavity dose for build-up thicknesses greater than 1.0 g/cm^2 obtained from the Monte Carlo calculations is in agreement with the measurements for all four build-up cap materials. For build-up thicknesses less than 1.0 g/cm^2, the normalized air cavity

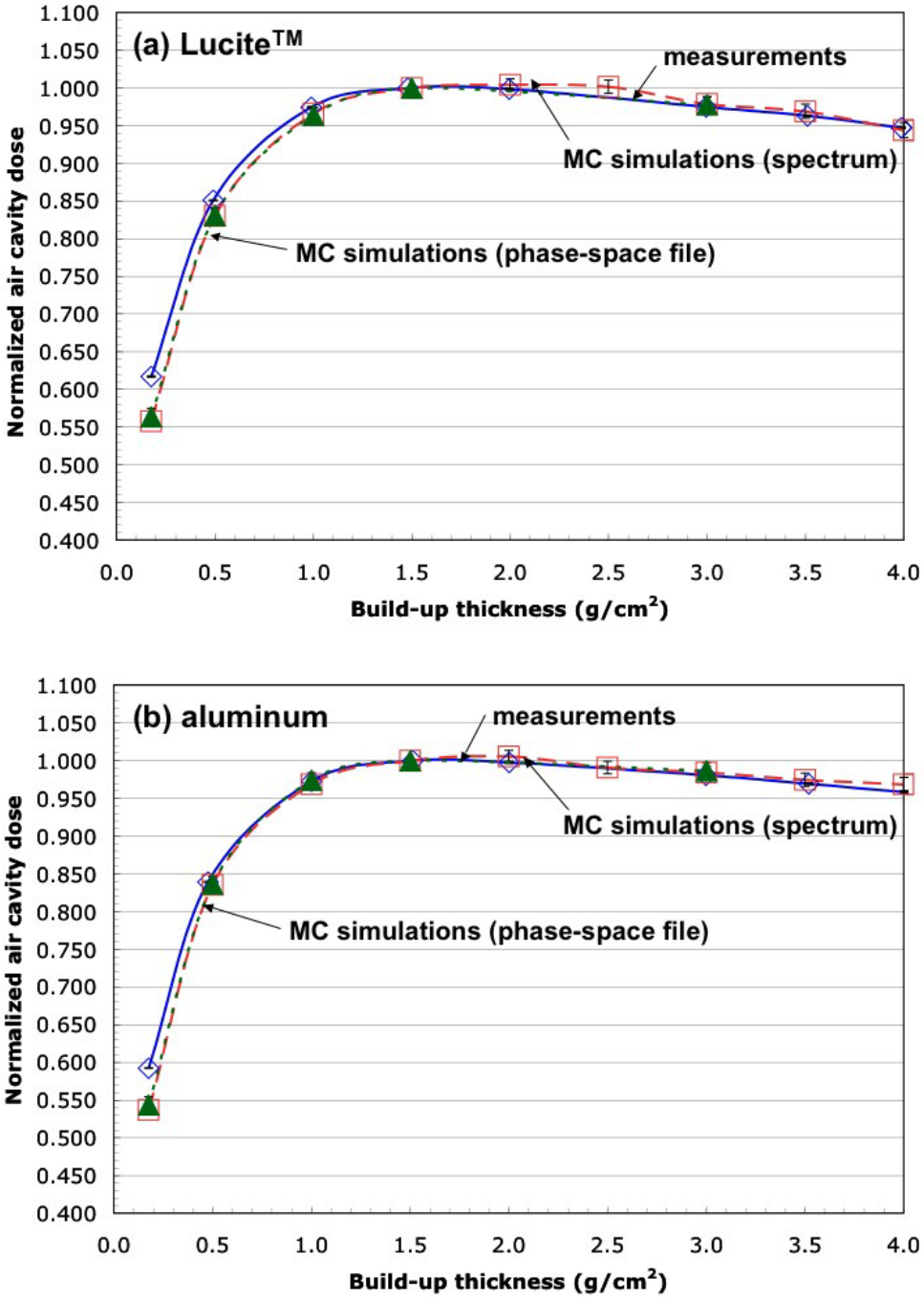

Figure 4–10: Normalized air cavity dose for the 6 MV photon beam, obtained from the measurements and the Monte Carlo simulations, against build-up thickness for Lucite™ build-up caps, in part (a), and aluminum build-up caps, in part (b).

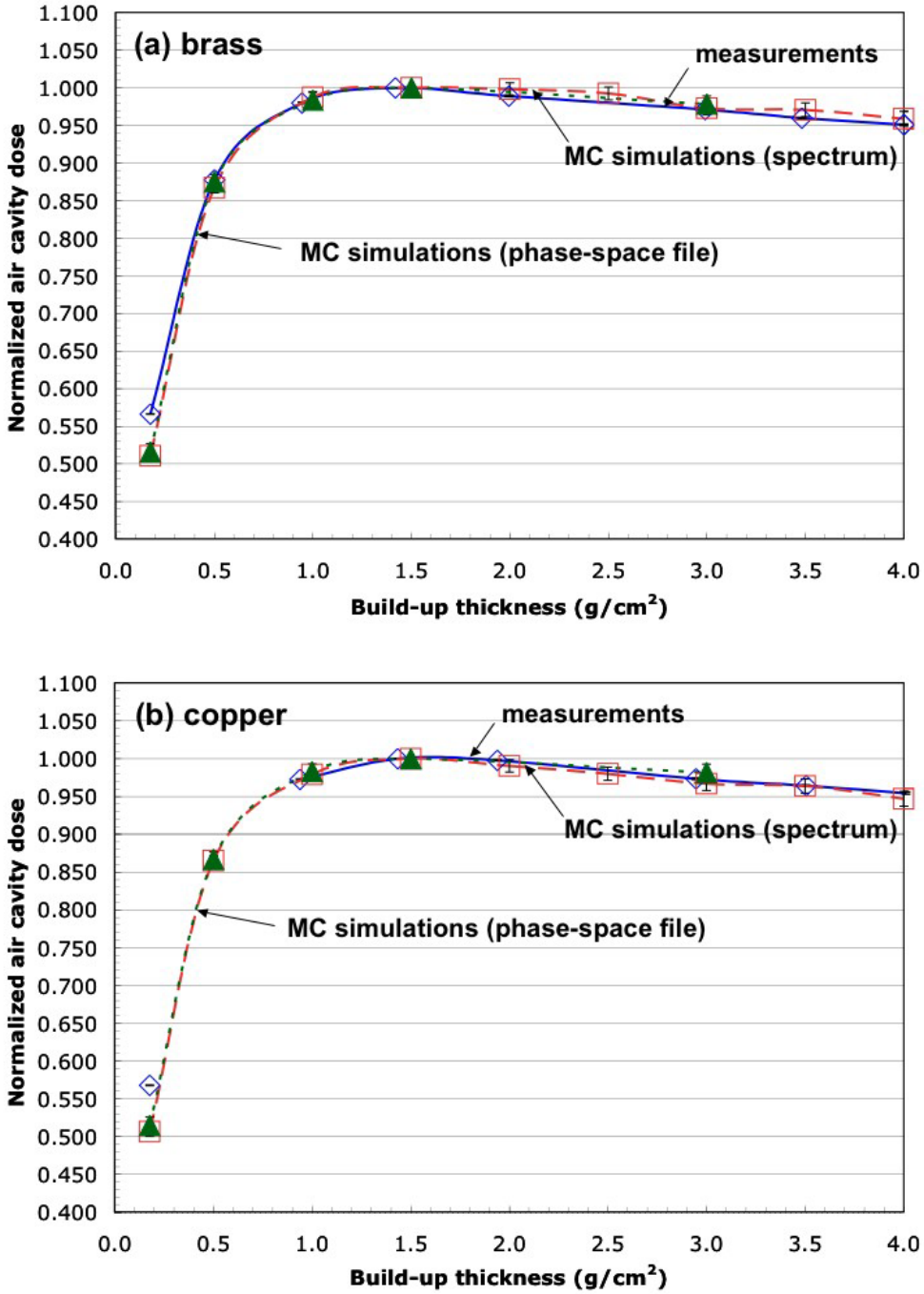

Figure 4–11: Normalized air cavity dose for the 6 MV photon beam, obtained from the measurements and the Monte Carlo simulations, against build-up thickness for brass build-up caps, in part (a), and copper build-up cap, in part (b).

dose obtained from the Monte Carlo calculations is smaller than the measurements, with a maximum difference of 9–11 % at 0.176 g/cm^2 build-up thickness, i.e., 0 cm build-up cap thickness. The variation of the air cavity dose for the 6 MV photon beam obtained from the Monte Carlo simulations with the phase-space file is similar to that obtained with the spectrum file for all build-up thicknesses. We speculate that the Monte Carlo beam model does not correctly account for the contaminating electrons produced from the treatment head for the 6 MV photon beam.

18 MV

The normalized measured and Monte Carlo-calculated air cavity doses versus build-up thickness for the 18 MV photon beam are shown in Fig. 4–12 for Lucite^{TM} and aluminum build-up caps and in Fig. 4–13 for brass and copper build-up caps. The data were normalized to 1 at 3.0 g/cm^2 build-up thickness. For build-up thicknesses greater than 2.0 g/cm^2, the variation of the Monte Carlo-calculated air cavity dose with build-up thickness is in agreement with the measurements for all the build-up cap materials. For build-up thicknesses less than 2.0 g/cm^2, the normalized air cavity dose calculated with the Monte Carlo calculations for the 18 MV photon beam is smaller than the measurements. The difference of the normalized air cavity dose between the measurements and the Monte Carlo calculations for the 18 MV photon beam is maximum at 0.176 g/cm^2 build-up thickness, i.e., 0 cm build-up cap thickness, with a percentage difference of approximately 25 %. The percentage difference between the calculated and measured normalized air cavity doses decreases with increasing build-up thickness. The variation of the air cavity dose with build-up thickness determined by the Monte Carlo calculations with the phase-space file is

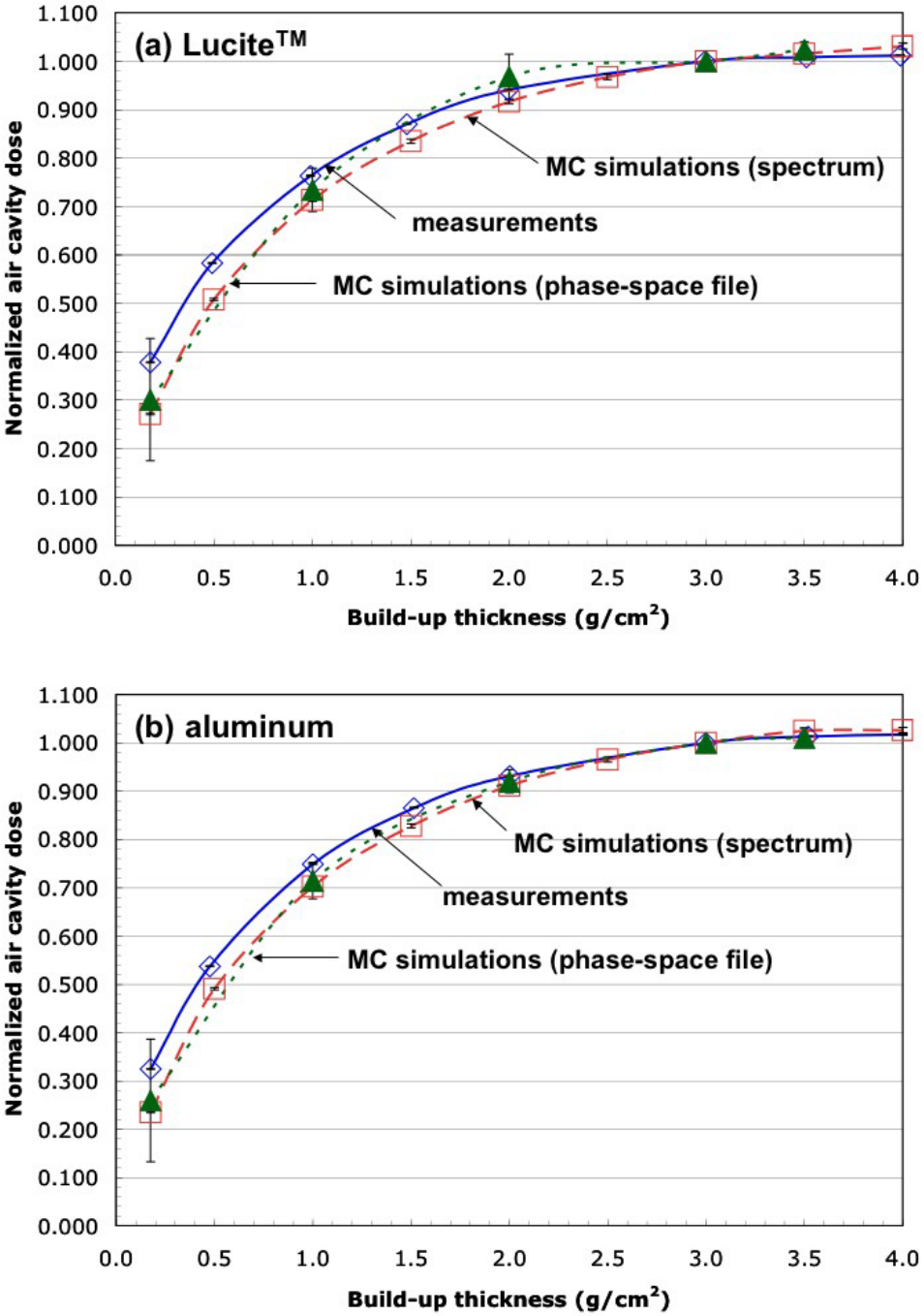

Figure 4–12: Normalized air cavity dose for the 18 MV photon beam, obtained from the measurements and the Monte Carlo simulations, against build-up thickness for Lucite™ build-up caps, in part (a), and aluminum build-up caps, in part (b).

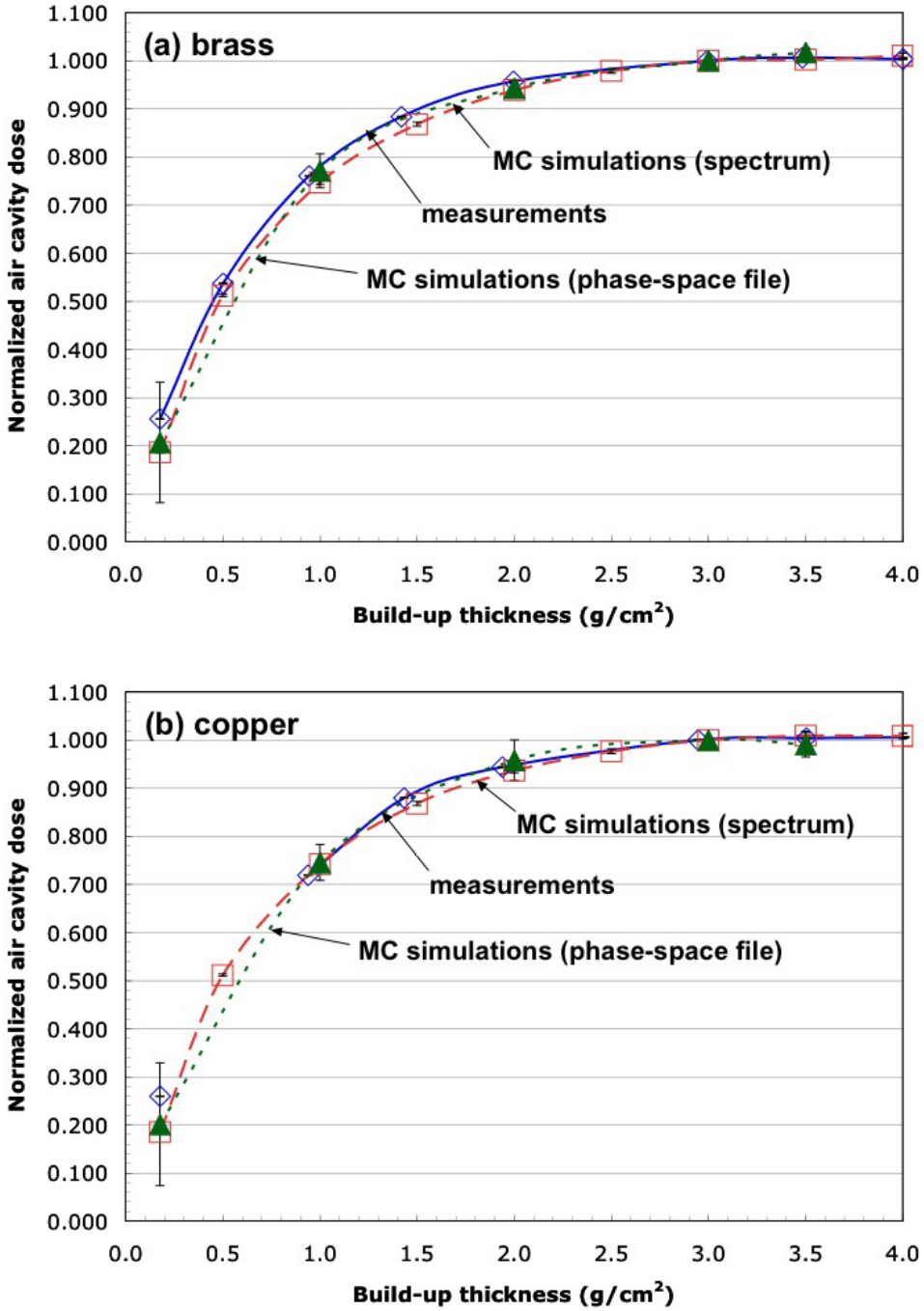

Figure 4–13: Normalized air cavity dose for the 18 MV photon beam, obtained from the measurements and the Monte Carlo simulations, against build-up thickness for brass build-up caps, in part (a), and copper build-up caps, in part (b).

similar to the that determined with the spectrum file. We attribute the difference between the measurements and the Monte Carlo calculations to inaccurate modeling of the contaminating electrons produced from the treatment head in the Monte Carlo calculations for the 18 MV photon beam.

The Monte Carlo calculations using the simple RZ ionization chamber geometry underestimated the variation of the air cavity dose in the ionization chamber when the build-up thickness was less than 1.0 g/cm^2 for the 6 MV photon beam and 2.0 g/cm^2 for the 18 MV photon beam. However, for build-up thicknesses greater than 1.0 g/cm^2 and 2.0 g/cm^2 for the 6 MV and 18 MV photon beams, respectively, the Monte Carlo calculations of the air cavity dose in the ionization chamber agreed with the measurements. Therefore, we conclude that our RZ geometry of the Exradin A1SL ionization chamber can be used to study the response of the Exradin A1SL ionization chamber with the build-up cap when the build-up cap thickness is sufficiently large.

4.6 Separation of primary and scatter doses in the air cavity of the ionization chamber in the in-air measurements and in the in-phantom measurements

4.6.1 Primary and scatter doses in the air cavity in the in-air measurements

Monte Carlo methods were used to estimate the primary and scatter doses deposited in the air cavity of the ionization chamber for the 10×10 cm^2 field size as a function of build-up thickness for the 6 MV and 18 MV photon beams. The total and scatter doses in the air cavity were calculated using the DOSRZnrc/EGSnrcMP user code with the RZ geometry shown in Fig. 4–9. For the 6 MV photon beam, the

build-up thickness including the thickness of the ionization chamber's wall ranged from 0.176 g/cm^2 to 4.0 g/cm^2. For the 18 MV photon beam, the total and scatter doses deposited in the air cavity were calculated for build-up thicknesses up to 4.0 g/cm^2 for Lucite^{TM} build-up caps, up to 11.8 g/cm^2 for aluminum build-up caps, and up to 18.5 g/cm^2 for brass and copper build-up caps. The 10×10 cm^2 phase-space files for the 6 MV and 18 MV photon beams were used as input sources, which were obtained using the BEAMnrc user code and scored at 90 cm from the x-ray target, as discussed in section 3.3.2.

The DOSRZnrc user code reports the mass, total dose, and scatter dose in each scoring region. The air cavity of the Exradin A1SL ionization chamber is represented by three scoring regions, as shown in Fig. 4–8. The primary dose in the air cavity D_{pri} and the standard deviation of the primary dose $\sigma_{D_{\mathrm{pri}}}$ were calculated, respectively, with the following relationships:

$$D_{\mathrm{pri}} = \frac{\sum_{\mathrm{i}=1}^{3} m_{\mathrm{i}}(D_{\mathrm{i,tot}} - D_{\mathrm{i,sca}})}{\sum_{\mathrm{i}=1}^{3} m_{\mathrm{i}}}, \tag{4.5}$$

$$\sigma_{D_{\mathrm{pri}}} = \frac{\sqrt{\sum_{\mathrm{i}=1}^{3} \{m_{\mathrm{i}}^2(\sigma_{D_{\mathrm{i,tot}}}^2 - \sigma_{D_{\mathrm{i,sca}}}^2)\}}}{\sum_{\mathrm{i}=1}^{3} m_{\mathrm{i}}}, \tag{4.6}$$

where m_{i} is the mass of air cavity scoring region i, $D_{\mathrm{i,tot}}$ and $D_{\mathrm{i,sca}}$ are the total and scatter doses in air cavity scoring region i, respectively, and $\sigma_{D_{\mathrm{i,tot}}}$ and $\sigma_{D_{\mathrm{i,sca}}}$ are the standard deviations of the total and scatter doses in air cavity scoring region i, respectively. The standard deviation of the total dose in air cavity scoring region

i was considered as the sum of the standard deviations of the primary and scatter doses in air cavity scoring region i, i.e., $\sigma_{\mathrm{D_{i,tot}}} = \sigma_{\mathrm{D_{i,pri}}} + \sigma_{\mathrm{D_{i,sca}}}$. We assumed that there is no correlation between the primary dose and the scatter dose in the air cavity. The scatter dose in the air cavity D_{sca} and the standard deviation of the scatter dose $\sigma_{\mathrm{D_{sca}}}$ were calculated, respectively, with the following equations:

$$D_{\mathrm{sca}} = \frac{\sum_{\mathrm{i}=1}^{3} m_{\mathrm{i}} D_{\mathrm{i,sca}}}{\sum_{\mathrm{i}=1}^{3} m_{\mathrm{i}}}, \tag{4.7}$$

$$\sigma_{\mathrm{D_{sca}}} = \frac{\sqrt{\sum_{\mathrm{i}=1}^{3} (m_{\mathrm{i}} \sigma_{\mathrm{D_{i,sca}}})^2}}{\sum_{\mathrm{i}=1}^{3} m_{\mathrm{i}}}. \tag{4.8}$$

6 MV

Figure 4–14 shows the normalized calculated primary and scatter doses deposited in the air cavity of the ionization chamber for the 10×10 cm^2 field size against build-up thickness for the 6 MV photon beam. The primary and scatter doses are normalized to 1 at 0.176 g/cm^2 build-up thickness, i.e., the thickness of the ionization chamber's wall. For a given build-up cap material, the primary dose in the air cavity first increases with increasing build-up thickness, shows a maximum at 1.5 g/cm^2 build-up thickness, and then decreases with further increase in build-up thickness. At a given build-up thickness, the primary dose in the air cavity also increases with increasing build-up cap material density. For example, at 1.5 g/cm^2

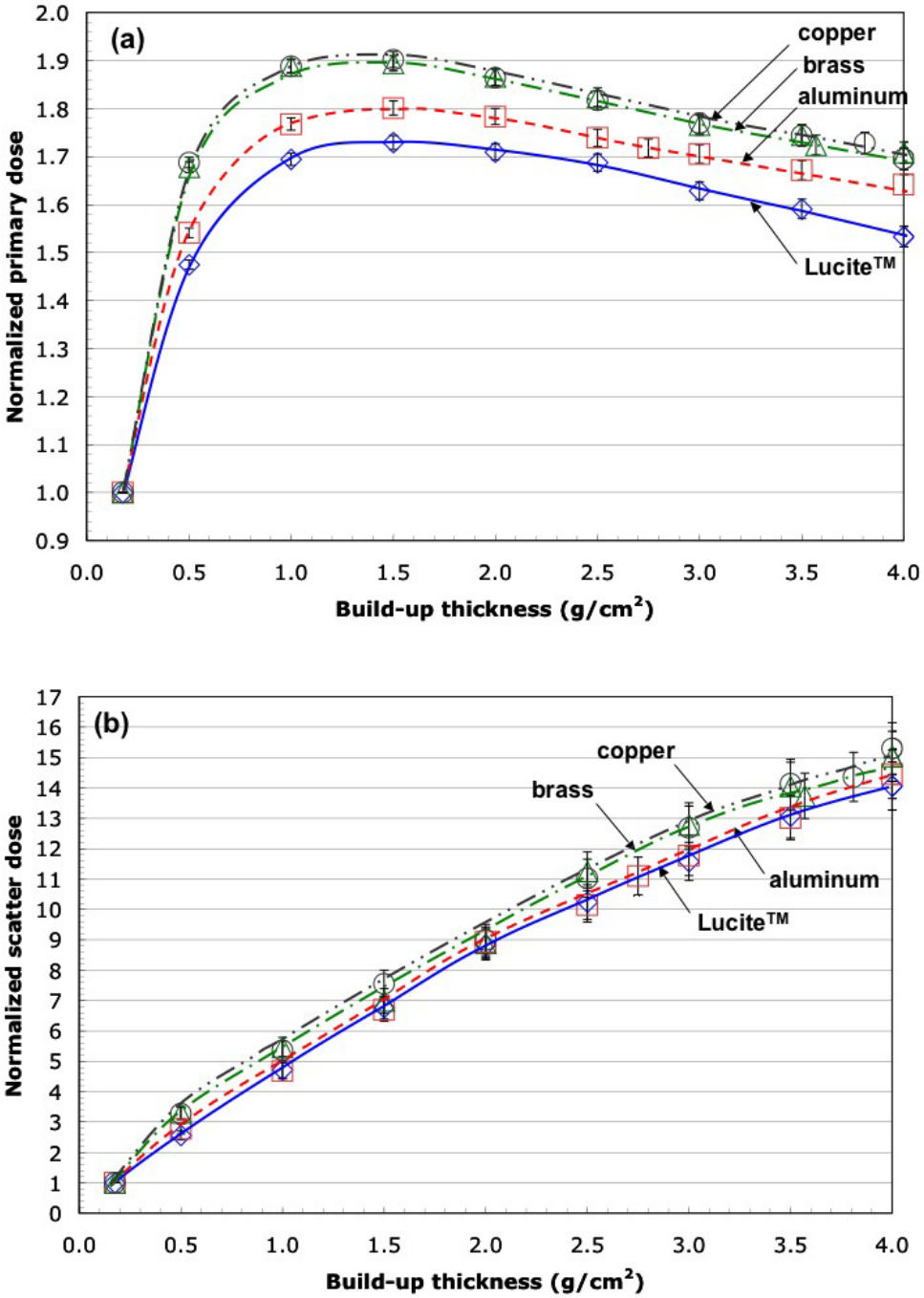

Figure 4–14: Normalized primary dose, in part (a), and scatter dose, in part (b), deposited in the air cavity for the 6 MV photon beam versus build-up thickness calculated for Lucite^{TM}, aluminum, brass, and copper build-up caps.

build-up thickness, the primary dose with the copper build-up cap is 9 % greater than that with the Lucite^{TM} build-up cap.

For a given build-up cap material, the scatter dose in the air cavity for the 6 MV photon beam steadily increases with increasing build-up thickness. The increase in the scatter dose with build-up thickness is essentially due to the increase in the build-up cap volume from which photons are scattered. With respect to build-up cap material density, the scatter dose in the air cavity also increases with increasing build-up cap material density. For example, at 1.5 g/cm^2 build-up thickness, the scatter dose produced from the copper build-up cap is 18 % greater than that with the Lucite^{TM} build-up cap.

Figure 4–14 shows that the primary and scatter doses in the air cavity for the 6 MV photon beam increase with increasing build-up cap material density; essentially increasing the total dose in the air cavity. At 1.5 g/cm^2 build-up thickness, the total dose in the air cavity with the copper build-up cap is 10 % greater than the air cavity dose with the Lucite^{TM} build-up cap. This result is congruent with our measurements. The apparent PSF(10, 6 MV) measured with the Lucite^{TM} build-up cap, 1.032, is 9 % larger than that with the copper build-up cap, 0.951, as shown in Fig. 4–1.

18 MV

The normalized calculated primary and scatter doses in the air cavity of the ionization chamber for the 10×10 cm^2 field size versus build-up thickness for the 18 MV photon beam are shown in Fig. 4–15. The primary and scatter doses are normalized to 1 at 0.176 g/cm^2 build-up thickness. For all build-up cap materials, the primary

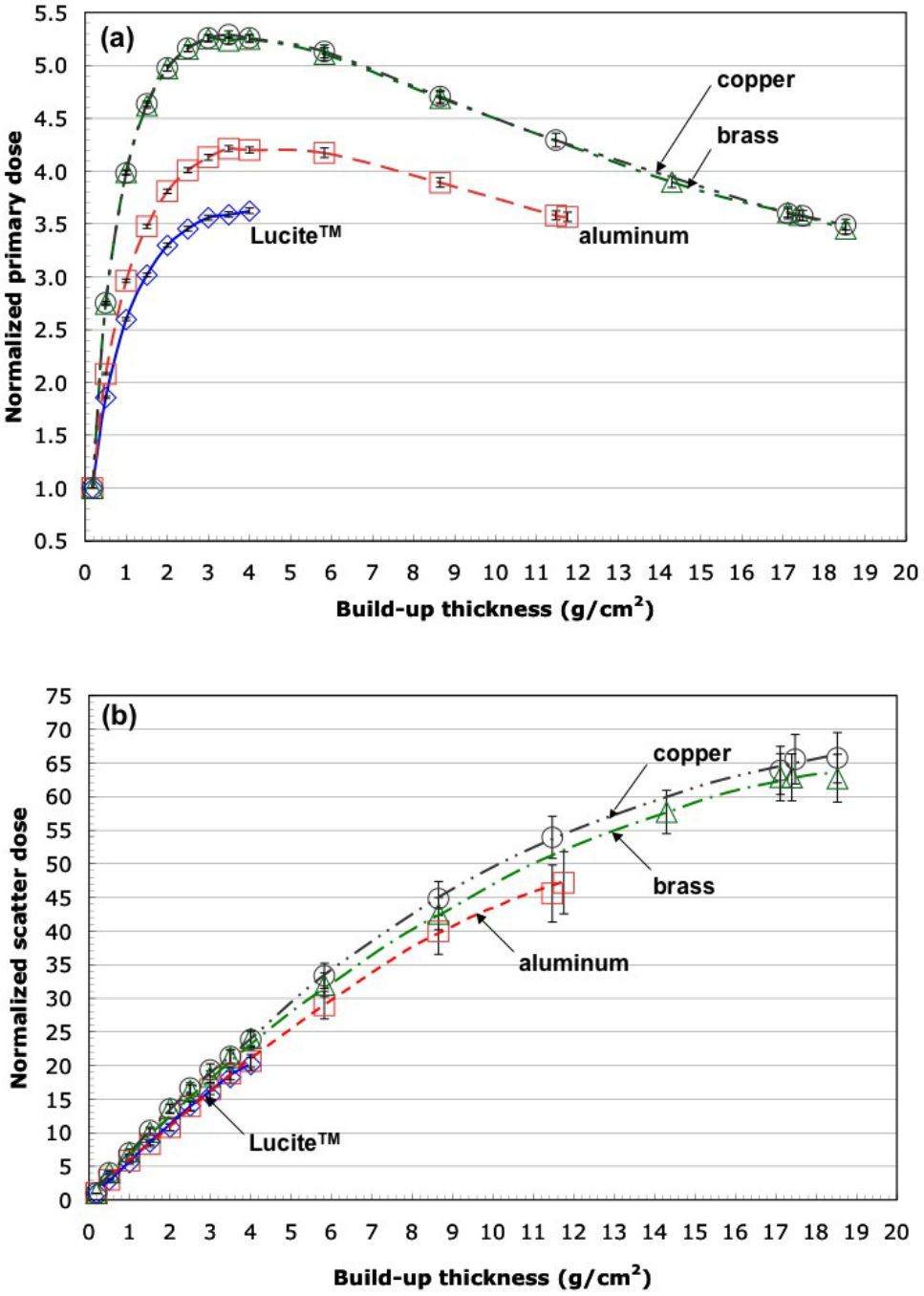

Figure 4–15: Normalized primary dose, in part (a), and scatter dose, in part (b), deposited in the air cavity for the 18 MV photon beam versus build-up thickness calculated for Lucite™, aluminum, brass, and copper build-up caps.

dose first increases with increasing build-up thickness, reaches a maximum at about 3.5 g/cm^2, and then decreases with further increase in build-up thickness. Similarly to the 6 MV photon beam, the primary dose in the air cavity at a given build-up thickness for the 18 MV photon beam is smallest with the Lucite^{TM} build-up cap and largest with the copper build-up cap. The difference in the primary dose between the different build-up cap materials for the 18 MV photon beam is larger than that in the 6 MV photon beam. For example, at 3.0 g/cm^2 build-up thickness, the primary dose with the copper build-up cap is 50 % larger than that with the Lucite^{TM} build-up cap.

The scatter dose in the air cavity for the 18 MV photon beam increases steadily with increasing build-up thickness for all build-up cap materials. Similarly to the primary dose, the scatter dose in the air cavity increases with increasing build-up cap material density. At 3.0 g/cm^2 build-up thickness, the scatter dose with the copper build-up cap is 18 % larger than that with the Lucite^{TM} build-up cap for the same build-up thickness.

Figure 4–15 shows that the primary and scatter doses in the air cavity for the 18 MV photon beam also increase with increasing build-up cap material density, thereby increasing the total dose in the air cavity. At 3.0 g/cm^2 build-up thickness, the total dose in the air cavity with the copper build-up cap is 49 % greater than that with the Lucite^{TM} build-up cap. This result is in agreement with our measurements. As shown in Fig. 4–1, the apparent PSF$(10, 18\ \text{MV})$ measured with the Lucite^{TM} build-up cap, 1.030, is 45 % greater than that with the copper build-up cap, 0.709.

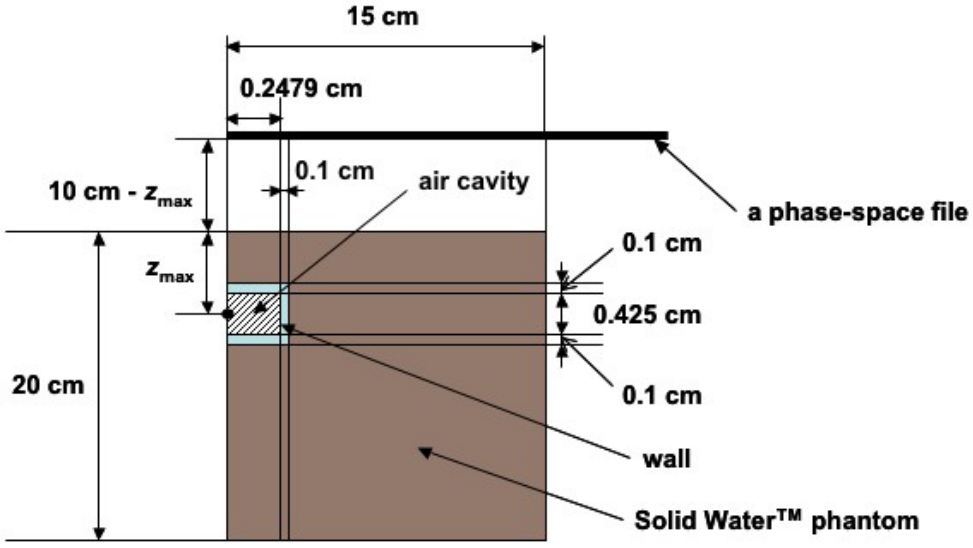

Figure 4–16: RZ Geometry to calculate the primary dose in the air cavity at the nominal $z_{\max}$ in the Solid Water$^{\text{TM}}$ phantom.

4.6.2 Primary dose in the air cavity in the in-phantom measurements

For the 10×10 cm^2 field size, the primary dose in the air cavity at 1.5 cm depth for the 6 MV photon beam and 3.0 cm depth for the 18 MV photon beam in the Solid Water$^{\text{TM}}$ phantom were calculated with Monte Carlo methods using the DOSRZnrc/EGSnrcMP user code. The RZ geometry used for the Monte Carlo simulations is shown in Fig. 4–16. The total and scatter doses in the air cavity were calculated using the 10×10 cm^2 phase-space file, and the primary dose in the air cavity was determined by subtracting the scatter dose from the total dose in the air cavity.

6 MV

Table 4–4 lists the calculated primary dose in the air cavity for the 10×10 cm^2 field size at 1.5 cm depth in the Solid Water$^{\text{TM}}$ phantom and the calculated primary

Material (1)	Primary dose component (Gy/incident particle) (2)	Primary dose relative to Solid Water^{TM} (3)
Solid Water^{TM} phantom	1.015E-16 ($\pm$1.193 %)	-
Lucite^{TM}	1.009E-16 ($\pm$0.670 %)	0.994 $\pm$ 0.014
Aluminum	1.047E-16 ($\pm$0.642 %)	1.032 $\pm$ 0.014
Brass	1.101E-16 ($\pm$0.697 %)	1.085 $\pm$ 0.015
Copper	1.101E-16 ($\pm$0.674 %)	1.085 $\pm$ 0.015

Table 4–4: Primary dose in the air cavity at 1.5 cm depth in the Solid Water^{TM} phantom and primary doses in the air cavity with 1.5 g/cm^2 Lucite^{TM}, aluminum, brass, and copper build-up caps for the 10 $\times$ 10 cm^2 field size in the 6 MV photon beam. Column 3 lists the ratio of the primary dose in the air cavity with the build-up cap to that in the Solid Water^{TM} phantom.

dose in the air cavity for 1.5 g/cm^2 build-up thickness with the Lucite^{TM}, aluminum, brass, and copper build-up caps for the 6 MV photon beam. When the build-up thickness is equal to 1.5 g/cm^2, Table 4–4 shows that the primary dose in the air cavity with the Lucite^{TM} build-up cap is statistically in agreement with the primary dose in the air cavity at 1.5 cm depth in the Solid Water^{TM} phantom. For aluminum, brass, and copper build-up caps, the primary doses in the air cavity are 3 %, 9 %, and 9 % greater than that in the Solid Water^{TM} phantom, respectively.

18 MV

The calculated primary dose in the air cavity in the Solid Water^{TM} phantom for the 10 $\times$ 10 cm^2 field size and the calculated primary dose in the air cavity for 3.0 g/cm^2 build-up thickness with the Lucite^{TM}, aluminum, brass, and copper build-up caps are summarized in Table 4–5. For build-up thickness of 3.0 g/cm^2, the primary dose in the air cavity with the Lucite^{TM} build-up cap is approximately equal to the primary dose in the air cavity at 3.0 cm depth in the Solid Water^{TM}

Material (1)	Primary dose component (Gy/incident particle) (2)	Primary dose relative to Solid Water^{TM} (3)
Solid Water^{TM} phantom	7.586E-16 ($\pm$0.617 %)	-
Lucite^{TM}	7.510E-16 ($\pm$0.458 %)	0.990 $\pm$ 0.008
Aluminum	8.736E-16 ($\pm$0.414 %)	1.152 $\pm$ 0.009
Brass	1.114E-15 ($\pm$0.403 %)	1.469 $\pm$ 0.011
Copper	1.126E-15 ($\pm$0.396 %)	1.484 $\pm$ 0.011

Table 4–5: Primary dose in the air cavity at 3.0 cm depth in the Solid Water^{TM} phantom and primary dose in the air cavity with 3.0 g/cm^2 Lucite^{TM}, aluminum, brass, and copper build-up caps for the 10×10 cm^2 field size in the 18 MV photon beam. Column 3 lists the ratio of the primary dose in the air cavity with the build-up cap to that in the Solid Water^{TM} phantom.

phantom. For the same build-up thickness, the primary doses in the air cavity with aluminum, brass, and copper build-up caps are 15 %, 47 %, and 48 % greater than that in the Solid Water^{TM} phantom, respectively.

In our in-air measurements, the measured ionization signal is essentially related to the total dose deposited in the air cavity of the ionization chamber. To separate the primary dose component from the measured signal, we calculated the ratio of the primary dose to the total dose in the air cavity for 1.5 g/cm^2 build-up thickness in the 6 MV photon beam and for 3.0 g/cm^2 build-up thickness in the 18 MV photon beam for the Lucite^{TM}, aluminum, brass, and copper build-up caps.

Table 4–6 summarizes the calculated ratio of the primary dose to the total dose in the air cavity with the Lucite^{TM}, aluminum, brass, and copper build-up caps for the 6 MV and 18 MV photon beams. For the 6 MV photon beam, about 5 % of the total dose in the air cavity is deposited by scattered photons produced within the build-up cap. For the 18 MV photon beam, the contribution of the scattered photons

build-up cap material (1)	6 MV (2)	18 MV (3)
Lucite^{TM}	0.952 ± 0.009	0.956 ± 0.007
aluminum	0.954 ± 0.009	0.960 ± 0.006
brass	0.955 ± 0.009	0.964 ± 0.006
copper	0.951 ± 0.009	0.963 ± 0.006

Table 4–6: Ratios of the primary dose to the total dose in the air cavity with Lucite^{TM}, aluminum, brass, and copper build-up caps for the 6 MV and 18 MV photon beams. Build-up thicknesses are 1.5 g/cm^2 for the 6 MV photon beam and 3.0 g/cm^2 for the 18 MV photon beam.

produced within the build-up cap to the total dose in the air cavity is about 4 %. The scatter dose fraction is independent of the build-up cap material for the 6 MV and 18 MV photon beams.

4.7 PSF(10, $h\nu$) corrected from the apparent PSF(10, $h\nu$) for 6 MV and 18 MV photon beams

4.7.1 Correction for scatter dose contribution

Using the calculated ratios of the primary dose to the total dose in the air cavity with the Lucite^{TM}, aluminum, brass, and copper build-up caps, we corrected the measured apparent PSF(10, $h\nu$) for the 6 MV and 18 MV photon beams with a factor that removes the contribution of photons scattered within the build-up cap from the measured signal. The PSF(10, $h\nu$) was determined by the following relationship:

$$\text{PSF}(10, h\nu) = \text{apparent PSF}(10, h\nu) \times \frac{1}{C_{\text{p}}}, \tag{4.9}$$

where C_{p} is the ratio of the primary dose to the total dose in the air cavity with the build-up cap. The correction factor C_{p} is related to the parameter B introduced by

build-up cap material (1)	apparent PSF(10, 6 MV) (2)	PSF(10, 6 MV) (3)
Lucite^{TM}	1.032 ± 0.001	1.084 ± 0.010
aluminum	0.993 ± 0.001	1.041 ± 0.009
brass	0.947 ± 0.001	0.992 ± 0.009
copper	0.951 ± 0.001	1.000 ± 0.009
Monte Carlo-calculated PSF(10, 6 MV)		**1.075 ± 0.011**

Table 4–7: Apparent PSFs(10, 6 MV) (column 2) and PSFs(10, 6 MV) (column 3) obtained with Lucite^{TM}, aluminum, brass, and copper build-up caps.

the BJR Supplement 17[2] (section 2.5) through the following relationship:

$$C_{\mathrm{p}} = \frac{1}{1+B}. \tag{4.10}$$

6 MV

Table 4–7 lists the apparent PSFs(10, 6 MV) and the PSFs(10, 6 MV) corrected with Eq. 4.9 obtained with the Lucite^{TM}, aluminum, brass, and copper build-up caps. The Monte Carlo-calculated PSF(10, 6 MV), i.e., the ratio of the total dose to the primary dose at 1.5 cm depth in the Solid Water^{TM} phantom, is also included in Table 4–7. The PSF(10, 6 MV) measured with the Lucite^{TM} build-up cap and corrected with the factor C_{p} is in agreement with the Monte Carlo-calculated PSF(10, 6 MV). The PSFs(10, 6 MV) obtained with the aluminum, brass, and copper build-up caps, however, are smaller than the Monte Carlo-calculated PSF(10, 6 MV).

18 MV

Table 4–8 lists the apparent PSFs(10, 18 MV) and the PSFs(10, 18 MV) corrected with Eq. 4.9 obtained with the Lucite^{TM}, aluminum, brass, and copper build-up caps as well as the Monte Carlo-calculated PSF(10, 18 MV), which is defined

build-up cap material (1)	apparent PSF(10, 18 MV) (2)	PSF(10, 18 MV) (3)
Lucite^{TM}	1.030 ± 0.001	1.078 ± 0.007
aluminum	0.888 ± 0.001	0.926 ± 0.006
brass	0.695 ± 0.001	0.721 ± 0.004
copper	0.709 ± 0.001	0.737 ± 0.004
Monte Carlo-calculated PSF(10, 18 MV)		**1.057 ± 0.007**

Table 4–8: Apparent PSFs(10, 18 MV) (column 2) and PSFs(10, 18 MV) (column 3) obtained with Lucite^{TM}, aluminum, brass, and copper build-up caps.

as the total dose to the primary dose at 3.0 cm depth in the Solid Water^{TM} phantom. The discrepancy between the PSF(10, 18 MV) corrected with the factor $C_{\rm p}$ and the Monte Carlo-calculated PSF(10, 18 MV) is smallest with the Lucite^{TM} build-up cap (+2 %). Similarly to the 6 MV photon beam, the PSFs(10, 18 MV) obtained with the aluminum, brass, and copper build-up caps and corrected with Eq. 4.9 are smaller than the Monte Carlo-calculated PSF(10, 18 MV).

The correction of the apparent PSF(10, $h\nu$) for the 6 MV and 18 MV photon beams with the correction factor $C_{\rm p}$ improved our measured data with the Lucite^{TM} build-up cap. Although the correction factor $C_{\rm p}$ increased the measured PSFs(10, $h\nu$) with the aluminum, brass, and copper build-up caps, the PSFs(10, $h\nu$) obtained with Eq. 4.9 were smaller than the Monte Carlo-calculated PSF(10, $h\nu$) for the 6 MV and 18 MV photon beams.

4.7.2 Correction for primary dose contribution

The correction factor $C_{\rm p}$ or the parameter B accounts for the contribution of the scattered photons produced within the build-up cap to the measured signal in the ionization chamber. We have shown in Figs. 4–14 and 4–15 that the primary

dose in the air cavity was dependent on the build-up cap material density for the 6 MV and 18 MV photon beams. In an attempt to account for the dependence of the primary dose in the air cavity on the build-up cap material density, we calculated a correction factor based on first principals of cavity theory. Assuming that the air cavity ionization is produced by electrons released from the surrounding media, i.e., the thickness of the ionization chamber's wall is zero, the correction factor was derived as shown below.

The total dose deposited in the Solid Water^{TM} phantom D_{sw} is related to the total dose in the air cavity $D_{air,\,pha}$ with the following relationship:

$$D_{sw} = D_{air,\,pha} \times \left(\frac{\overline{L}_{\Delta}}{\rho}\right)^{SW}_{air}, \tag{4.11}$$

where $\left(\frac{\overline{L}_{\Delta}}{\rho}\right)^{SW}_{air}$ is the mean restricted collision stopping power ratio of Solid Water^{TM} to air. The primary dose in Solid Water^{TM} D^{pri}_{sw} obtained with the build-up cap is related to the primary dose in the air cavity $D^{pri}_{air,\,cap}$ by the following equation:

$$D^{pri}_{sw} = D^{pri}_{air,\,cap} \times \left(\frac{\overline{L}_{\Delta}}{\rho}\right)^{cap}_{air} \times \left(\frac{\overline{\mu}_{ab}}{\rho}\right)^{SW}_{cap}, \tag{4.12}$$

where $\left(\frac{\overline{L}_{\Delta}}{\rho}\right)^{cap}_{air}$ is the mean restricted collision stopping power ratio of a build-up cap material to air and $\left(\frac{\overline{\mu}_{ab}}{\rho}\right)^{SW}_{cap}$ is the mean mass energy absorption coefficient ratio of Solid Water^{TM} to the build-up cap material. Equation 4.12 assumes that the ionization in the air cavity of the ionization chamber is essentially generated by electrons produced within the build-up cap. The PSF(10, $h\nu$) is given by the

following relationship:

$$\mathrm{PSF}(10, h\nu) = \frac{D_{\mathrm{SW}}(z_{\max}, 10, h\nu)}{D^{\mathrm{pri}}_{\mathrm{SW}}(z_{\max}, 10, h\nu)} = \frac{D_{\mathrm{air,\ pha}}}{D^{\mathrm{pri}}_{\mathrm{air,\ cap}}} \times \left(\frac{\overline{L}_{\Delta}}{\rho}\right)^{\mathrm{SW}}_{\mathrm{cap}} \times \left(\frac{\overline{\mu}_{\mathrm{ab}}}{\rho}\right)^{\mathrm{cap}}_{\mathrm{SW}}. \tag{4.13}$$

The primary dose in the air cavity with the build-up cap $D^{\mathrm{pri}}_{\mathrm{air,\ cap}}$ is related to the total dose in the air cavity with the build-up cap $D_{\mathrm{air,\ cap}}$ as follows:

$$D^{\mathrm{pri}}_{\mathrm{air,\ cap}} = D_{\mathrm{air,\ cap}} \times C_{\mathrm{p}}. \tag{4.14}$$

where C_{p} is the ratio of the primary dose to the total dose in the air cavity with the build-up cap. Since the apparent PSF is defined as the ratio of total dose in the air cavity in the Solid Water$^{\mathrm{TM}}$ phantom $D_{\mathrm{air,\ pha}}$ to the total dose in the air cavity with the build-up cap $D_{\mathrm{air,\ cap}}$, the PSF(10, $h\nu$) is related to the apparent PSF(10, $h\nu$) by the following relationship:

$$\mathrm{PSF}(10, h\nu) = \text{apparent PSF}(10, h\nu) \times \frac{1}{C_{\mathrm{p}}} \times \left(\frac{\overline{L}_{\Delta}}{\rho}\right)^{\mathrm{SW}}_{\mathrm{cap}} \times \left(\frac{\overline{\mu}_{\mathrm{ab}}}{\rho}\right)^{\mathrm{cap}}_{\mathrm{SW}}. \tag{4.15}$$

The mean restricted stopping power ratios of Solid Water$^{\mathrm{TM}}$ to the build-up cap materials $\left(\frac{\overline{L}_{\Delta}}{\rho}\right)^{\mathrm{SW}}_{\mathrm{cap}}$ were calculated with Monte Carlo methods using the SPRRZnrc/EGSnrcMP user code. The input sources of the Monte Carlo simulations were the $10 \times 10\ \mathrm{cm}^2$ phase-space files for the 6 MV and 18 MV photon beams. The mean mass energy absorption coefficient ratios of the build-up cap materials to Solid Water$^{\mathrm{TM}}$ $\left(\frac{\overline{\mu}_{\mathrm{ab}}}{\rho}\right)^{\mathrm{cap}}_{\mathrm{SW}}$ were calculated with Monte Carlo methods using the g/EGSnrcMP user code for the 6 MV and 18 MV photon spectrum files.

build-up cap material (1)	apparent PSF(10, 6 MV) (2)	C_{p} (3)	$\left(\frac{\overline{L}_{\Delta}}{\rho}\right)^{\mathrm{SW}}_{\mathrm{cap}}$ (4)	$\left(\frac{\overline{\mu}_{\mathrm{ab}}}{\rho}\right)^{\mathrm{cap}}_{\mathrm{SW}}$ (5)	PSF(10, 6 MV) (6)
Lucite$^{\mathrm{TM}}$	1.032 ± 0.001	0.952 ± 0.009	1.000 ± 0.001	1.000 ± 0.001	1.084 ± 0.010
aluminum	0.993 ± 0.001	0.954 ± 0.009	1.279 ± 0.001	0.913 ± 0.001	1.215 ± 0.011
brass	0.947 ± 0.001	0.955 ± 0.009	1.553 ± 0.002	0.929 ± 0.002	1.432 ± 0.013
copper	0.951 ± 0.001	0.951 ± 0.009	1.537 ± 0.001	0.925 ± 0.001	1.422 ± 0.013
Monte Carlo-calculated PSF(10, 6 MV)					$\mathbf{1.075 \pm 0.011}$

Table 4–9: PSF(10, 6 MV) in Solid Water$^{\mathrm{TM}}$ (column 6) obtained using Lucite$^{\mathrm{TM}}$, aluminum, brass, and copper build-up caps for in-air measurements and corrected with Eq. 4.15. Column 2 lists the measured apparent PSFs(10, 6 MV) with the Lucite$^{\mathrm{TM}}$, aluminum, brass, and copper build-up caps. Columns 3, 4, and 5 list ratios of the primary dose to the total dose deposited in the air cavity with the build-up caps, ratios of the mean restricted collision stopping powers of Solid Water$^{\mathrm{TM}}$ to build-up cap materials, and ratios of the mean mass energy absorption coefficients of build-up cap materials to Solid Water$^{\mathrm{TM}}$ for the 6 MV photon beam, respectively.

6 MV

Table 4–9 lists the PSFs(10, 6 MV) in Solid Water$^{\mathrm{TM}}$ obtained by correcting the measured apparent PSFs(10, 6 MV) using Eq. 4.15 for the Lucite$^{\mathrm{TM}}$, aluminum, brass, and copper build-up caps (column 6). Table 4–9 also summarizes the ratios of the primary dose to the total dose in the air cavity with the build-up caps C_{p} (column 3), the ratios of the mean restricted collision stopping powers of Solid Water$^{\mathrm{TM}}$ to the build-up cap materials $\left(\frac{\overline{L}_{\Delta}}{\rho}\right)^{\mathrm{SW}}_{\mathrm{cap}}$ (column 4), and the ratios of the mean mass energy absorption coefficients of the build-up cap materials to Solid Water$^{\mathrm{TM}}$ $\left(\frac{\overline{\mu}_{\mathrm{ab}}}{\rho}\right)^{\mathrm{cap}}_{\mathrm{SW}}$ (column 5) for the 6 MV photon beam. The Monte Carlo-calculated PSF(10, 6 MV) is also included in Table 4–9. The corrected PSF(10, 6 MV) obtained with the Lucite$^{\mathrm{TM}}$ build-up cap is statistically in agreement with the Monte Carlo-calculated PSF(10, 6 MV). Correction of the apparent PSFs(10, 6 MV) with Eq. 4.15 substantially increases the measured PSFs(10, 6 MV) with the aluminum,

build-up cap material (1)	apparent PSF(10, 18 MV) (2)	C_{p} (3)	$\left(\frac{\overline{L}_{\Delta}}{\rho}\right)_{\mathrm{cap}}^{\mathrm{SW}}$ (4)	$\left(\frac{\overline{\mu}_{\mathrm{ab}}}{\rho}\right)_{\mathrm{SW}}^{\mathrm{cap}}$ (5)	PSF(10, 18 MV) (6)
Lucite$^{\mathrm{TM}}$	1.030 ± 0.001	0.956 ± 0.007	0.996 ± 0.001	0.998 ± 0.001	1.071 ± 0.007
aluminum	0.888 ± 0.001	0.960 ± 0.006	1.256 ± 0.001	1.012 ± 0.002	1.177 ± 0.008
brass	0.695 ± 0.001	0.964 ± 0.006	1.507 ± 0.002	1.203 ± 0.001	1.307 ± 0.008
copper	0.709 ± 0.001	0.963 ± 0.006	1.505 ± 0.001	1.194 ± 0.001	1.323 ± 0.008
Monte Carlo-calculated PSF(10, 18 MV)					$\mathbf{1.057 \pm 0.007}$

Table 4–10: PSF(10, 18 MV) in Solid Water$^{\mathrm{TM}}$ (column 6) obtained using Lucite$^{\mathrm{TM}}$, aluminum, brass, and copper build-up caps for in-air measurements and corrected using Eq. 4.15. Column 2 lists the measured apparent PSFs(10, 18 MV) with the Lucite$^{\mathrm{TM}}$, aluminum, brass, and copper build-up caps. Columns 3, 4, 5 list ratios of the primary dose to the total dose deposited in the air cavity with the build-up cap, ratios of the mean restricted collision stopping powers of Solid Water$^{\mathrm{TM}}$ to build-up cap materials, and ratios of the mean mass energy absorption coefficients of build-up cap materials to Solid Water$^{\mathrm{TM}}$ for the 18 MV photon beam, respectively.

brass, and copper build-up caps. However, the PSFs(10, 6 MV) are now larger than the Monte Carlo-calculated PSF(10, 6 MV).

18 MV

Table 4–10 lists the PSFs(10, 18 MV) in Solid Water$^{\mathrm{TM}}$ obtained by correcting the measured apparent PSFs(10, 18 MV) using Eq. 4.15 as well as the Monte Carlo-calculated PSF(10, 18 MV) (column 6). The ratios of the primary dose to the total dose in the air cavity with the build-up caps C_{p} (column 3), the ratios of the mean restricted collision stopping powers of Solid Water$^{\mathrm{TM}}$ to the build-up cap materials $\left(\frac{\overline{L}_{\Delta}}{\rho}\right)_{\mathrm{cap}}^{\mathrm{SW}}$ (column 4), and the ratios of the mean mass energy absorption coefficients of the build-up cap materials to Solid Water$^{\mathrm{TM}}$ $\left(\frac{\overline{\mu}_{\mathrm{ab}}}{\rho}\right)_{\mathrm{SW}}^{\mathrm{cap}}$ (column 5) for the 18 MV photon beam are also listed in Table 4–10. For the Lucite$^{\mathrm{TM}}$ build-up cap, the discrepancy between the PSF(10, 18 MV) obtained with Eq. 4.15 and the Monte

Carlo-calculated PSF(10, 18 MV) is smaller than that obtained with Eq. 4.9. Thus, correcting the primary dose in the air cavity improves the measured result. The PSF obtained with the Lucite^{TM} build-up cap and corrected with build-up cap scattering only is 1.078 ± 0.007, while correcting for the primary dose in the air cavity gives a PSF(10, 18 MV) of 1.071 ± 0.007, which is statistically closer to the Monte Carlo-calculated PSF(10, 18 MV) (1.057 ± 0.007). The PSFs(10, 18 MV) for the aluminum, brass, and copper build-up caps corrected with Eq. 4.15 are greater than those corrected for build-up cap scattering only. However, the corrected PSFs(10, 18 MV) are larger than the Monte Carlo-calculated PSF(10, 18 MV).

From the data in Tables 4–9 and 4–10, we conclude that the PSFs(10, $h\nu$) measured with the Lucite^{TM} build-up cap and corrected with Eq. 4.15 are in agreement with the Monte Carlo-calculated PSFs(10, $h\nu$) for the 6 MV and 18 MV photon beams. For the Lucite^{TM} build-up cap, the main cause of the discrepancy between the measured apparent PSF(10, $h\nu$) and the Monte Carlo-calculated PSF(10, $h\nu$) is the scatter dose contribution produced within the build-up cap. As shown in Tables 4–4 and 4–5, the difference of the primary dose in the air cavity between with the Solid Water^{TM} phantom and with the Lucite^{TM} build-up cap for the 6 MV and 18 MV photon beams is less than 1 % and can be ignored.

For the aluminum, brass, and copper build-up caps, the scattered photons within the build-up cap also contributed to the dose in the air cavity. However, the primary dose in the air cavity for the 6 MV and 18 MV photon beams was larger when the ionization chamber was surrounded by higher density material build-up cap than the primary dose in the air cavity at $z_{\max}$ in the Solid Water^{TM} phantom, as shown in

Tables 4–4 and 4–5. Correction of the apparent PSFs$(10, h\nu)$ obtained with the aluminum, brass, and copper build-up caps for build-up cap scattering only resulted in PSFs(10, $h\nu$) smaller than the Monte Carlo-calculated PSF(10, $h\nu$) for both megavoltage photon beams.

When we included our simple correction factor derived in Eq. 4.15, the measured PSFs(10, $h\nu$) were larger than the Monte Carlo-calculated PSF(10, $h\nu$). We acknowledged that our derived correction factor assumes that the dose in the air cavity is deposited by electrons produced in the surrounding media, i.e., Solid Water$^{\text{TM}}$ or build-up cap. Electrons produced within the ionization chamber's wall were ignored. In reality, part of the air cavity dose is deposited by electrons produced in the ionization chamber's wall or in the air cavity of the ionization chamber. Obtaining a correction factor for the primary dose in the in-air measurements requires a detailed study of the origin of the electron fluence that deposits the dose in the air cavity of the ionization chamber. This essentially suggests that the correction factor for the primary dose component measured with build-up caps having densities much different than water is a function of the ionization chamber's make and model in addition to the beam energy and the build-up cap material. Such correction factors can only be obtained with detailed Monte Carlo studies using accurate ionization chamber geometries and verified experimentally.

REFERENCES

[1] British Journal of Radiology. *Central axis depth dose data for use in radiotherapy: 1996,* Supplement 25. The British Institute of Radiology, London, UK, 1996.

[2] British Journal of Radiology. *Central axis depth dose data for use in radiotherapy,* Supplement 17. The British Institute of Radiology, London, UK, 1983.

[3] X. A. Li. Peak scatter factors for high energy photon beams. *Medical Physics*, 26:962–966, 1999.

CHAPTER 5
Conclusions

5.1 Thesis summary

The goal of this thesis was to measure the peak scatter factors (PSFs) for a 10×10 cm^2 field size in 6 MV and 18 MV photon beams using a Solid Water^{TM} phantom and build-up caps made of Lucite^{TM}, aluminum, brass, and copper. The measurements were carried out using an Exradin A1SL thimble ionization chamber having an air cavity volume of 0.056 cm^3. We also used Monte Carlo methods to calculate the PSF in Solid Water^{TM} and to obtain correction factors for the measurements. The Monte Carlo simulations were performed using the EGSnrc code system[1].

First, the PSF for the 10×10 cm^2 field size was determined experimentally using a technique suggested by the British Journal of Radiology Supplements 17[2] and 25[3]. The BJR Supplement technique for determining the PSF for the 10×10 cm^2 field size involves calculating the normalized PSF (NPSF) from the measured apparent PSF. The NPSF is then extrapolated to 0×0 cm^2 field size and the PSF for the 10×10 cm^2 field size is equal to the reciprocal of the extrapolated value. For the 6 MV photon beam, the average of the extrapolated PSFs for the 10×10 cm^2 field size obtained with the Lucite^{TM}, aluminum, brass, and copper build-up caps was 1.046 ± 0.005. The extrapolated PSF(10, 6 MV) was independent of the build-up cap material. For the 18 MV photon beam, on the other hand, the average of the

extrapolated PSFs for the 10×10 cm^2 field size obtained with the four build-up caps was 1.102 ± 0.039. However, we noted that the different build-up cap materials produced different extrapolated PSF(10, 18 MV). The smallest PSF(10, 18 MV), 1.053, was obtained with the Lucite^{TM} build-up cap and the largest PSF(10, 18 MV), 1.133, was obtained with the brass and copper build-up caps.

For the 6 MV and 18 MV photon beams, the PSF for the 10×10 cm^2 field size was also determined using Monte Carlo methods. The Monte Carlo-calculated PSF(10, $h\nu$) was 1.075 ± 0.011 for the 6 MV photon beam and 1.057 ± 0.007 for the 18 MV photon beam. Although the PSF(10, 6 MV) obtained with the BJR Supplement technique did not depend on the build-up cap material, the numerical value was smaller than the Monte Carlo-calculated PSF$(10, 6$ MV). For the 18 MV photon beam, the extrapolated PSF(10, 18 MV) obtained with the Lucite^{TM} build-up cap was in agreement with the Monte Carlo-calculated PSF$(10, 18$ MV). However, the extrapolated PSFs(10, 18 MV) obtained with the higher density material build-up caps were significantly greater than the Monte Carlo-calculated PSF$(10, 18$ MV).

We investigated the perturbation of the build-up cap material on the PSF measurements. We used Monte Carlo methods to separate the primary and scatter doses deposited in the air cavity of the ionization chamber in the in-air measurements and in the in-phantom measurements. For the 10×10 cm^2 field size, the magnitude of the primary dose for a given build-up thickness increased with increasing build-up cap material density. For build-up thickness of 1.5 g/cm^2 in the 6 MV photon beam, the primary dose with the copper build-up cap was 9 % greater than that with the

Lucite^{TM} build-up cap. For the 18 MV photon beam at 3.0 g/cm^2 build-up thickness, the primary dose with the copper build-up cap was 1.5 times greater than the primary dose with the Lucite^{TM} build-up cap. The results of the Monte Carlo calculations also showed that the contribution of the scatter dose produced within the build-up cap to the total dose in the air cavity is approximately independent of the build-up cap material. For the 10×10 cm^2 field size, the scatter dose contribution to the total dose in the air cavity was 5 % for the 6 MV photon beam and 4 % for the 18 MV photon beam for a build-up thickness of $z_{\max}$.

We tried to calculate a factor to obtain the primary dose for a Solid Water^{TM} build-up cap from measurements with higher density material build-up caps. The correction factor assumed that the primary dose in the air cavity is deposited by electrons generated in the surrounding media. Although the correction factor decreased the primary dose for higher density material build-up caps, the resulting PSFs for the 10×10 cm^2 field size were greater than the Monte Carlo-calculated PSF for the 6 MV and 18 MV photon beams. We propose that an accurate correction factor can only be obtained by considering the contribution of electrons produced within the ionization chamber's wall and its air cavity to the primary dose deposited in the air cavity.

We suggest that PSF measurements should be carried out with build-up caps made of materials having densities close to water, such as Lucite^{TM}. When using higher density material build-up caps, the contribution of the scatter dose to the total dose in the air cavity is comparable to that when using a water-equivalent

material build-up cap. However, the higher density material build-up caps significantly increase the primary dose in the air cavity, hence, may underestimate the PSF value. In addition, factors required to correct the primary dose in the air cavity can not be obtained with simple means. Calculation of such correction factors would involve a rigorous study of the ionization chamber and build-up cap designs.

5.2 Future work

The EGSnrc code system[1] contains a geometry package called the EGSnrc C++ class library[4]. This geometry package allows modeling complex geometries for Monte Carlo simulations. This geometry package may be used to accurately model our Exradin A1SL ionization chamber in order to calculate a factor that corrects the primary dose deposited in the air cavity for the measurements with the aluminum, brass, and copper build-up caps. The Monte Carlo simulations may also be used to calculate the fraction of electrons generated within the ionization chamber's wall that contributes to the dose in the air cavity of the ionization chamber.

A second possible extension of this work is PSF measurements for small field sizes. In our work, we investigated the PSF only for the 10×10 cm^2 field size. For such large field sizes, lateral electronic equilibrium is established on the beam central axis. However, the lateral electronic equilibrium is lost in small field sizes. We suggest that a similar investigation should be carried out for small field sizes where the lateral electronic equilibrium may be lost. The study of small field sizes may lead to better methods of extrapolating the NPSF to 0×0 cm^2 field size accurately to obtain the PSF(10, $h\nu$) from the measurements.

REFERENCES

[1] I. Kawrakow and D. W. O. Rogers. *The EGSnrc code system: Monte Carlo simulation of electron and photon transport,* NRCC Report PIRS-701. National Research Council Canada, Ottawa, ON, 2006.

[2] British Journal of Radiology. *Central axis depth dose data for use in radiotherapy,* Supplement 17. The British Institute of Radiology, London, UK, 1983.

[3] British Journal of Radiology. *Central axis depth dose data for use in radiotherapy: 1996,* Supplement 25. The British Institute of Radiology, London, UK, 1996.

[4] I. Kawrakow. *egspp: the EGSnrc C++ class library,* NRCC Report PIRS-899. National Research Council Canada, Ottawa, ON, 2005.